Iron Oxide Nanoparticles: Preparation, Properties and Applications

THESIS

SUBMITTED TO

BABASAHEB BHIMRAO AMBEDKAR UNIVERSITY
(A CENTRAL UNIVERSITY)
LUCKNOW

BABASAHEB
BHIMRAO
AMBEDKAR
UNIVERSITY

LUCKNOW

प्रज्ञा शील करुणा

ESTABLISHED 1996

FOR THE DEGREE OF

Doctor of Philosophy

IN

APPLIED CHEMISTRY

Submitted by

Sandhya Singh

ENROLMENT NUMBER. 858/12

Under the Supervision of

Prof. Gajanan Pandey

DEPARTMENT OF APPLIED CHEMISTRY
SCHOOL FOR PHYSICAL SCIENCES
BABASAHEB BHIMRAO AMBEDKAR UNIVERSITY
VIDYA VIHAR, RAE BARELI ROAD, LUCKNOW-226 025

2018

Dedicated to

Beloved Parents

For Endless Support, Love and Cooperation

CERTIFICATE

This is to certified that the thesis entitled "**Iron Oxide Nanoparticles: Preparation, Properties and Applications**" submitted by Ms. **Sandhya Singh** is an original research work and has not been previously submitted in part or full for the award of any other degree or diploma to this or other university.

This thesis submitted to Babasaheb Bhimrao Ambedker University Lucknow satisfies all the requirements as stipulated in Doctor of Philosophy (Ph.D) regulation-1999 as emended in 2008/2010/2013 and it is fit for submission and evaluation for the award the degree of Doctor of Philosophy in University.

Supervisor 2/2/18

Head of Department
07/02/18

DECLARATION

I declare that the thesis entitled **"Iron Oxide Nanoparticles: Preparation, Properties and Applications"** has been synthesized by me under the supervision of Prof. Gajanan Pandey, Professor, Department of Applied Chemistry, School for Physical Sciences, Babasaheb Bhimrao Ambedkar University, Lucknow. No part of this thesis has formed the basis for the award of any degree, diploma or fellowship previously. Further, I declare that the material embodied in the present work is based on original research work and the indebtedness to others has been duly acknowledged at relevant places.

Sandhya Singh

(Sandhya Singh)
Department of Applied Chemistry,
School for Physical Sciences,
Babasaheb Bhimrao Ambedkar University,
Vidya Vihar, Raebareli Road,
Lucknow-226025, U.P., India.

Date: 21/02/18

Acknowledgement

Foremost, I wish to express my profound sense of deepest gratitude and sincere thanks to my honourable and esteemed supervisor ***Prof. Gajanan Pandey (Ex-Head of Department)*** *for the continuous support of my Ph.D study and related research, for his patience, motivation, and immense knowledge. His guidance helped me in all the time of research and writing of this thesis. I could not have imagined having a better advisor and mentor for my Ph.D study.*

I convey my sincere thanks to all the faculty members of Chemistry department: ***Prof Kaman Singh (Head & Dean), Assistant Prof. Dr. Jyoti Pandey, Assistant Prof. Dr. Shailesh Kumar, Assistant Prof. Dr. Preeti Gupta, Assistant Prof. Dr. Jawahar Lal and Dr. Alok Kumar Singh*** *for their insightful comments and encouragement, but also for the hard question which incented me to widen my research from various perspectives. A warm thank goes to the departmental Lab Staff for providing friendly and motivating environment during the research work.*

I thank my fellow labmates ***Mr. Gaurav Hitlari, Dr. Manisha Gautam, Dr. Vivek Pandey, Mr. Satya Prakash Gupta, Mr. Ajay Kumar, Mr. Sumit Kumar, Mr. Ashok Kumar, Mr. Gulam Abbas, Mr. Sabir Shekh and colleagues Dr. Rakesh Kumar Sonker (DAP BBAU) and Dr. Ravindra Kumar (DAP BBAU)*** *in for the stimulating discussions, for the sleepless nights we were working together before deadlines, and for all the fun we have had in the last five years.*

My deepest gratitude goes to my affectionate friends ***Mr. Ajay Kumar (DAS BBAU), Mr. Ram Kumar (DAAS BBAU), Mr. Ankit Khokhar (Bhaiya)*** *and* ***Sandeeep Kumar Aladia (CMA, Kapoorthala) (BADE BHAI)*** *for their continuous moral support and encouragement.*

I devote this thesis to my beloved parents ***(Father Shri Ganga Ram Singh and Mother Smt. Asha Devi)*** *for their lot of love, support and sacrifice from the early first day of my journey of life. I also express my sincere hearty thanks to all my brothers* ***(Mr. Nilesh Kumar (Lecturer) and Mr. Rahul Kumar Gautam, Mr. Sandeep Kumar****, sister in law* ***(Mrs. Neha kureel (Assistant Teacher),*** *my sister* ***(Mrs. Vijay Laxmi),*** *and my brother-in-law* ***(Mr. Bramh Pal (Lekpal)*** *for providing me with every kind of support. I would acknowledge the sweet smile of my precious nephew* ***Mr. Namish Singh and Mr. Vaibhav Pratap Singh*** *and dear nieces* ***my sweet Angel Navya Singh and Aditi Singh*** *which inspired and imparted happiness in my life and gave strength to overcome the failures and to start over again.*

Last, but not least, I would like to thank the authors of various research articles and books whose work has been consulted, utilized and cited in my thesis.

Sandhya Singh

Sandhya Singh
(Research Scholar)

ABSTRACT

Nanotechnology is the up-to-date advancement in the world of science stream. The word nanotechnology was first familiarized by Professor Norio Taniguchi of Tokyo Science University, in 1974 at the International Conference on Production Engineering in Tokyo. In recent years, nanotechnology has become one of the most imperative and exhilarating forefront fields in chemistry, physics, engineering and biology. A particle having one or more dimensions of the order of 100 nm or less". In nanotechnology a particle is demarcated as a minor object that behaves as a complete unit in terms of its conveyance and properties. The properties that distinguish the nanoparticles from the bulk material characteristically progress at a critical length of under 100nm. Nanoparticles may or may not exhibition size related properties that fluctuate significantly from those observed in fine particles or bulk materials. Nanoparticles are found in different dimension like as 0-D, 1-D, 2-D, 3-D nanoparticles for various applications. The attention-grabbing and sometimes surprising properties of nanoparticles are therefore largely owing to the great surface area of the material, which dominates the contributions made by the minor bulk of the material. Nanoparticles exhibit important properties owing to quantum confinement, high surface to volume ratio. In case nanomaterials quantum confinement and surface to volume ratio is very important property. In first chapter also discuss the various synthetic technique for synthesis of nanomaterial.

Metal oxides constitute a miscellaneous and attention-grabbing class of materials whose properties cover the entire collection from metals to semiconductors and insulators. Their surface plays tremendous roles in an extremely comprehensive range of phenomena. These metal oxides nanoparticles plays very important role in

many fields of chemistry, physics and materials science for instance catalysts for an assortment of commercially significant reactions. Iron oxide nanoparticles have distinctive magnetic properties for instance superparamagnetism, high coercivity, low Curie temperature, high magnetic susceptibility, etc. In the last few decades, great efforts have been made on synthesis of iron oxide nanoparticles owing to their comprehensive range of applications like magnetic fluids, data storage, catalysis and bio-applications and structure and properties of various phase if iron oxide nanoparticles are discussed in 1st chapter. Application and literature review of iron oxide nanoparticles are explain in brief.

The whole thesis is divided in to 7 chapters. In 1st chapter, general introduction about nanotechnology and metal oxide, iron oxide nanoparticles and objective of research work has been presented. In the 2nd chapter discussion about characterization techniques of nanoparticles and typical applications of these techniques have been discussed. Morphological as well as structural investigation of nanoparticles is examined by XRD, SEM, FTIR, BET, UV-Vis, and PL. Basic principle and instrumentation of these techniques are explained in detail.

The 3erd chapter comprises synthesis of α-Fe_2O_3 nanostructures by chemical co-precipitation followed by annealing at 500 and 600°C for 3 h. Nanoparticle powders were characterized by X-ray diffraction (XRD), scanning electron microscope (SEM), energy dispersive X-ray spectroscopy (EDX), Fourier transform infra-red spectroscopy (FT-IR), particle size distribution, Brunauer Emmett Teller analysis (BET), photoluminescence and UV-Visible spectroscopy. XRD confirmed the formation of crystalline α-Fe_2O_3 nanoparticles while SEM confirmed the formation of rice grain and spherical shapeα-Fe_2O_3nanostructures at 500 and 600 °C. From EDX and FTIR results formation of α-Fe_2O_3 is further established. BET analysis

confirmed the mesoporous behavior of nanoparticles. UV-Visible and photoluminescence spectra have been used to determine band gap and photo-oxidation behavior of dye methylene blue. Both Fe_2O_3-500 and Fe_2O_3-600 nanostructures exhibit exceptionally high photocatalytic activity however the same is higher for Fe_2O_3-500 than that of Fe_2O_3-600 for degradation of methylene blue (Meb).

The 4^{rth} chapter encompasses synthesis of poly vinyl pyrrolidone (PVP) coated magnetite nanoparticles by chemical co-precipitation method. The samples were characterized using X-ray diffraction (XRD), scanning electron microscopy (SEM), energy dispersive X-ray spectroscopy (EDX), Fourier transform infrared spectroscopy (FTIR) and Brunauer Emmett Teller (BET) methods. The surface area, pore volume and pore radius were calculated by the BET analysis. The EDX and FTIR analysis demonstrated the fabrication of PVP coated Fe_3O_4 NPs. The as synthesized Fe_3O_4/PVP has successfully been used as an adsorbent for elimination of Congo red dye in aqueous medium.

Cobalt ferrite has attracted considerable attention in recent years due to its unique physical Properties such as high Curie temperature, large magnetocrystalline anisotropy, moderate saturation magnetization, large magneto restrictive coefficient, excellent chemical stability and mechanical hardness. The 5thchapter presents preparation of cobalt ferrite magnetic nanoparticles by co-precipitation method using Fe(III) and Co(II) in the presence of NH_4OH, at 90˚C. The structure, morphology and magnetic properties of as-prepared were characterized via X-ray diffraction (XRD), High resolution Scanning electron microscope (HRSEM), Energy dispersive x-ray spectroscopy (EDX), Fourier transform Infrared (FTIR) and UV-Visible spectroscopy,. XRD revealed the crystallographic structure of the synthesized sample. HRSEM images have shown the nearly spherical shape and particle size and

morphology of cobalt ferrite nanoparticles. The EDS spectra have shown strong peaks of Fe, Co and O.

In 6thchapter Cd-Ni ferrite nanoparticles with a composition of $Ni_{0.6}Cd_{0.4}Fe_2O_4$ have been successfully prepared via simple co-precipitation technique using sodium hydroxide (NaOH) solution is used as a precipitating agent. The structural and optical properties of the samples were studied using Powder X-ray diffraction (PXRD), Scanning electron microscopy (SEM), Energy dispersive X-ray spectroscopy (EDX), Fourier transform Infrared Spectroscopy (FITR), UV-Visible spectroscopy (UV-Vis), and Fluorescence spectroscopy (FL) measurements. The PXRD analysis of all the samples shows the cubic phase without any impurity peaks. The average particle sizes were calculated by Scherrer's formula. The SEM image shows the agglomeration and flakes type nanoparticles with many void spaces due to exhaust of gases. EDX analysis is used for the elemental analysis of prepared samples (Cd, Ni, Fe, and O). FTIR spectra of the samples show the nature of the chemical bond between metal oxygen bonds (M-O). UV-Vis and PL spectra is used for the band gap calculation and its optical properties.

In 7th chapter complete conclusion of thesis is describe.

CONTENT

Chapter: 1	**1-73**
General Introduction	
1. Introduction	
1.1 Nanotechnology	**2-3**
1.2 Nanoparticles	**4-5**
1.2.1 Types of nanoparticle	**5**
1.2.1.1 0-D nanoparticle	**5-6**
1.2.1.2 1-D nanoparticle	**6-7**
1.2.1.3 2-D nanoparticle	**7-8**
1.2.1.4 3-D nanoparticle	**8-9**
1.3 Properties of nanoparticle	**9-10**
1.4 Why nanoparticle exhibit such property	**10**
1.4.1 Quantum confinement	**10-11**
1.4.2 Surface to volume ratio	**11-12**
1.5 Fabrication method	**12**
1.5.1 Physical method	**12-16**
1.5.2 Chemical method	**17-21**
1.6 Metal oxide nanoparticle	**21-22**
1.7 Iron oxide nanoparticle	**22**
1.7.1 Introduction	**22-23**
1.7.2 Phases of iron oxide nanoparticle	**23-28**
1.8 Ferrite	**28-30**

1.8.1 Types of ferrite	**30-35**
1.8.2 Electrical properties	**35-36**
1.8.3 Magnetic properties	**36-38**
1.9 Application of iron oxide nanoparticle	**38-39**
1.9.1 Heavy metals organic pollutants and dyes removal	**39-40**
1.9.2 Corrosion inhibition on mild steel	**40-41**
1.9.3 Biomedical application	**41-43**
1.10 Literature survey	**43-51**
1.11 Objectives of the present work	**51**
1.12 References	**52-73**
Chapter-2	**74-100**
Characterization Techniques	
2.1 Synthesis procedure	**75**
2.2 Materials used	**75-76**
2.3 Characterization techniques	**76**
2.3.1 XRD	**76-83**
2.3.2 SEM	**83-85**
2.3.3 EDX	**85-86**
2.3.4 FTIR	**86-88**
2.3.5 BET	**88-90**
2.3.6 UV-Vis	**90-92**
2.3.7 PL	**92-97**
2.3.8 Photocatalytic activity	**97-98**
2.4 References	**99-100**

Chapter-3		**101-123**
Effect of annealing temperature on α-Fe_2O_3 nanostructures and optical properties		
3.1	Introduction	**102-104**
3.2	Experimental procedure	**104-105**
3.3	Characterization	**105-106**
3.4	Photocatalytic activity	**106**
3.5	Results and discussion	**106-118**
3.6	Conclusion	**118-119**
3.7	References	**120-123**
Chapter-4		**124-149**
Synthesis and characterization of polyvinyl pyrrolidone (PVP) coated Fe_3O_4 nanoparticles by chemical co-precipitation method and removal of Congo red dye by adsorption process		
4.1	Introduction	**125-127**
4.2	Experimental Section	**127-129**
4.3	Characterization	**129**
4.4	Results and discussion	**130-143**
4.5	Conclusion	**143**
4.6	References	**144-149**
Chapter-5		**150-159**
Synthesis, characterization of Fe_3O_4, $CoFe_2O_4$nanomaterials and its application in photodegradation of Rhodamine B dye		
5.1	Introduction	**151**

5.2	Experimental section	**151-153**
5.3	Characterization	**153**
5.4	Results and discussion	**154-157**
5.5	Conclusion	**157**
5.6	References	**158-159**
	Chapter-6	**160-171**
	Synthesis and characterization of Cadmium doped nickel Ferrite ($Ni_{0.6}Cd_{0.4}Fe_2O_4$) nanoparticles and its optical properties	
6.1	Introduction	**161-162**
6.2	Experimental section	**162-163**
6.3	Characterization	**163**
6.4	Results and discussion	**164-169**
6.5	Conclusion	**169**
6.6	References	**170-171**
	Chapter-7 Conclusion	**172-173**

LIST OF ABBREVIATION

Serial number	Name of compound	Full name
1.	Meb	Methylene blue dye
2.	CR	Congo red dye
3.	Rhb	Rhodamine b dye
4.	Fe_2O_3	Hematite
5.	Fe_3O_4	Magnetite
6.	XRD	X-ray diffraction
7.	FTIR	Fourier transform infrared
8.	SEM	Scanning electron microscope
9.	BET	Brunauer - Emmett - Teller
10.	EDX	Energy dispersive X-ray spectroscopy
11.	UV-Vis	Ultra violet visible spectroscopy
12.	PL	Photoluminance
13.	IONPs	Iron oxide nanoparticles
14.	NPs	nanoparticles
15.	CVD	Chemical vapour deposition
16.	MRI	Magnetic resonance imaging
17.	MNCs	Magnetic nanocomposits
18.	MFe_2O_4	Metal ferrite
19.	γ-Fe_2O_3	Maghemite
20.	PVP	Poly vinyl pyrrolidone
21.	FWHM	Full width half maxima

22.	HRSEM	High resolution scanning electron microscopy
23.	SPION	Superparamagnetic iron oxide nanoparticles
24.	MIONPs	Magnetic iron oxide nanoparticles
25.	MNPs	Magnetic nanoparticles
26.	MG	Malachite green
27.	PANI	Polyaniline
28.	MR	Methyl Red

LIST OF FIGURES

Figure No.

1.1: Shows top-down, bottom-up approach.

1.2: Typical scanning electron microscope (SEM) and transmission electron microscope (TEM) image of different types of 0-D nanoparticles.

1.3: Typical SEM image of different types of 1-D nanoparticles, which is synthesized by several research groups.

1.4: Typical SEM and TEM image of different kinds of 2-D nanoparticles, which is synthesized by several research groups.

1.5: Typical SEM and TEM image of different kinds of 3-D nanoparticles, which is synthesized by several research groups.

1.6: Shows surface to volume ratio.

1.7: Schematic representation of sputtering technique.

1.8: Schematic representation of spray pyrolysis technique.

1.9: Schematic representation of inert gas phase condensation technique.

1.10: Schematic representation of pulsed laser ablation technique.

1.11: Schematic representation of sonochemical reduction technique.

1.12: Schematic representation of hydrothermal technique.

1.13: Schematic representation of solvothermal technique.

1.14: Schematic representation of sol-gel method.

1.15: Schematic representation of chemical vapor deposition method.

1.16: Crystal structure of phases of iron oxide nanoparticles.

1.17: Crystal structure of hexagonal ferrite nanoparticles.

1.18: Crystal structure of garnet ferrite nanoparticles.

1.19: Crystal structure of spinel ferrite.

1.20: Magnetic moment of electron.

1.21: Hysteresis curve of a ferromagnetic material at constant temperature.

2.1: (a)-Methylene blue (b)-Rhodamine b (c)-Congo red Dye (d)-Polyvinyl pyrolidone (PVP).

2.2: Bragg's Low.

2.3: Schematic diagram of X-ray diffraction.

2.4: Full width half maxima (FWHM).

2.5: Represent instrumental broading.

2.6: Schematic diagram of scanning electron microscope.

2.7: Schematic diagram of energy dispersive X-ray spectroscopy.

2.8: Schematic diagram of fourier transform infra-red spectroscopy.

2.9: Schematic diagram of Brunauer-Emmett-Teller.

2.10: Schematic diagram of ultra Violet -Visible spectroscopy.

2.11: Band gap of iron oxide nanoparticle.

2.12: Schematic diagram of (a) Fluorescence (b) Phosphorescence.

2.13: Schematic diagram of fluorescence spectrophotometer.

2.14: Schematic representation of phtocatalytic activity.

3.1: XRD patterns of (a) Fe_2O_3-500 (b) Fe_2O_3-600 composites prepared at 500 and 600°C.

3.2: N_2 adsorption-desorption isotherms of (a) Fe_2O_3-500(b) Fe_2O_3-600 nanoparticles.

3.3: The SEM images of (a) Fe_2O_3-500 and (b) Fe_2O_3-600 nanoparticles. EDX spectra of (c) Fe_2O_3-500 (d) Fe_2O_3-600 nanostructures.

3.4: Particle size distribution of Fe_2O_3 -500 and Fe_2O_3-600 materials.

3.5: FTIR spectra of Fe_2O_3-500 and Fe_2O_3-600 samples.

3.6: UV-Visible spectra of Fe_2O_3-500 and Fe_2O_3-600 nanostructures.

3.7: Band gap energy of Fe_2O_3-500 and Fe_2O_3-600 nanostructures.

3.8: (a) Absorption spectra of Meb solution (100 mL 50 mg/L) in presence of 100mg Fe_2O_3-500 and Fe_2O_3-600nanoparticles.

3.9: Extent of degradation of Meb in presence of Fe_2O_3-500, Fe_2O_3-600 catalyst.

3.10: Pseudo first order kinetics for degradation Meb in presence andFe_2O_3-500 Fe_2O_3-600catalysts.

3.11: PL spectra of Fe_2O_3-500 and Fe_2O_3-600 nanostructures.

3.12: A schematic illustration of the α-Fe_2O_3 photocatalytic reaction mechanism.

4.1: XRD patterns of (a) Fe_3O_4/PVP (1g) (b) Fe_3O_4/PVP (2g) (c) Fe_3O_4/PVP (3g) nanoparticles formed by calcination at 400 °C temperature.

4.2: The SEM image of (a)Fe_3O_4/PVP (1g), (b) Fe_3O_4/PVP (2g) and (c) Fe_3O_4/PVP (3g) NPs. EDX pattern of (d) Fe_3O_4/PVP (1g), (e) Fe_3O_4/PVP (2g) and (f) Fe_3O_4/PVP (3g) NPs.

4.3: FTIR spectra of (a) Fe_3O_4/PVP (1g) (b)Fe_3O_4/PVP (2g) (c) Fe_3O_4/PVP (3g)

4.4: N_2 adsorption-desorption isotherms of (a) Fe_3O_4/PVP (1g) (b) Fe_3O_4/PVP (2g) (c) Fe_3O_4/PVP (3g) nanoparticles.

4.5: BJH plot of (a) Fe_3O_4/PVP (1g) (b) Fe_3O_4/PVP (2g) (c) Fe_3O_4/PVP (3g) NPs.

4.6: Effect of pH on adsorption of Congo red dye on the surface of Fe_3O_4/PVP (1g)

4.7: Effect of contact time and initial metal ions concentration on adsorption Congo red dye on the surface of Fe_3O_4/PVP (1g) at pH 6 on room temperature.

4.8: Langmuir isotherm plot

4.9: Freundlich isotherm plot

4.10: Pseudo first order kinetics

4.11: Pseudo second order kinetics

5.1: XRD of (a) Fe_3O_4 (b) $CoFe_2O_4$.

5.2: SEM image of (a) Fe_3O_4 (b) $CoFe_2O_4$.

5.3: FTIR spectra of (a) Fe_3O_4 (b) $CoFe_2O_4$.

5.4: UV-Visible spectra of (a) Fe_3O_4 (b) $CoFe_2O_4$.

5.5: Photodegradation study of Rhb of (a) Fe_3O_4 (b) $CoFe_2O_4$ and (c) extent of degradation and (d) kinetics.

6.1: XRD spectra (a) pure $Ni_{0.6}Cd_{0.4}Fe_2O_4$ (b) Calcinated $Ni_{0.6}Cd_{0.4}Fe_2O_4$.

6.2: SEM image (a) pure $Ni_{0.6}Cd_{0.4}Fe_2O_4$ (b) Calcinated $Ni_{0.6}Cd_{0.4}Fe_2O_4$ (c, d) EDX spectra of pure $Ni_{0.6}Cd_{0.4}Fe_2O_4$ and Calcinated $Ni_{0.6}Cd_{0.4}Fe_2O_4$.

6.3: FTIR spectra (a) pure $Ni_{0.6}Cd_{0.4}Fe_2O_4$ (b) Calcinated $Ni_{0.6}Cd_{0.4}Fe_2O_4$.

6.4: UV-Visible spectra (a) pure $Ni_{0.6}Cd_{0.4}Fe_2O_4$ (b) Calcinated $Ni_{0.6}Cd_{0.4}Fe_2O_4$ and (a, b) band gap of pure $Ni_{0.6}Cd_{0.4}Fe_2O_4$ and calcinated $Ni_{0.6}Cd_{0.4}Fe_2O_4$.

6.5: PL spectra (a) pure $Ni_{0.6}Cd_{0.4}Fe_2O_4$ (b) Calcinated $Ni_{0.6}Cd_{0.4}Fe_2O_4$.

LIST OF TABLE

Table No.

1.1: Properties of various phase of iron oxide nanoparticle

4.1: Values of the surface area, total pore volume, and the average pore diameter of the samples.

4.2: Values of Langmuir and Freundlich sorption constants for removal of dye Congo red at pH 5 at room temperature.

4.3: Comparison of pseudo-first-order and pseudo-second-order kinetic models for removal Congo red by Fe_3O_4/PVP (1g) in different experimental conditions

Chapter 1
General Introduction

Chapter-1

General Introduction

"This chapter presents a view on different type of 0-D, 1-D, 2-D, 3-D nanoparticles, synthesis method of metal oxides, IONPs and their applications in everyday life. Significant developments of iron oxide nanoparticles for the removal of dyes by photodegradation, adsorption method are critically reviewed. The leading objectives and a brief framework of the up-to-date investigations carried out in this thesis are presented in detail."

1. Introduction:

1.1. Nanotechnology:

Nanotechnology is the up-to-date advancement in the natural world of science stream. The word nanotechnology was first of all familiarized by Professor Norio Taniguchi of Tokyo Science University, in 1974 at the International Conference on fabrication Engineering in Tokyo [1]. The perception of nanotechnology was firstly articulated by the American physicist Dr. Richard Feynman in 1959in the famous talk 'There's plenty of room at the bottom', [2] however in recent years, nanotechnology has become one of the greatest imperative and exhilarating forefront fields in chemistry, physics, engineering and biology. It shows great possibilities for provided that us in the proximate future with numerous breakthroughs that will modify the direction of technological progresses in far-reaching range of applications.

While the connotation of ''nanotechnology" shows a discrepancy from field to field and country to country and is extensively used as a ''catch all" narrative for whatever very lesser. Nanotechnology is ordinarily defined as the understanding, control, and re-establishment of matter on the order of nanometers (i.e., fewer than 100 nm) to procreate materials with fundamentally novel properties and functions [3]. Ordinarily, nanotechnology is the handling of matter on an atomic and molecular scale. One nanometer is a billionth of a meter, or 10^{-9} of a meter, which means that these structures are extraordinary minor. Nanotechnology incorporates two chief methodologies: (i) the ''top-down" approach, in which greater structures are reduced in size to the nanoscale while retaining their distinctive properties devoted of atomic-level control (e.g., miniaturization in the domain of electronics) or deconstructed from bigger structures into their slighter, composite parts and (ii) the ''bottom-up" approach, correspondingly called ''molecular nanotechnology" or ''molecular

manufacturing," familiarized by Drexler et al., [4] in which materials are engineered from atoms or molecular constituents through a procedure of assembly or self-assembly as revealed in Figure 1.1. While maximum of modern-day technologies rely on the ‘‘top-down" approach, molecular nanotechnology embraces great possibilities for breakthroughs in materials and engineering, electronics, medicine and healthcare, energy, biotechnology, information technology, and national security. Nanotechnology is based on the cognizance that particle smaller number than 100 nm impart to nanostructures constructed from them novel properties and behavior. This happens because particles which are slighter than the distinguishing lengths concomitant with precise phenomena often exhibition new chemistry, most important to a different behavior which be contingent on the size. The nanotechnology is perceived as a general cross disciplinary technology; however it has the potential to create a coming "industrial" rebellion that will have a most important impact on society and everyday life, comparable or over and above the influence of electricity and info technology. The intellectual drive in this novel inventiveness promises to counterfeit links across traditional punitive boundaries.

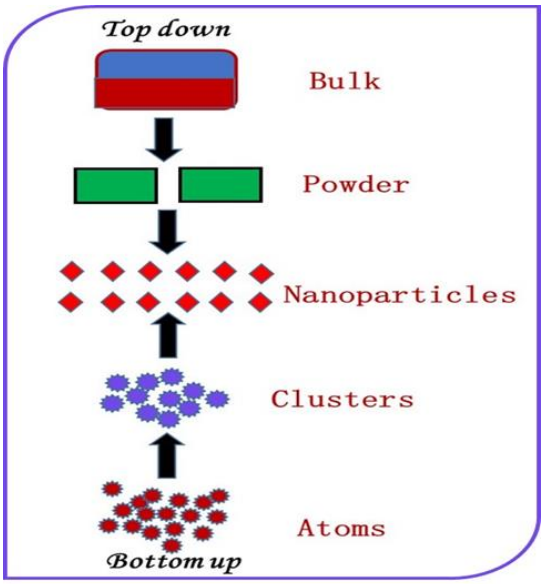

Figure 1.1: Shows top-down, bottom-up approach

1.2. Nanoparticles (NPs):

There is no recognized worldwide meaning of a NPs, conveniently one given in the UK is: "A particle having one or more dimensions of the order of 100 nm or lower" is called as nanoparticle. In nanotechnology a particle is demarcated as a minor object that behaves as a complete entity in terms of its conveyance and properties. Nanoparticle's research at present is an area of concentrated scientific inquisitiveness owing to an extensive assortment of prospective applications of these materials in the fields of biomedicine, optics and electronics on so on. Nanoparticles are of excessive scientific concern as they are efficiently an overpass amongst bulk materials and atomic or molecular structures.

It is further categorized according to size: particles cover an array between 100 and 2500 nanometers while ultrafine particles, conversely, are sized amongst 1 and 100 nanometers. Analogous to ultrafine particles, NPs are sized between 1 and 100 nanometers. The properties that distinguish the NPs from the bulk material characteristically progress at a length of lower than 100 nm. Nanoparticles may or may not exhibition size linked properties that fluctuate significantly from those detected in fine particles or bulk materials. NPs are solid particles at the transitional state that is between atoms/molecules and macroscopic objects. They show novel or upgraded properties based on particular individualities for instance size, dissemination and morphology. Countless materials when formed at nanoscale alter their properties owing to their lesser size and outsized surface area to volume ratio than macro-sized materials. The intensification in surface-area-to-volume ratio, which is a plodding procession as the particle come to be smaller in size, leads to a growing dominance of the behavior of atoms going on the outward of a particle over that of those in the

internal of particle. This affects mutually the properties of particles in separation and its relations with the other different materials.

1.2.1. Types of Nanoparticles:

The particles which are confined in everything the three-dimensional and retain properties that are stuck between the properties of bulk semiconductors and those of distinct molecules [5].

1.2.1.1. Zero dimensional nanoparticles:

A most important feature that distinguishes numerous sorts of nanostructures is their dimensionality. The word ‘‘nano’’ is coming from the Greek term ‘‘nanos’’, which means dwarf [6]. This word ‘‘nano’’ has been allocated to point in the direction of the number 10^{-9}, i.e., one billionth of whichever unit. In the preceding 10 years, compelling improvement has been made in the field of 0-D nanoparticles. A rich assortment of physical and chemical approaches have been established for engineering 0-D nanoparticles with fine-organized dimensions. A moment ago, 0-D nanoparticles such as homogeneous particles arrays (quantum dots), heterogeneous particles arrays, core-shell quantum dots, onions, hollow spheres and nanolenses have been produced by quite a lot of research groups [7-11]. Figure 1.2 shows the images of not the same sorts of 0-D nanoparticles. Moreover, 0-D nanoparticles, such as quantum dots has been comprehensively premeditated in light emitting diodes (LEDs) [12], solar cells [13], single-electron transistors [14], and lasers [15].

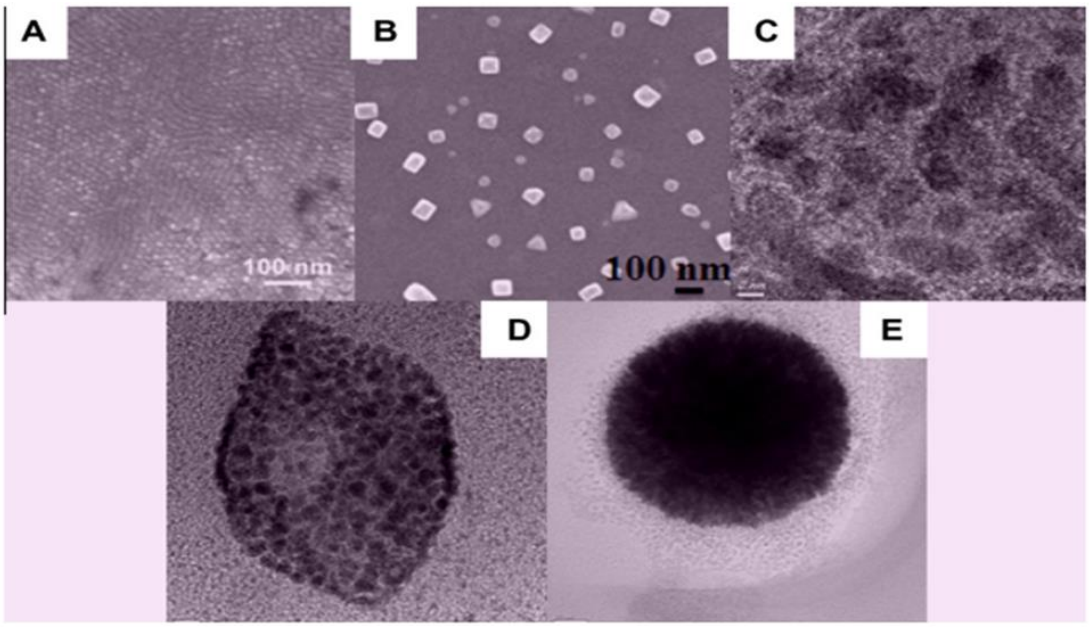

Figure 1.2: Characteristic SEM and TEM image of dissimilar kinds of 0-D nanoparticles. (A) Quantum dots [7], (B) nanoparticles arrays, (C) core-shell nanoparticles, (D) hollow cubes, and (E) nanospheres.[16]

1.2.1.2. One dimensional nanoparticles:

In the previous years, 1-D nanoparticles have enthused an increasing concentration due to their prominence in research and improvements and have a wide-ranging of prospective applications. It is universally accepted that 1-D nanoparticles are perfect structures for reconnoitering a great number of innovative phenomena at the nanoscale and examining the size and dimensionality reliance of serviceable properties. They are furthermore anticipated to play a significant role as mutually be integrated and the important units in producing electronic, optoelectronic, and EEDs with nanoscale dimensions. The field of 1-D nanoparticles for instance nanotubes has achieved a significant courtesy after the groundbreaking work by Iijima [17]. 1-D nanoparticles have a reflective impression in nanoelectronics, nanodevices, nanocomposite materials, alternative energy resources and national safekeeping [18]. Figure 1.3 (A-F) show the 1-D nanoparticles, for instance nanowires, nanorods, nanotubes, nanobelts, nanoribbons, and hierarchical nanostructures, which have been created in other research laboratory [19-33].

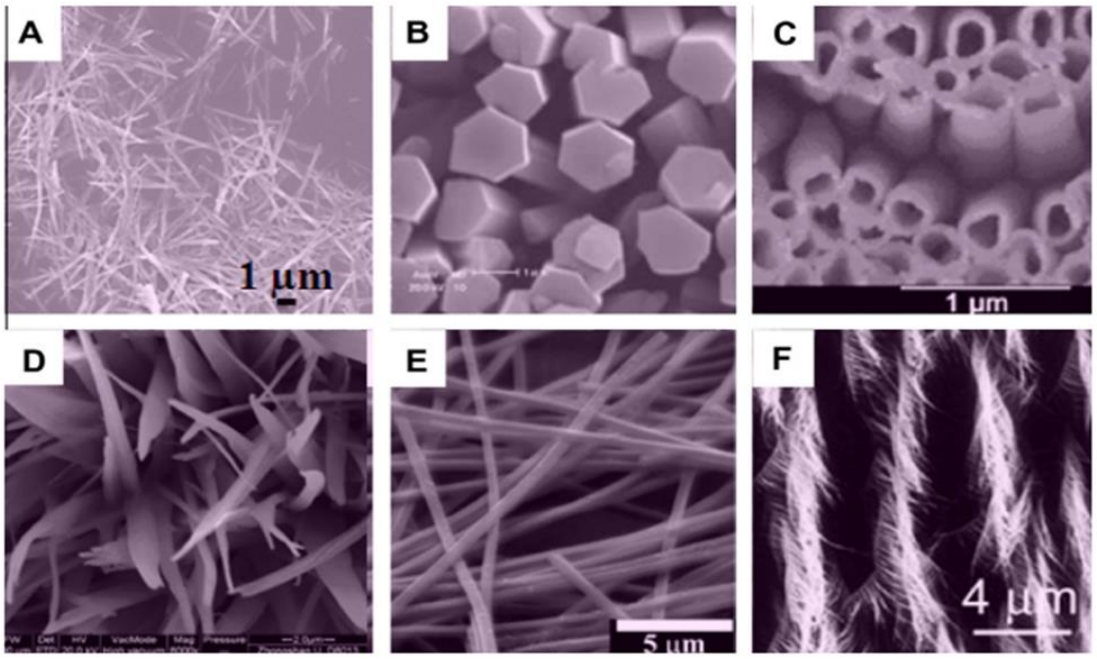

Figure 1.3: Representative SEM image of unlike types of 1-D nanoparticles. (A) Nanowires, (B) nanorods [20], (C) nanotubes [21], (D) nanobelts [22], (E) nanoribbons, [23]and (F) hierarchical nanostructures [24]. [16]

1.2.1.3. Two dimensional nanoparticles:

2-D nanoparticles have twofold dimensions exterior of the nanometric magnitude range. In modern an inordinate length of time, a preparation of 2-D nanoparticles have become a crucial part in materials research, owed to their numerous squat dimensional characteristics not the same from the bulk properties. In the quest of 2-D nanoparticles, substantial research consideration has been concentrated over the bygone hardly any years on the improvement of 2-D nanoparticles. 2-D nanoparticles with assured geometries show distinctive shape-dependent characteristics and succeeding utilization as building blocks for the significant constituents of nanodevices [34-36]. In addition, a 2-D nanoparticles are mainly fascinating not merely for basic considerate of the mechanism of nanostructure progression, but also for examination and developing innovative applications in sensors, photocatalysts, nanocontainers, nanoreactors, and templates for 2-D structures of other materials [37]. Figure 1.4 presents 2-D nanoparticles, such

as junctions (continuous islands), bifurcated structures, nanoprisms, nanoplates, nanosheets, nanowalls, and nanodisks [38-42].

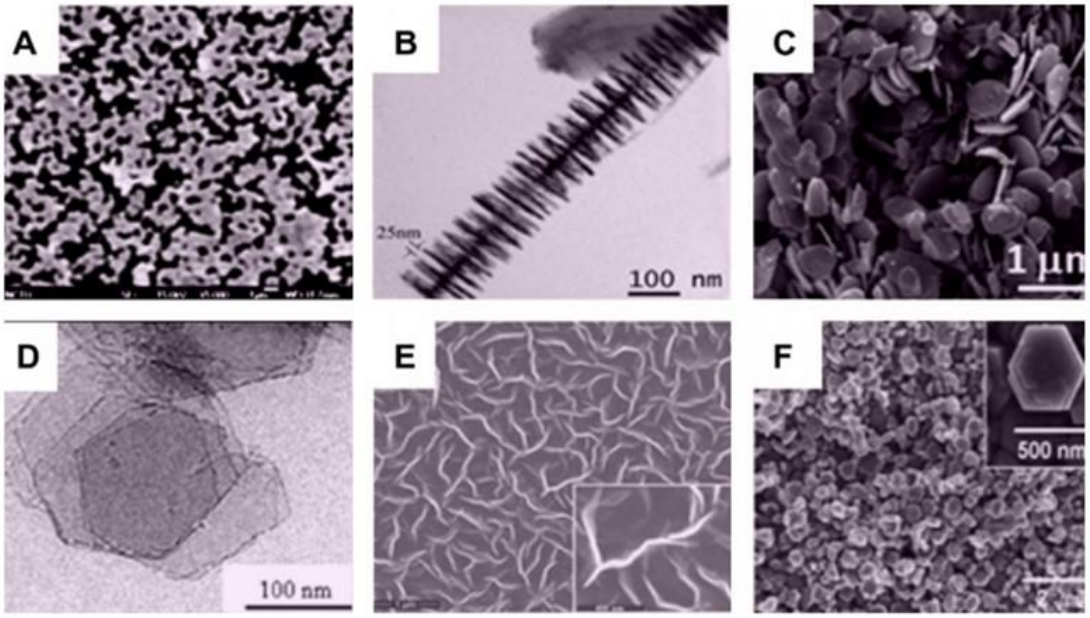

Figure 1.4: SEM and TEM image of unlike categories of 2-D nanoparticles. (A) Junctions (continuous islands), (B) branched structures [39], (C) nanoplates [40], (D) nanosheets [42], (E) nanowalls [43], and (F) nanodisks [44,16]

1.2.1.4. Three-dimensional nanoparticle:

Owing to the excessive precise surface area and additional superior properties over their bulk counterparts ascending from quantum size effect, 3-D nanoparticles have paying attention and research curiosity, and the numerous 3-D nanoparticles have been manufactured in the previous 10 years [45-59]. It is recognized that the behavior of nanoparticles be contingent on the sizes, shapes, dimensionality and morphologies, which are thus the main aspects to their definitive performance and applications. Therefore it is of remarkable attentiveness to synthesize 3-D nanoparticles with a controlled structure and morphology. In addition, 3-D nanostructures are an imperative material owing to its all-inclusive range of applications in the area of catalysis, magnetic material and electrode material for batteries [45-59]. Furthermore, the 3-D nanoparticles have newly fascinated intensive

research interests because the nanostructures have greater surface area and produced sufficient absorption sites for completely involved molecules in a minor space [60]. On the other hand, such materials with absorbency in three dimensions could lead to an improved conveyance of the molecules [60-62]. In Figure 1.5, we show the characteristic 3-D nanoparticles, such as nanoballs (dendritic structures), nanocoils, nanocones, nanopillers and nanoflowers [63-67].

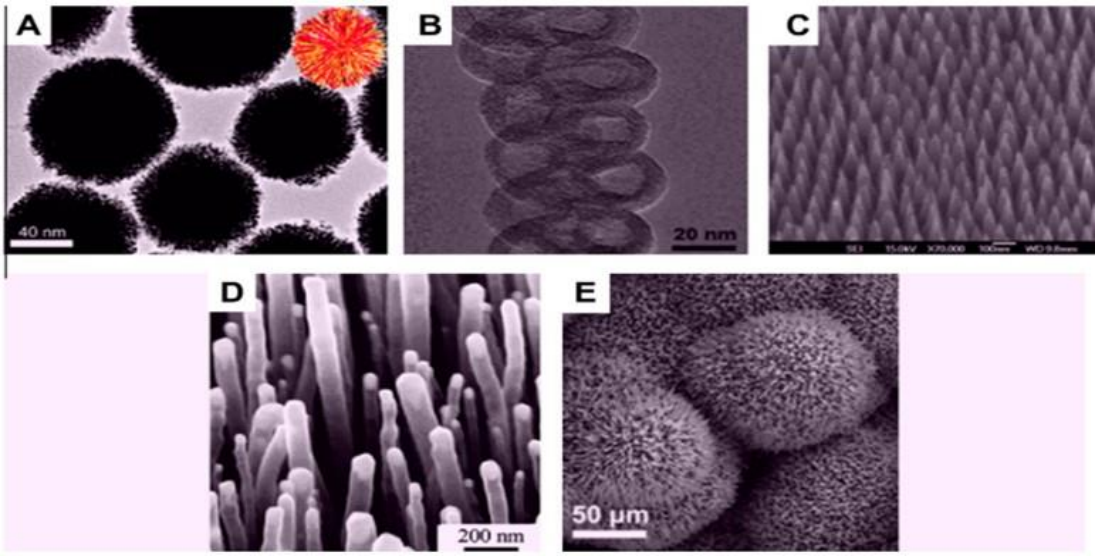

Figure 1.5: Typical SEM and TEM microscopic images of dissimilar kinds of 3-D nanoparticles (A) Nanoballs (dendritic structures) [63], (B) nanocoils [64], (C) nanocones, (D) nanopillers [65], and (E) nanoflowers [66]. [16]

1.3. Properties of nanoparticles:

NPs are of excessive scientific interest as they are, in effect, a connection between bulk materials and atomic or molecular structures. A bulk material has continuous physical properties irrespective of its size but at the nano-scale size-dependent properties are often perceived. *The attention-grabbing and sometimes surprising properties of NPs are therefore largely owing to the excessive surface area of the material, which dominates the contributions made by the minor bulk of the material*.

(a) What is more, nanoparticles have been found to impart specific superfluous properties to numerous everyday products. For instance, the existence of TiO_2 NPs imparts what we call the self-cleaning result due to size being nano-range.

(b) These NPs are rigid, and impart their properties to the polymer (plastic). Nanoparticles have also been involved to textile fibers in order to generate smart and purposeful clothing.

(c) Metal, dielectric, and semiconductor nanoparticles have been designed, as well as hybrid structures (e.g., core-shell nanoparticles) [68]. Nanoparticles prepared of semiconducting material may also be labeled quantum dots if they are slight sufficient (typically sub 10 nm) that quantization of electronic energy levels occurs. Such nanoscale particles are used in biomedical uses as drug carriers or imaging agents.

1.4. Why nanoparticles exhibit such properties:

1.4.1. Quantum confinement:

Quantum confinement is a precise prosperous archetypal for describing the size reliant on electronic structure of nano-sized semiconducting nanostructures. Commonly speaking, it calculates increasing band gaps with reducing particle sizes owing to ever-changing of the band edges. The mainstream of theoretical examinations on quantum confinement out of the ordinary effects were completed on isolated particles with perfect structures and surface terminations. The quantum confinement influence can be perceived once the diameter of the particle is of the magnitude as the wavelength of electron wave function. When the materials are so lesser, their electronic and optical properties differ substantially from those of bulk materials. A particle acts as if it were free when the confining dimension is outsized compared to the wavelength of the particle. Throughout this state, band gap leftovers

at its original energy owing to incessant energy state. However, as the confining dimension reductions and reaches an assured limit, characteristically in nanoscale, the energy spectrum turns to discrete as. As an outcome, bandgap becomes size dependent property. This ultimately results a blue shift in optical brightness as the size of the particles reductions. Specially, the effect defines the phenomenon that results from electrons and electron holes being hugged into a dimension that approaches a critical quantum measurement, called the excitons Bohr radius. In up-to-date application, a quantum dot confines incompletely three dimensions such as a minor sphere, a quantum wire confines in double dimensions, and a quantum well confines in single dimension.

1.4.2. Surface to volume ratio (SA/V):

Surface to volume ratio plays very significant role play in nanotechnology. As the surface area raises the whole term increases but the volume remains same. Nanostructures & nanomaterials have a great fraction of surface atoms per unit volume. The ratio of surface atoms to internal atoms fluctuates dramatically if one successively divisions a macroscopic object into lesser parts. As the scale reductions (keeping the volume constant) the surface area of the material rises as presented in Figure 1.6 and with increases in surface area the capacity of the particles to act together with other particle increases. Also the physical and chemical properties, like interactive forces, reactivity etc. increases. So the SA/V ratio has an important effect on the properties of nanoparticles.

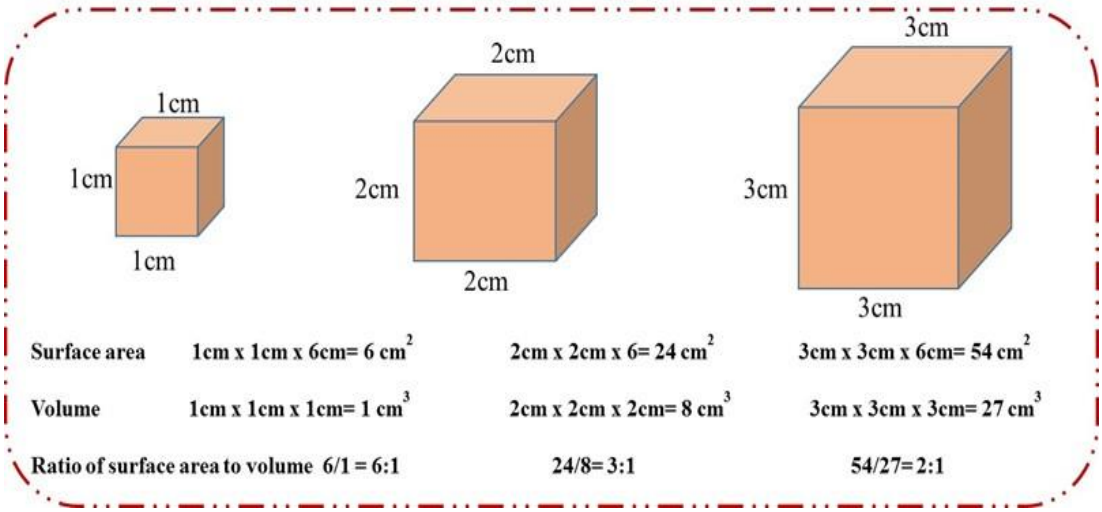

Figure 1.6: Shows surface to volume ratio

1.5. Fabrication methods:

Varieties of methods are available for efficient formation of nanostructures varying the numerous degrees including shape, size and structure. These synthesizing techniques fall into both categories, 'bottom-up' and 'top-down'. In modern years the limits of every approach, in terms of featured size, excellence and in terms of properties, that can be achieved [69]. A diagram that exemplifies the varieties of materials and products that these two methodologies used for is revealed. Metals, metal oxides, sulfides even polymers, core-shell and composite nanoparticles can be synthesized using a number of synthetic techniques, which are broadly classified into two categories, such as physical methods and chemical methods.

1.5.1. Physical methods:

1.5.1.1. Sputtering technique:

At the present time different kind of sputtering system such as ion-assisted deposition, ion beam, reactive, high-target utilization, high power impulse magnetron as well as gas flow sputtering have been used for synthesis of nanoparticles. A characteristic sputtering procedure commonly involves the expulsion of atoms or clusters of nominated materials through subjecting them to a fast-tracked and

exceedingly concentrated beam of inert gas for example helium or argon [70]. A schematic illustration of a typical sputtering system is revealed in Figure 1.7.

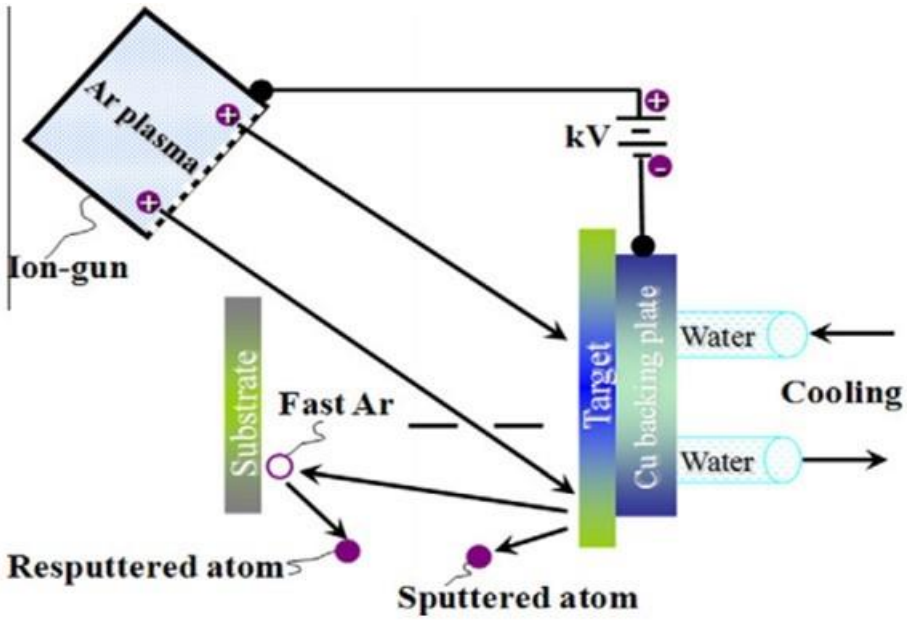

Figure 1.7: Representation of sputtering technique [16]

1.5.1.2. Spray pyrolysis:

Spray pyrolysis (Figure 1.8) is fundamentally a solution procedure in which nanoparticles are set down by spraying a solution on a heated substrate surface, where the component react to produce a chemical compound. The chemical reactants are designated such that the products other than the anticipated compound remain volatile in nature at the temperature of deposition. The spray pyrolysis technique characterizes a very simple and comparatively cost-effective processing method (principally in respect to equipment costs) as compared to different film deposition techniques [71, 72]. Spray pyrolysis synthesis technique offers a tremendously informal technique for synthesizing films of desired composition and does not regime high-quality substrates, chemicals, well-appointed vacuum apparatus and exotic gases. In spray pyrolysis process mainly five parts, such as atomizer, precursor solution, substrate heater, as well as temperature controller are needed. Numerous varieties of atomizers

are frequently used in spray pyrolysis technique, for instance air blast (the liquid is exposed to a tributary of air) [73], ultrasonic (ultrasonic frequencies generate the undersized wavelengths necessary for acceptable atomization) [73] as well as electrostatic (the liquid is exposed to an extraordinary electric field) [73].

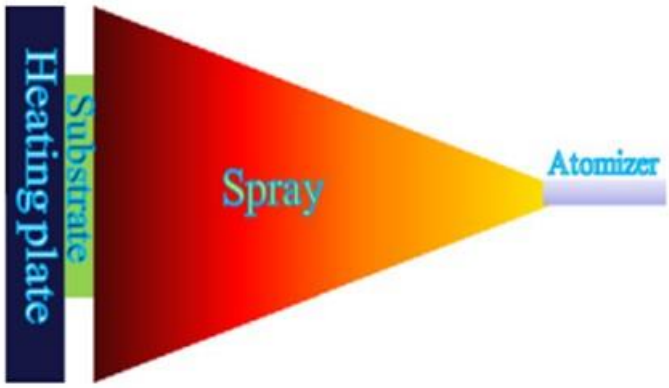

Figure 1.8: Schematic representation of spray pyrolysis technique [16]

1.5.1.3. Inert gas phase condensation technique:

The inert gas phase condensation (IGC) technique (Figure 1.9) is one and only of the greatest auspicious procedure used for the fabrication of low-cost nanomaterial. In general, IGC method has been used to manufacture various single phase metals, semiconductors as well as metal oxide nanoparticles. This method is mainly depends upon disappearance and condensation (nucleation and growth) in a sub-atmospheric inert-gas surroundings for the nanoparticles generation [74, 75] . The production of atoms bunches by IGC procedure through evaporating an originator material, whichever a solitary constituent or a compound, in a gas well-maintained at a low pressure. The disappeared atoms or molecules go through a standardized condensation to form atom clusters (lose energy) through collisions with gas atoms or molecules in the surrounding area of a cold surface to condense on it.

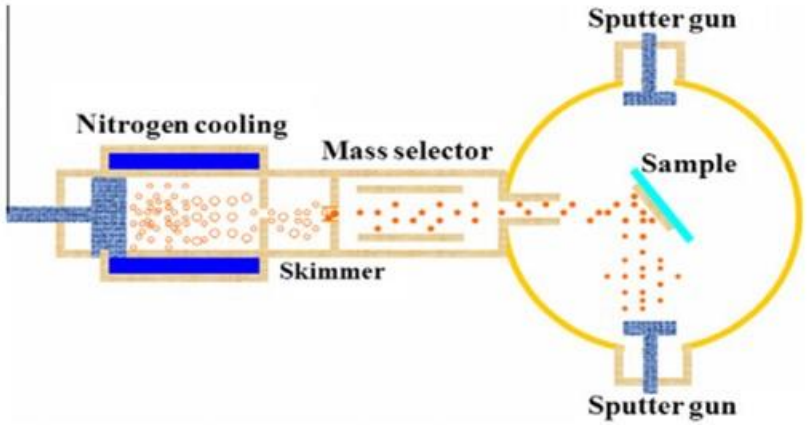

Figure 1.9: Schematic representation of inert gas phase condensation technique [16]

1.5.1.4. Pulsed laser ablation:

As a physical gas-phase technique is used for preparing nanosized particles, pulsed laser ablation in a prevalent technique to synthesize high-purity as well as ultra-fine nanoparticles of whichever composition. In this technique, the material is evaporated using pulsed laser in a compartment occupied with a known quantity of a reagent gas followed by controlled condensation of nanoparticles onto the support. View of a pulsed laser ablation technique for the fabrication of nanoparticles is depicted in Figure 1.10. By means of the materials atoms diffusion from the object to the substrate, they interrelate through gas to form the preferred compound (for instance, oxide of oxygen, nitride for nitrogen or ammonia, carbide for methane, etc.). The pulsed laser disappearance of metals in the chamber is an amendment of the well-known method for the production of metal compounds in a diffusion mist chamber and makes it feasible to formulate nanoparticles of assorted molecular composition for instance mixed oxides/nitrides and carbides/nitrides or combinations of oxides of numerous metals. The elemental composition and size dissemination of nanoparticles can be improved by changing definite experimental structures, together with composition of the inert gas and the substance gas in the chamber and fluctuating the temperature gradient and laser pulse power.

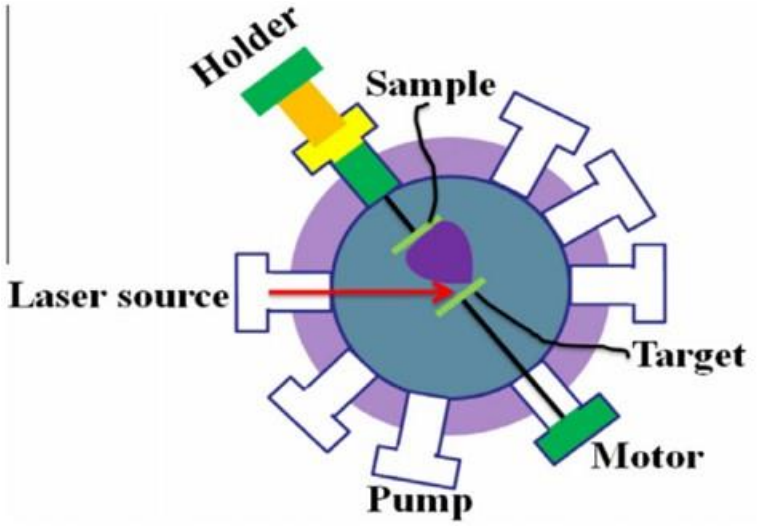

Figure 1.10: Schematic representation of pulsed laser ablation technique [16]

1.5.1.6. Sonochemical reduction:

Sonochemical reduction scheme is extensively used physical method for formation of dissimilar categories of nanoparticles. Figure 1.11 represents the schematic diagram of the sonication system. In this apparatus, a multiwave ultrasonic producer and a barium titanate oscillator of 65 mm diameter have been used for the ultrasonic irradiation. For the duration of the microwave irradiation the vessel was locked. The multiwave ultrasonic producers were operated at 200 kHz frequency with a feedback power of 200 W. The sonication procedure was carried out in a temperature-controlled water bath.

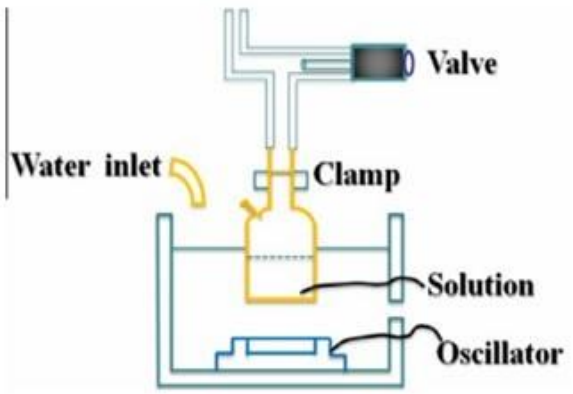

Figure 1.11: Schematic representation of sonochemical reduction technique [16]

1.5.2. Chemical methods:

1.5.2.1. Co-Precipitation

Co-precipitation technique is an easy as well as appropriate approach to synthesize MNPs (metal oxides and ferrites) from aqueous salt solutions by the addition of a base like sodium hydroxide (NaOH) and ammonium hydroxide (NH_4OH) in the inert atmosphere at room temperature or at optimum temperature. The size, shape, and morphology of the magnetic nanoparticles is very greatly be influenced by type of counter ion (e.g., chlorides, sulfates, nitrates), the ratio of ferrous and ferric ion (Fe^{2+}/Fe^{3+} ratio), the reaction temperature, the pH value, as well as the ionic strength of the media [76]. Iron oxide nanoparticles (either Fe_3O_4 or γ-Fe_2O_3) and ferrites are frequently synthesize in an aqueous solution for which chemical reaction of synthesis may be written as:

$$M^{2+} + 2Fe^{3+} + 8OH^- \rightarrow MFe_2O_4 + 4H_2O \quad (1)$$

In Equation 1, M is divalent cations like Fe^{2+}, Mn^{2+}, Co^{2+}, Cu^{2+}, Mg^{2+}, Zn^{2+}, and Ni^{2+}. For the complete precipitation process, pH should be maintained between 8 to 14, with a stoichiometric ratio of 2:1 (Fe^{3+}/M^{2+}) in a nonoxidizing oxygen environment [77]. Nickel-doped cobalt ferrite magnetic nanoparticles (19-32 nm) were synthesized in a standardized aqueous solution in the existence of surfactant at dissimilar calcination temperatures by co-precipitation route [78].

1.5.2.2. Hydrothermal method:

Hydrothermal scheme can be determined as the use of water as reaction medium in a vacuum-packed reaction vessel when the temperature is elevated to 100˚ C. It is used for synthesis of single crystals that be contingent on the solubility of minerals in sizzling water under extraordinary pressure. The complete process of crystal growth is carried out in an autoclave, in which a precursor is provided along

with water. A temperature gradient is upheld at the contradictory ends of the progression vessel so that the burning end liquefies the nutrient as well as the unruffled end causes seeds to take superfluous growth. The hydrothermal technique is more appropriate for better-quality and growth of bigger crystals, while maintaining a virtuous governor over their composition. A schematic illustration of a hydrothermal system is represented in Figure 1.12. The drawbacks of the hydrothermal technique involve the requisite of costly autoclaves, good excellence seeds of a fine size and the unfeasibility of observing the crystal as it produces.

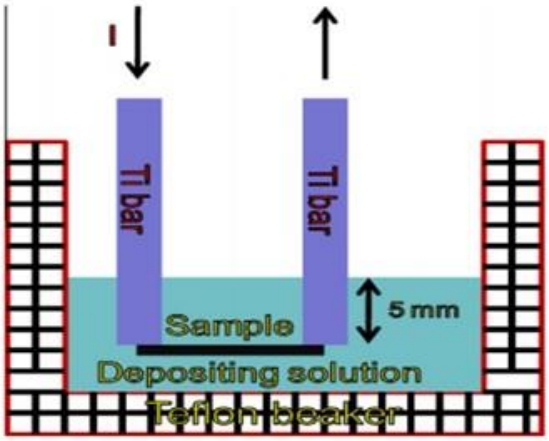

Figure 1.12: Schematic representation of hydrothermal technique [16]

1.5.2.3. Solvothermal techniques:

Solvothermal synthesis method is a universally used chemical method to synthesize the dissimilar varieties of nanoparticles, an experimental sketch is shown in Figure 1.13. Solvothermal synthesis method is very analogous to the hydrothermal route, the merely difference being that the precursor solution is generally not aqueous but this is not at all times. By changing definite experimental parameters, like as reaction temperature, reaction time, solvent type, surfactant type, and type of starting material, it is conceivable to accurate control the size, shape spreading, and crystallinity of metal oxide nanoparticles or nanostructures that achieved.

Figure 1.13: Schematic representation of solvothermal technique [16]

1.5.2.4. Sol-gel technique:

The sol-gel manner (Figure 1.14), also acknowledged as chemical solution deposition, a drizzly chemical synthesis line of attack that can be used to fabrication of NPs by gelation, precipitation, and hydrothermal action [79]. The sol-gel method is extensively used in the fields of materials and chemical science. Such approaches are used first and foremost for the fabrication of materials beginning from a chemical solution (or sol) that acts as the originator for an integrated network (or gel) of either detached particles or linkage polymers. By fluctuating definite experimental parameters together with dopant introduction [80], heat treatment [81] and accurately choosing specific other surfactants, including inverted micelles [82], polymer matrix architecture founded on block copolymers [83] or polymer blends [84], porous glasses [85] and ex situ particle capping [86], it is probable to rheostat the superior size dissemination and steadiness control of quantum-confined semiconductors, metal, MONPs . Despite the above, the basic chemistry of the sol-gel procedure is intricate owing to the different reactivities of the network forming and the network modifying constituents and the wide-ranging selection of reaction parameters [87].

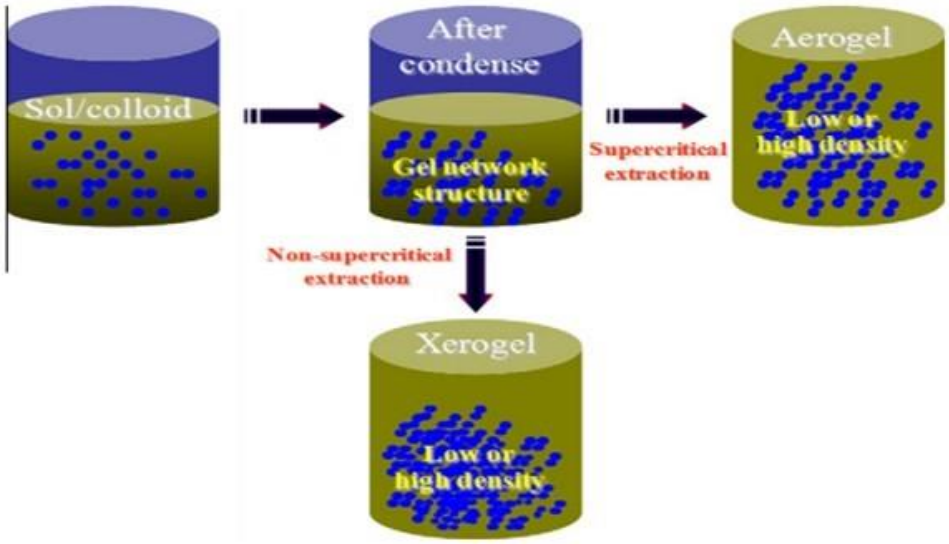

Figure 1.14: Schematic representation of sol-gel method [16]

1.5.2.5. Chemical vapor deposition:

Chemical vapor deposition (CVD) method is a chemical route in which gasiform molecules transform into a solid material, in the form of 0-D, 1-D, 2-D and 3-D nanoparticles, on the surface of a substrate. In a typical CVD manner (Figure 1.15), the substrate is unprotected to one or more hot-blooded originators, which react and/or decompose on the substrate surface to produce the preferred deposit. An elementary CVD process involves of the following five steps:

(a) A predefined mixture of reactant gases and diluent inert gases are positioned into the chamber by the mass flow controller at an identified current rate.

(b) The gas species interchange to the surface site.

(c) The reactants get adsorbed on the surface situate.

(d) The reactants go through chemical reactions with the substrate to form the nanoparticles.

(e) The gaseous reaction products are desorbed and expatriate from the chamber.

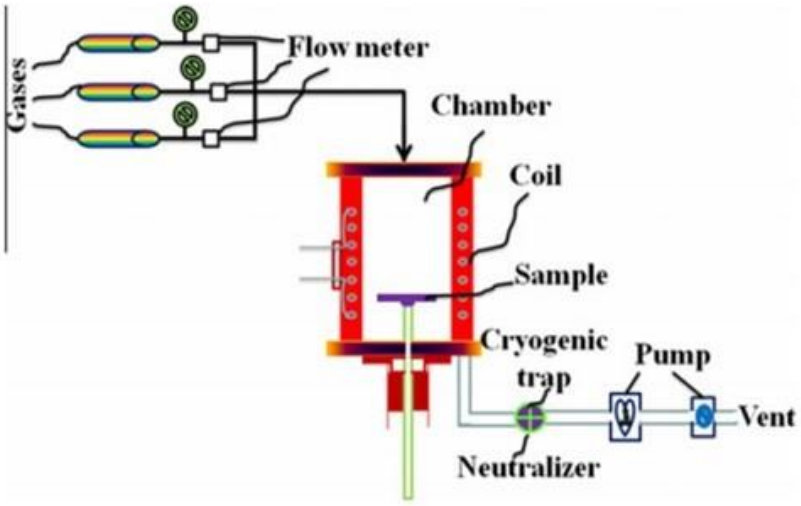

Figure 1.15: Schematic representation of chemical vapor deposition method [16]

1.6. Metal Oxide nanoparticles (MONPs):

Metal oxides constitute a miscellaneous and attention-grabbing class of materials whose properties cover the entire collection from metals to semiconductors and insulators. Their surface plays tremendous roles in an extremely comprehensive range of phenomena. These MONPs plays very vital character in many fields of chemistry, physics and materials science for instance catalysts for an assortment of commercially significant reactions. By the introduction of nanotechnology, the surface depending properties of materials as well as metal oxides alter too much. Owing to their restricted size and an extraordinary density of corner or edge surface sites, metal oxide nanoparticles now can demonstrate unique physical and chemical properties and have received increasing courtesy & recognition for numerous applications. In the modern times, metal oxide nanoparticles have gained great attentiveness due to prospective applications in pharmaceutics, paints, cosmetic, gas sensors, fuel cells, anode of electro-emitting diodes, magnetic materials, thermoelectric material etc. Oxides of transition metals behave as an insulators as well as metals. These metal oxides are the functional constituents as the catalysts used in a number of processes. The use of transition metal oxides as a catalyst is the

technologically advanced and thus the paramount importance in pollution remediation.

1.7. Iron oxide nanoparticles:

1.7.1. Introduction:

Nanoparticles are designed by the inorganic or organic materials, which have several unique properties than bulk materials [88]. Among these, IONPs have distinctive magnetic properties for instance superparamagnetism, great coercivity, squat Curie temperature, more magnetic susceptibility, etc. In the latter hardly any epochs, outstanding efforts have been made on fabrication of IONPs owing to their comprehensive range of uses like magnetic fluids, data storage, catalysis and bio-applications [89-94]. At present, IONPs are also applied in significant biomedical relevance for instance magnetic bio-separation, finding of biological entities, MRI, MFH and targeted drug delivery. It is critical to decide on materials for the production of nanostructure and devices with manageable physical and chemical properties.

Iron oxides nanoparticles including Fe_3O_4 magnetite (ferrimagnetic, superparamagnetic when the size is reduced than 15 nm), α-Fe_2O_3 (hematite, faintly ferromagnetic or antiferromagnetic) and γ-Fe_2O_3 (maghemite, ferrimagnetic) among which magnetite and maghemite are the greatest auspicious and famous phase of IONPs. Then again, it is a challenge to govern the phase, size, shape and steadiness of iron oxide nanoparticles. The magnetic property of the IONPs be influenced by shape and size of the particle. 1-D iron oxide nanoparticles are characteristically used for the stowage of digital and correspondent signals in the area of advanced bendable media [95], however sphere-shaped IONPs with small size have appeared as main nanomaterials for biomedical uses owing to their superparamagnetic property.

However, insignificant size of IONPs have a great propensity to form agglomerates to diminution the energy related with the extraordinary surface to

volume ratio. Furthermore, IONPs can be simply oxidized in air and resulting in the damage of magnetism. Therefore, the surface modification process is crucial to stabilize the MIONPs. These approaches comprise grafting or coating with organic molecules, consisting small organic molecules, polymers and biomolecules or coating with an inorganic coat (silica, metal and carbon). The important properties of the magnetic nanoparticles are express to their extra-large surface area, magnetic property, small toxicity, and large recoverability. However, the accumulation of magnetic nanoparticles in aqueous solutions confines their practical relevance. Therefore surface modification is carried out by chemical or physical interaction of nanoparticles with inorganic or organic materials.

1.7.2. Phases of iron oxide nanoparticles:

IONPs are categorized as the consequential transition metal oxides taking benefit of technical prominence. In natural surroundings, iron oxides can be found in several dissimilar forms [96]. Sixteen clean phases of iron oxides are found, particularly, oxides for instance magnetite, hematite, iron oxide beta phase and maghemite, hydroxides such as iron(III) hydroxide or bernalite, iron(II) hydroxide, oxyhydroxides for example geothite, akaganetite, lepidocrocite, feroxyhyte are known to date. Trivalent oxidation state, distinct colors and little solubility are characteristics of these compounds [97]. Among all iron oxides and hydroxides, only schwertmannite (iron-oxyhydroxysulfate) and ferrihydrite (hydrous ferric oxyhydroxide) are poorly crystalline. Different phases of iron oxide nanoparticles are shown in Figure 1.16.

1.7.2.1. Magnetite:

Magnetite is one of the most significant phases of iron oxide, black in color and ferromagnetic in which both Fe (II) and Fe (III) ions are existing. Even though

stoichiometric ratio in magnetite has Fe (II)/ Fe (III) equals to 0.5 but magnetite, which is commonly non-stoichiometric results in a Fe^{3+} lacking layer. Crystal structure of magnetite has an inverse spinel with a face-centered cubic (FCC) unit cell having an edge length of 0.839 nm and 32 oxygen atoms. In case of inverse spinel crystal structure Fe^{2+} and half of the Fe^{3+} occupy octahedral sites as well as the other half of the Fe^{3+} occupies tetrahedral sites. Divalent iron atoms have a preference to take octahedral sites to achieve larger crystal field stabilization energy. On the other hand, the trivalent iron atoms occupy both octahedral as well as tetrahedral sites (crystal field stabilization energy=0). The tangible crystal types of magnetite consist of octahedron and rhombodecahedron with surface area in the range of 4 to100 $m^2 g^{-1}$[98].

1.7.2.2. Hematite:

The second significant and prevalent phase of iron oxide is hematite (α-Fe_2O_3). Structure of Hematite is analogous to the corundum (α-Al_2O_3), consisting of a compact arrangement connected with Fe^{3+} ions in octahedral coordination with oxygens in hexagonal closest packing. The crystal system of hematite is hexagonal type with the value of lattice parameters of a=5.0346 Å, c=13.752 Å, however crystals consist of lots of forms. The structure can also be recognized as the stacking of Fe^{3+} ions sheets in the middle of two-fold closed-packed layers of oxygens, fused together by covalent bond. The structure in addition has a three-D outline developed along with trigonally distorted octahedral FeO_6, interconnected to thirteen neighbors by one and only face, three edges and six vertices. Because Fe is in a trivalent state (ferric Fe), every one of the oxygens is in reality bonded with just two Fe ions, and so, only two out of three obtainable oxygen octahedrons are occupied. This specific arrangement have tendency to make the structure neutral with no deficit or charge excess. Hematite's fixed surface area ranges from 10 to 90 $m^2 g^{-1}$[98].

1.7.2.3. Goethite:

Goethite is general phase of iron oxy-hydroxide, α-FeO(OH) shows an orthorhombic crystal structure through lattice parameters of a=9.95 Å, b=3.01 Å, c=4.62 Å. This structure is a 3-D structure manufactured up with $FeO_3(OH)_3$ octahedral forming big tunnels, dissemination out along the direction (0 1 0) whereas hydrogen atoms are situated. Everyone octahedron is interrelated to eight adjacent octahedron by four edges and three vertices. Oxygen atoms are in tetrahedral environs, whichever OFe_3H or OFe_3H (bond). Shapes of Goethite phase can be found in nature are different; conversely, its morphology frequently is acicular. Its precise surface area has been reported from 8 to 200 m^2g^{-1} [98].

1.7.2.4. β phase:

Ferrihydrite is commonly habituated to elucidate both 2- or 6-line ferrihydrite, which have two or six recognizable extensive reflections in a diffraction pattern. Ferrihydrite has unlike chemical formulae, containing $Fe_5HO_8{\cdot}4H_2O$, $Fe_5(O_4H_3)_3$, $Fe_2O_3{\cdot}2FeOOH_2{\cdot}6H_2O$ as well as $5Fe_2O_3{\cdot}9H_2O$ [99]. The shape of ferrihydrite is sphere-shaped and unlike other phases it forms only as nano crystals representing extraordinary particular surface areas in the range of 100 to 700 m^2g^{-1}[98]. The structure of ferrihydrite continues to be controversial as the lowermost degree of order hinders the explanation of the structure.

1.7.2.5. Wustite:

Wustite (FeO) is one more phase of iron oxide with a cubic unit cell. This phase is steady under warm air equilibrium at high temperatures (above 843 K) and small pressures. The big O^{2-} anions form a close crowded fcc sublattice through the minor Fe^{2+} cations which occupied the interstitial positions. Just about everything, Fe ions are octahedrally coordinated to oxygen atom [100]. In wüstite, the oxygen and

iron (1 1 1) planes form ultimate two-D hexagonal lattices with an inter-atomic separation of 3.04 Å, which typically resembles to the lattice constant of the hexagonal unit cell on the unreformed FeO (1 1 1) surface. Alongside the (1 1 1) direction the iron and oxygen (1 1 1) planes evolve the cubic ABC stacking order with an interlayer distance of 1.25 Å. The distance of the Iron-oxygen bond is 2.16 Å.

1.7.2.6. Akaganeite:

Akaganeite (β-FeOOH) is an iron oxyhydroxide phase by means of biggest tunnel-type structure amongst totally other phases. In this structure, iron atoms are forcefully joined to the framework. In akaganeite the octahedral sites are normally occupied by FeH and Cl and maybe H_2O is presumably to be found in the tunnels (Cl is considered as an impurity) [101].

1.7.2.7. Lepidocrocite:

Crystal structure of lepidocrocite form (γ-FeO(OH)) is orthorhombic, is gathered by twice layers of Fe-octahedral, and hydroxyl groups which occupied their peripheral surfaces permitting the development of hydrogen bonding stuck between the layers. It is whispered that hydrogen atoms are placed at the midpoints of inversion and occupied the identical distances from dual oxygen atoms of the neighboring layers, therefore generating unceasing O–H–O–H–O chains with hydrogen bonds regularity. The leading morphology of lepidocrocite is whichever lath-like or tabular plus the surface area are generally between 15 and 260 m^2g^{-1} [92]. Table 1 [98, 102] summarizes complete information various phases of iron oxide nanoparticles.

Table 1.1: characteristic properties of numerous phases of IONPs

Iron oxide Phase	**Chemical formula**	**Oxidation state**	**Crystal structure**	**Magnetism**	**Colour**
Magnetite	Fe_3O_4	+2, +3, (2.67-average)	Cubic (a=b=c)	Ferrimagnetic	Black/brownish black
Hematite	α-Fe_2O_3	+3	Rhombohedral (a=b=c, α≠β≠γ)	Weakly Ferro/antiferromagnetic	Red
Iron oxide β phase	β-Fe_2O_3	+3	Cubic (a=b=c)	Paramagnetic	-
Maghemite	γ-Fe_2O_3	+3	Cubic or tetragonal (a=b=c)	Ferrimagnetic	Reddish brown
Geothite	α-FeO(OH)		Orthorhombic (a≠b≠c, α=β=γ)	Antiferromagnetic	Yellowish brown
Akaganeite	β-FeO(OH)		Monoclinic (a≠b≠c, α=β=90˚,γ=120˚)	Antiferromagnetic	Yellowish brown
Lepidocrocite	γ-FeO(OH)		Orthorhombic (a≠b≠c, α=β=γ=90˚)	Antiferromagnetic	Orange
Feroxyhyte	δ-FeOOH		Hexagonal (a=b≠c,α=β=90˚, γ=120˚)	Ferrimagntic	Red-brown
Iron (III) hydroxide (Barenalite)	$Fe(OH)_3$		Orthorhombic (a≠b≠c, α=β=γ=90˚)	-	Dark green
Iron (II) hydroxide	$Fe(OH)_2$			-	Green
Ferrihydrite	$Fe_5HO_8.4H_2O$		Hexagonal (a=b≠c,α=β=90˚, γ=120˚)	Superferromagntic	Red-brown
Wustite	FeO	+2	Cubic (a=b=c)	Antiferromagnetic	Black

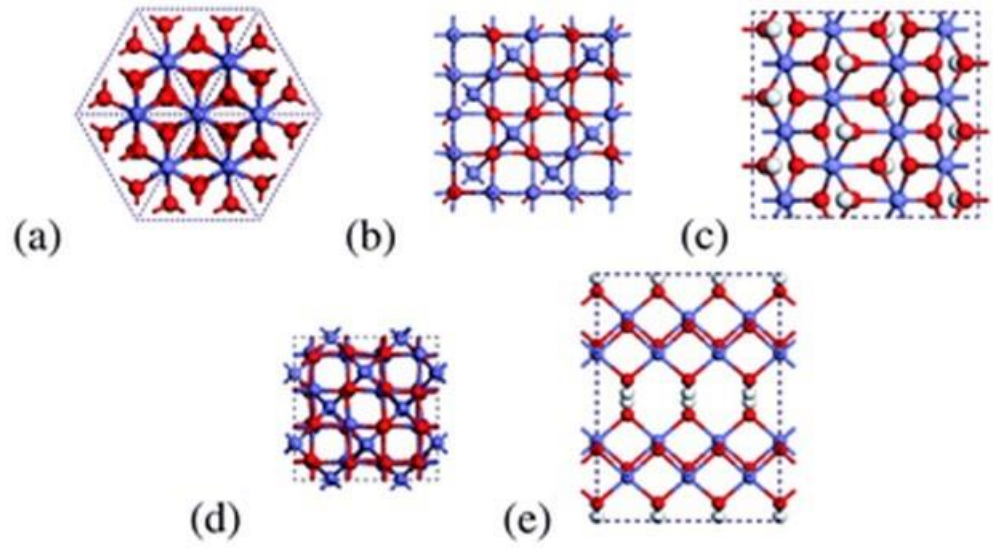

Figure 1.16: Crystal structure of phases of IONPs: (a) hematite, (b) magnetite, (c) goethite, (d) maghemite, (e) lepidocrocite. [103]

1.8. Ferrites:

The ferrites are magnetic ceramics consisting iron oxide and metal oxides, and have been used in numerous devices such as long-lasting magnets, memory storing devices, micro-wave devices and telecommunication equipment. The importance of ferrites material lies in the fact that they own extensive assortment of electrical and magnetic properties. The extraordinary electrical resistivity, slight eddy current and dielectric destruction, highest saturation magnetization, maximum permeability, higher Curie temperature etc. are the outstanding electrical as well as magnetic properties of ferrites [101]. Ferrites with such mishmash of electrical insulator and magnetic conductor are imperative magnetic materials which are not be replaceable by other magnetic materials. The benefit of ferrite is that they have greater usefulness and little charge and are informal for production than other materials. On account of their sundry and interesting applications in extensive technological and scientific fields, the fabrication and analysis of these materials have become significant. The

rudimentary electrical and magnetic properties of ferrite are sensitive to preparation and related parameters, kind and quantity of dopant, dissemination of cations over the existing sites. The dopant selection is also essential conditions in governing the properties of ferrite materials [104, 105].

The rock-strewn were found in the region of Magnesia in Asia significant, and hence the term of minerals is Magnetite, Fe_3O_4, is in a structural class of compounds so-called the spinels with the composition $MeFe_2O_4$ where Me is a divalent cation, Fe^{2+} in the instance of magnetite. The unsurprisingly occurring ferrites, for instance magnetite are magnetically lenient. The research efforts at that time for generating the analogue lenient magnetic materials were not efficacious until in 1930's when the first artificial ferrites were developed self-sufficiently in Japan and Netherlands [106]. Ferrites materials were synthesized as stretched out as 1859, active research on the synthesis of ferrite for radio frequency applications did not start up to 1933. The most important pioneering work executed by Late. Dr. Snoek [107] as well as his associates in 1948. The enhancement of ferrite carry on rapidly subsequently the 2^{nd} world war. In the previous 6 to 7 decades ferrites are comprehensively considered from academic and technological point of view by numerous researchers [108-110]. Since then, intensive hard work have been dedicated to this research area, which directed to the extraordinary developments in both science and technologies of ferrite materials. Distinctive electric and magnetic properties of the ferrite materials have shown wonderful technological applications at room temperature such as data storage devices, magnetic sensors, transformer cores, actuators, targeted drug delivery, medical diagnosis, etc. [111-115]. More number of methods are obtainable for the synthesis of ferrites, the greatest frequently used technique is ceramic procedure. The adjustments in the properties for preferred applications have been brought by switching unlike type and quantity of substituent's [104, 116]. The foregoing two

decades have witnessed a marvelous increase in the attention of the academics and the industry in materials that are appropriately described by this novel vocabulary nanostructured materials. Unsurprisingly this in turn to the study ferrites at nano-scale a fairly attention-grabbing subject both from the fundamental and application points of view.

These ferrite nanoparticles have fascinated much consideration owing to their surface and quantum confinement effects contingent upon great surface-to volume quotient and size-dependent properties, correspondingly. These parameters resulted in dissimilar modifications in the physical and chemical properties of ferrites [117, 118] and make them stretchy to be used in dissimilar applications in the current technology. Consequently, the chemical production of ferrites has become the emphasis of varied studies. Ferrite nanoparticles can be manufactured by dissimilar showery chemical methods, such as the co-precipitation [119], hydrothermal synthesis [120], micro-emulsion synthesis [121] spray pyrolysis [122], citrate precursor technique [123] and sol gel method [124] etc.

1.8.1. Classification of ferrites:

Ferrites are a just fine established collection of magnetic semiconductor materials. Ferrites are categorized by the fallowing types.

1.8.1.1. On the basis of Crystal structure:

According to crystal structure, ferrites are of three kinds namely hexagonal ferrite, garnet and spinel ferrite [125]. By quality of their crystal structure they can accommodate variability if cations at offered sites enabling extensive variation in electrical and magnetic properties.

(a) Hexagonal ferrite:

Hexagonal ferrite was first time acknowledged by Went, Rathenau, Gorter & Van Ostershout 1952 [126] and Jonker, Wijn & Braun 1956. The collection of ferrites

which contain hexagonal crystal structures is denoted as hexagonal ferrites. Hexagonal ferrite are four types and designated as M, W, Y and Z. The crystal and magnetic structure of the dissimilar categories of hexagonal ferrites are extraordinarily complex, as presented for the most significant M-type $SrFe_{12}O_{19}$ in Figure 1.17. The rudimentary unit cell encloses 10 oxygen stratums, sequentially manufacture from 4 blocks, S (spinel), R (hexagonal), S* and R*. S* and R* have the same atomic arrangements as S and R, but are rotated 180° about the c axis with respect to S and R. An S or S* block be made up of double O^{2-}layers; while an R or R* block encloses three O^{2-} sheets, with one oxygen site in the intermediate stratum switched by a Sr^{2+} ion [127].

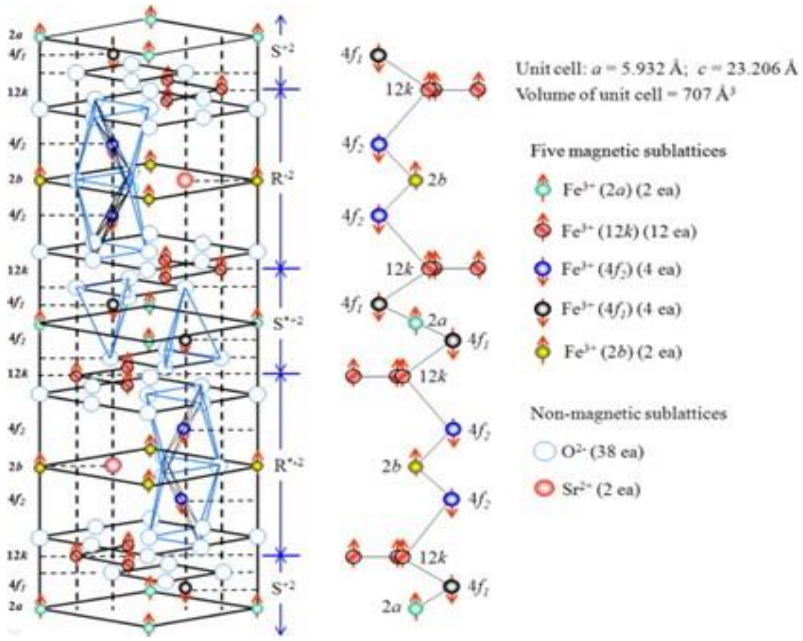

Figure 1.17: Crystal structure of hexagonal ferrite nanoparticles [128]

(b) Garnet:

The crystal structure of garnets have orthorhombic crystal structure (oxygen polyhedra, surrounding the cations) but with trivalent cations (together with rare earth and Fe^{3+}) occupying tetrahedral (d), octahedral (a), or dodecahedral-a 12-sided distorted polyhedral-(c) sites. The orientations of which are presented Figure 1.18.

The universal formula of garnets is $M_3{}^cFe_2{}^aFe_3{}^dO_{12}$, or $(3M_3O_3)c(2Fe_3O_3)a(3Fe_2O_3)d$, where M is a rare earth metal ion or an yttrium ion (such as nonmagnetic yttrium or a magnetic rare earth for example from lanthanum through ytterbium) and the superscripts c, a, d, denote as a dodecahedron, octahedron and tetrahedron in that order.

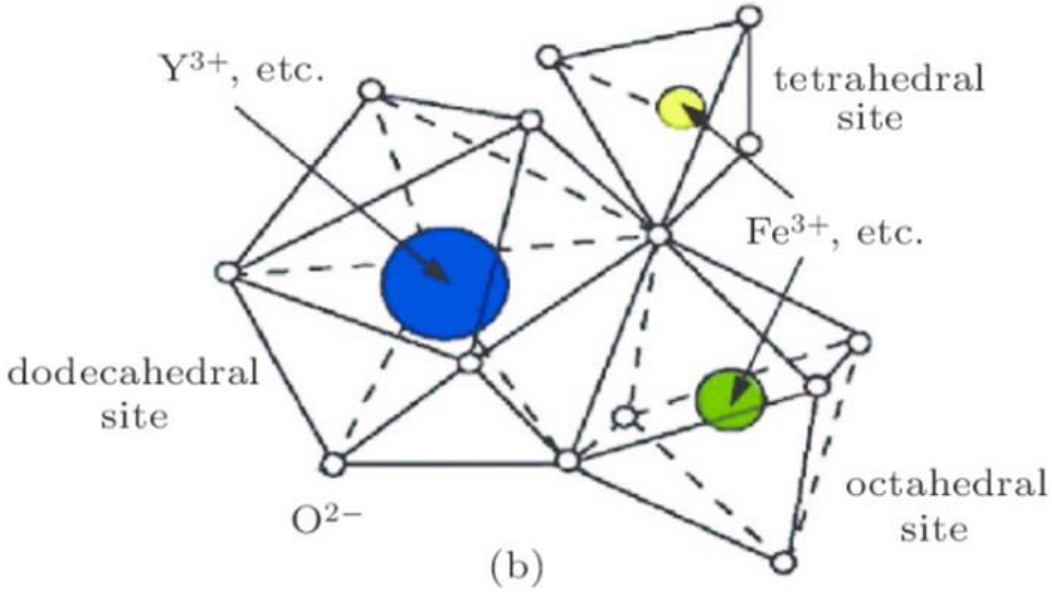

Figure 1.18: Crystal structure of Garnet ferrite nanoparticles [129]

(c) Spinel ferrite:

The generic formula of spinel ferrite having $MeFe_2O_4$ in which Me and Fe show tetrahedral and octahedral cation sites, in that order, and O designates the oxygen anion site. They are also known as cubic ferrites. In spinel ferrites, the relatively large oxygen anions form a cubic close packing with ½ of the octahedral and ⅛ of the tetrahedral interstitial sites engaged by metal ions. Spinel ferrites with the formula $MeOFe_2O_3$ or $Me^{II}Fe^{III}{}_2O_4$ where Me^{II} symbolizes a divalent metal cation for instance Mn, Fe, Co, Ni, Cu, Zn, Cd, Mg, and Fe^{III} is the trivalent iron cation, have the same crystallographic structure as the mineral spinel ($MgAl_2O_4$), which was investigated by Bragg [130, 131]. The unit cell of spinel ferrite goes to the cubic

structure and offerings itself the cube created by 8 $MeOFe_2O_3$ molecules and be made up of 32 of O^{2-} anions. The anionic oxygen form the close face centered cube (fcc) packing involving in 64 tetrahedral (A) and 32 octahedral (B) unoccupied spaces partially populated by Fe^{3+} and Me^{2+}cations [120]. Figure 1.19 (a) symbolizes Spinel unit cell structure, (b) characterizes octahedral interstice (B site: 32 per unit cell, 16 occupied), and (c) tetrahedral interstice (A site: 64 per unit cell, 8 occupied). Figure 1.19 (a) indications the crystal structure of spinel structure. In Figure 19 (a) the ionic locations are the identical in octants sharing only one edge and dissimilar in octants sharing a face. Each one octant encloses 4 Oxygen ions. In Figure 1.19 (a) ionic locations in only double adjacent octants are shown, where the octant on the left consist octahedral and the one on the right contains tetrahedral sites. According to the dissemination of cations [107], there are the subsequent:

Types of spinels:

(a) Random Spinel:

The divalent metal ions Me^{2+} as well as trivalent Fe^{3+} ions are disseminated at both tetrahedral A site and octahedral B site then the ferrite is characterized as random spinel ferrite. General structure of random spinel is epitomized by the formula $Me_{1-}{}^{2+}Fe_{1-}{}^{\delta 3+}$ $Me_2{}^{2+}Fe_{2-}{}^{\delta 3+}O_4{}^{2-}$. It has an in-between cation distribution, symbolized as $[Fe_{0.67}Me_{0.33}]_{tet}[Me_{0.67}Fe_{1.33}]_{oct}O_4$. It has been recognized nowadays that in unit cell of spinel configuration eight tetrahedral and sixteen octahedral sites are engaged by metal ions and finally normal and inverse spinel signify the extreme circumstances. The dissemination of ions stuck between twice sorts of sites is investigate by a delicate balance of contributions, for instance the dimensions of ionic radii, their electronic configuration and the electrostatic energy of the lattice. The greatest known specimen of random spinel ferrite is copper ferrite.

(b) Normal spinel:

A material with the normal spinel structure having universal formula $Me(Fe_2)O_4$ has completely the divalent metal (Me^{+2}) cations occupy tetrahedral (A) sites as well as the trivalent metal (Fe^{+3}) cations occupy octahedral [B] sites. This can be characterized by the formula $[Me]_{tet}[Fe_2]_{oct}O_4$.

Specimens of normal spinel are:

$MgO.Al_2O_3 = MgAl_2O_4$ (normal, parent mineral)

$ZnO.Fe_2O_3 = ZnFe_2O_4$ (normal)

$FeO.Al_2O_3 = FeAl_2O_4$ (normal)

$CoO.Al_2O_3 = CoAl_2O_4$ (normal)

$MnO.Al_2O_3 = MnAl_2O_4$ (normal)

$NiO.Al_2O_3 = NiAl_2O_4$ (normal)

(c) Inverse spinel:

In case of inverse spinel structure, $Fe(MeFe)O_4$, the divalent metal cations has sturdier affinity for occupy octahedral [B] sites and the trivalent metal cations are similarly distributed in the tetrahedral site (A) and remaining octahedral site [B]. This can be denoted by formula, $[Fe]_{tet}$ $[Me,Fe]_{oct}O_4$. For instance cobalt ferrite ($CoFe_2O_4$) is predominantly an inverse spinel with a formula; $Co_xFe_{1-x}(Co_{1-x}Fe_{1+x})O_4$ (with x = 0) where, x is the cation spreading factor which describes the portion of tetrahedral sites engaged by Co^{2+} cations.

$CoO.Fe_2O_3 = FeCoFeO_4$ (inverse)

$NiO.Fe_2O_3 = FeNiFeO_4$ (inverse)

$MgO.Fe_2O_3 = FeMgFeO_4$ (inverse)

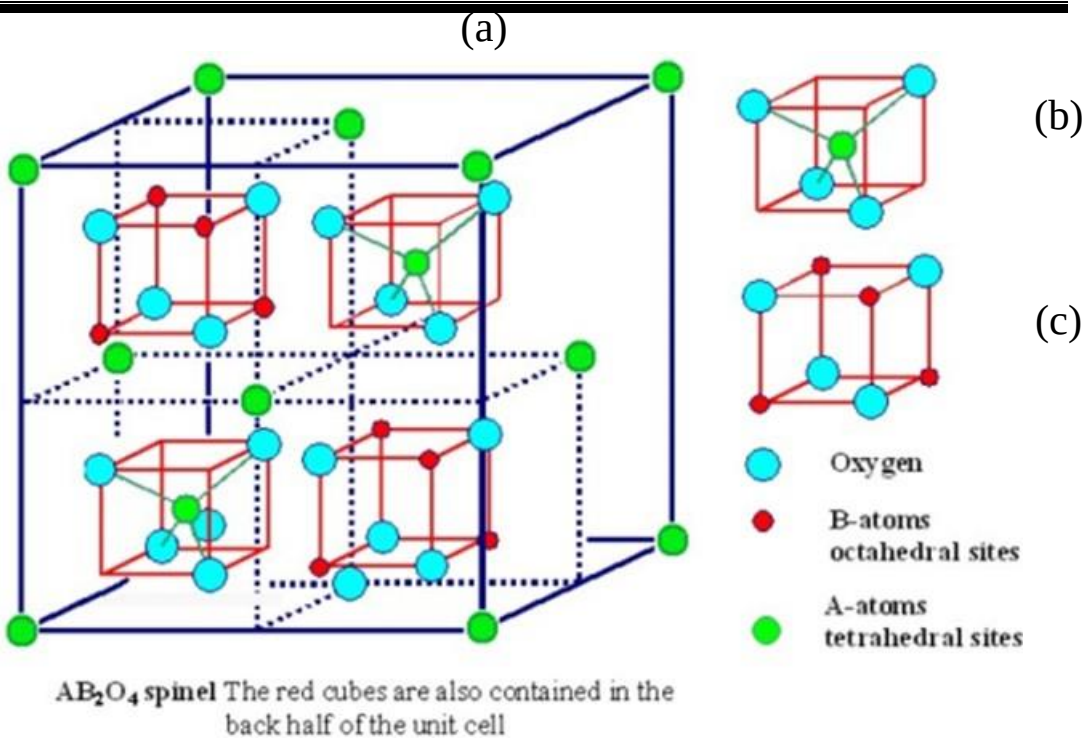

Figure 1.19: Crystal structure of Spinel ferrite [132]

1.8.2. Properties of spinel ferrites:

1.8.2.1. Electrical properties of spinel ferrites:

Spinel ferrites are most significant over conventional magnetic materials because of their extensive variability of applications. These materials have small electrical conductivities as compared to other magnetic materials and therefore they find varied use at microwave frequencies. Spinel ferrites, in common are semiconductors with their resistivities lying in the range between 10^{-2} and 10^{-11} ohm.cm^{-1}[133]. The conductivity is owing to Fe^{2+} and Me^{3+}metal ions. In general, the presence of Fe^{2+} outcomes in n-type behavior and M^{3+} in p-type behaviour. The conductivity arises owing to the movement of the additional electron or the positive hole over and done with the crystal lattice. The mobility is explain by a hopping mechanism, in which the charge importers jump from one ionic site to the additional. On this basis, the semiconducting nature of nickel and cobalt ferrite has been efficaciously treated by Jonker and Elwell et al. [134] correspondingly. In little, one

can say that the electrostatic interaction between conduction electron (or hole) and proximate ions may consequence in a displacement of the latter and polarization of the surrounding section, so that the importer is positioned at the center of a polarization potential well. The carrier is stuck at a lattice position, if this potential well is deep sufficient. Its transition to an adjacent site is determined by thermal activation. This has been defined as the hopping mechanism. In such a procedure the motion of the hopping electrons or holes are found to be proportional to e T, where A is the activation energy, k is the Boltzman's constant and T is the temperature in absolute degree. The reasons responsible for resistivity are the chemical in homogeneity affected during preparation, permeability, grain magnitude, sintering situations etc. Ferrites also show uncharacteristically high dielectric constant as well as dispersion of dielectric constant differs in the frequency variety from a few Hz to MHz. A dielectric material when subjected to an interchanging electric field, the positive and negative charges inside the material become displaced with respect to one extra and the system acquires an electric, dipole moment. The dipole moment per unit volume is known as polarization. The diffusion in the dielectric constant has been elucidated by Koops [135].

1.8.2.2. Magnetic properties of ferrites:

Magnetism is a physical property of the magnetic materials which instigates from electron orbital motion or intrinsic spin from the existence of unpaired electrons (Figure 1.20). Iron as well as assured iron containing materials can have unpaired electrons essential to demonstration magnetic behavior. Owing to the more number of electrons in materials, magnetic solids are more without difficulty observed as a gathering of magnetic dipole moments.

If a magnetism shows magnetic material is placed in a magnetic field H, the separable atomic moments in the material give to induce the magnetic flux inside the materials can be written as:

$$B = \mu o\ (H + M) \quad (2)$$

Where μo is the vacuum permeability (12.566×10^{-7} $VsA^{-1}m^{-1}$) and the magnetization M = m /V is the magnetic moment per unit volume, where m is the magnetic moment on a volume V of the material. In the regime, where the magnetization scales linearly with H, it is convenient to define the magnetic susceptibility (χ) as,

$$M = \chi H \quad (3)$$

Fundamentally, there are two types of magnetic measurements for magnetic particles:

1) Magnetization as a function of applied field with temperature (M-H loop).

2) Magnetization as a function of temperature at a given magnetic field.

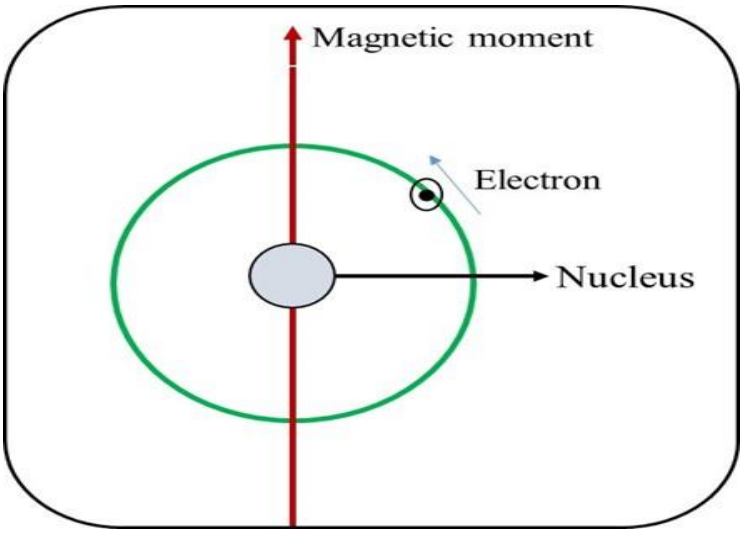

Figure 1.20: Magnetic moment of electron

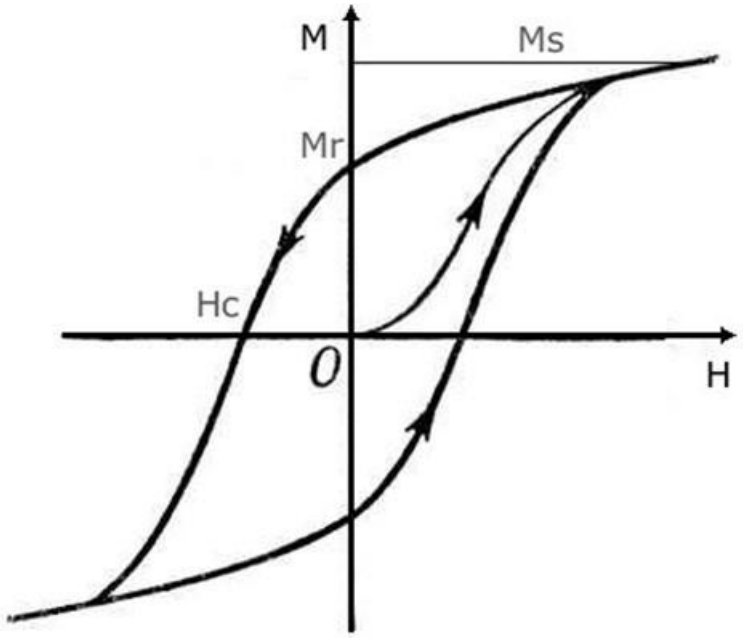

Figure 1.21: Hysteresis curve of a ferromagnetic material at constant temperature[136]

Figure 1.21 displays hysteresis loop of magnetic material at unceasing temperature. Magnetic hysteresis denotes to the irreversibility of the magnetization and demagnetization process. In this Figure Ms = saturated magnetization, Mr = Remanent magnetization, Hc = Coercivity.

1.9. Application of iron oxide nanoparticles:

IONPs are justly an attention-grabbing material have previously found in abundant applications principally owing to large surface to volume ratio and surprising magnetic properties. Sorbent properties are demonstrated by the IONPs, which were excellently tested on separation of organic dyes and toxic inorganic metal noxious waste from industrial discarded water. Moreover, their magnetic properties and capability of the improved surface to selectively bind chemicals show promise of the upcoming industrial attentiveness in magnetically separable sorbents and filtration media. γ-Fe_2O_3 and Fe_3O_4 NPs used in magnetic recording media such as tapes and HDDs. However, present-day industrial demand for advanced recording density have

condensed the size of used NPs., higher susceptibility and low-down coercivity of superparamagnetic iron oxide NPs (SPIONs) and their biocompatibility and biodegradability show excessive potential for relevance in biomedicine. In this thesis, selected of the applications of IONPs have been deliberated briefly which are relevant to our studies.

1.9.1. Heavy metal organic pollutants and dye removal from waste water:

Water resources become critical significant to living things, but there is a terribly environmental anxiety owing to a getting higher contamination from industrial wastewater. Several industries, for specimen pulp, paper, textile, plastics consume chemicals and colorants to process their products and likewise require a large quantity of water. Accordingly, water becomes polluted by heavy metals, organic compounds and extra dangerous materials. The noxious waste make injurious effects the seafaring and terrestrial ecosystems. The separation of contaminations in waste water by adsorption procedure, Magnetic IONPs coated with appropriate surfactants show auspicious help [137]. Magnetic loaded adsorbent materials have gained extraordinary attention in water purification owing to innumerable advantages such as great separation efficiency, modest manipulation method, fast processing speed, economic and environmental friendly, capable to handle concentrated feed, selectivity to specific guest molecules and informal specifically functional amendments.

Copper is universally found in municipal wastewater and its special effects are hazardous to living things. Certain methods have been suitable for its elimination like ion withdrawal, coagulation or adsorption but they possess disadvantage due to small sensitivity and cross reactivity. At present, surface reformed IONPs afford an alternative in bioremediation processes for the exclusion of Cu (II), Cr (VI), Ni etc.,

from water by adsorption [138]. The greatest contaminated industry in the world is textiles industry, since it requires a massive quantity of two most important components, chemicals and water. More than 1000 unlike chemicals have been used in textiles industry, frequently they are colorants and transfer agents. Owing to the economical and efficiency reasons natural and artificial dyes are used in textiles industry.

It generates problems to the atmosphere, because numerous man-made dyes are designed as exceedingly stable molecules, recalcitrant to be degraded by light, chemical and biological management. Specific profitable synthetic dyes generally have unreported great complex structures. Consequently, the release of dye wastewater can be one of industry's most important problem since it comprises numerous noxious waste for instance acid or caustic, liquefied solid, noxious compound similar to heavy metals and colour. Among them, colour is very visible in wastewater; therefore, it can be effortlessly recognized. Furthermore, these coloured sewages will cause main threats to the atmosphere [139].

In presence of minute quantity of artificial dyes is extremely discernible and undesirable. Mostly artificial dyes are also detergent resistant, vastly soluble in water, toxic, non-degradable, recalcitrant/stable and even cancer-causing. Hence, they can be a thoughtful threat to natural ecosystem and human beings. It also can cause the death of marine organisms that are significant for humans and a deficiency of fresh water resources. Therefore, we requirement to treat the wastewaters with noxious dyes previously they are liquidated into the water streams. The IONPs are the excessive boon for effective management of waste water.

1.9.2. Corrosion Inhibition on Mild Steel:

Corrosion is the damaging attack to metal by chemical or electrochemical reaction problem in minor steel, since which is without difficulty corroded in acidic

medium. A corrosion inhibition coating was completed on the slight steel to protect from corrosive atmosphere. Corrosion inhibitor material which precludes the corrosion reaction by given that a shielding barrier film which in turn stopovers the corrosive reaction. Paint material which prevents the uninterrupted contact of rusting media like air and H_2O over the metal surface. It forms a homogeneous skinny layer after exposure to air and preserves the base metal from the corrosion with its surroundings. Numerous metal oxide materials have been used in the formulation of paints. Assorted metal oxides are manufactured from corresponding oxides and are used as colorants in paints which constitute the nanomanufactured paints. Coatings of nanoformulated paint are being carried out on trifling steel plate and the coatings were confirmed in corrosion environment. The extensively used corrosion inhibitors are organic or inorganic chemicals, exclusive and poisonous to environment. For accurate selection of inhibitors, mechanistic information on corrosion and inhibition procedures is required. As an outcome, scientists are scheming novel green inhibitors based on natural products and biodegradable environmental biopolymers. The usual products based on the plant derivation contain more than a limited organic derivatives (e.g. alkaloids, polysaccharides, pigments, organic and amino acids, which can be used as corrosion inhibitors. Certain of polysaccharides, including gums, have been used as corrosion inhibitors for metals in acidic, alkaline, and in salt-water environment [140].

1.9.3. Biomedical application:

(a) Magnetic resonance imaging:

SPION show an imperative role as MRI contrast agents, to improve differentiate fit and pathological tissues. Recent progresses in MR imaging have facilitated in vivo imaging at proximate microscopic resolution [141]. In order to visualize and path stem and progenitor cells by MR imaging, it is compulsory to tag

cells magnetically. Tat protein-derived peptide orders have recently been used as an capable way of internalizing a number of marked proteins into cells [142]. Lewin et al. theorized that biocompatible magnetic particles could be derivatized with analogous sequences and that entire particles could be powerfully ferried into hematopoietic and neural progenitor cells in amounts up to 10-30 pg of superparamagnetic iron per cells [143].

(b) Magnetic hyperthermia:

Magnetic induction hyperthermia, one of the therapies for cancer handling, means the exposition of cancer tissues to an interchanging magnetic field. Magnetic field is not absorbed by the breathing tissues and can be practical to deep area in the living body. As soon as magnetic particles are subjected to a flexible magnetic field, some heat is produced owing to magnetic hysteresis loss. The quantity of heat generated be contingent on the nature of magnetic material and of magnetic field parameters. Magnetic particles inserted all over the place in tumour site and placed inside an oscillating magnetic field will heat up to a temperature reliant on the magnetic properties of the material, the power of the magnetic field, and the frequency of oscillation and the freezing capability of the blood flow in the tumour site. Cancer cells are damaged at temperature greater than 431C, whereas the normal cells can live at higher temperatures. Heat could be created applying an applicable magnetic field. The size of the magnetite crystals is submicrometric, so the powders or bulk of these biomaterials have analogous properties. These materials are not only biocompatible, but also bioactive and could be advantageous for bone tumours [144].

(c) Drug delivery:

Additional possible and best favorable application of these colloidal magnetic NPs is in drug delivery as importers of drug for site-specific delivery of drugs. Perfectly, they could bear on their outward or in their bulk a pharmaceutical drug that could be

driven to the target body part and free there. For these applications, the magnitude, charge and surface chemistry of the MNPs are mainly significant and intensely affect together the blood circulation time plus bioavailability of the particles in the interior the body [145]. In addition, magnetic properties and internalization of particles depend resiliently on the dimension of the magnetic particles [146, 147].

1.10. Review of Literature:

In the ancient time researchers are thinking on morphology and magnitude reliant magnetic properties of IONPs for biomedical uses. As an outcome of the dipolar relations in the middle of the magnetic particles, they are intriguing constructing blocks for self-assembly into innumerable nanostructures. The assembly structures (1-D, 2-D and 3-D nanoparticles) are main for essential studies and for the production of magnetic-force triggered nanodevices. A moment ago, the self-assembly of magnetic nanoparticles into definite shapes were reported by several researchers [148].

The preparation of discrete 1-D nanoparticles magnetic materials, for instance iron oxide nanorods, ellpsiodal and wires over the oriented attachment of monodisperse sphere-shaped nanoparticles has been defined. Cao et al. [149] reported production of uniform α-Fe_2O_3 nanoparticles by surfactant coated hydrothermal method. The manufactured products were α-Fe_2O_3 nanoellipsoids of 115-140 nm in elongated axis and 60-80 nm in small axis.

Mao et al. [150] have produced uniform echoing α-Fe_2O_3 spheres with diameter of approximately 600-700 nm and shell breadth less than 100 nm were achieved by uninterrupted hydrothermally management of watery $FeCl_3$ and tungstophosphoric acid ($H_3PW_{12}O_{40}$) solution at 180 °C. The resonating spheres were collected of robust shells with minor nanoparticles standing out of the surface and show an amazing

surface area and a feeble ferromagnetic behavior was gained at room temperature. The consequence of concentration of $H_3PW_{12}O_{40}$, reaction time and temperature for the making of the hollow spheres were inspected in the sequences of experiments. The surfactant aided hydrothermal method can encourage the self-alignment of the nanocrystals.

In latest time, hierarchical Fe_3O_4 nanostructure with coral-like morphology was produced by a humble glucose-assisted solvothermal method by Qin et al. [151]. The structure contains of tens of branches with lengths almost 1-2 μm. The essence of the nanostructure was collected of unsystematic aggregated particles with dimensions of 10 nm, and the twigs were designed from the oriented-aggregation of nanoparticles. In the case of ferrofluids, the surface properties of the MNPs are the highest factors defining colloidal steadiness. The most important measures used to progress the constancy of ferrofluids are the control of surface charge [152] plus the use of selected surfactants [153-155]. For case, magnetite nanoparticles fabricated through the co-precipitation of Fe^{2+} and Fe^{3+} in ammonia or NaOH solution is typically negatively charged, resultant in agglomeration. To attain stable colloids, the MNPs precipitous can be peptized (to disperse a precipitate to form a colloid by adding of surfactant) with aqueous tetramethylammonium hydroxide or with aqueous perchloric acid. The magnetite nanoparticles can be acidified with a solution of nitric acid and then further oxidized to maghemite by iron nitrate. Afterwards centrifugation and rediffusion in water, a ferrofluid based on positively charged γ-Fe_2O_3 nanoparticles was found, since the surface hydroxy groups are protonated in the acidic medium [156].

Commercially, H_2O or oil based ferrofluids are existing. They are ordinarily steady as soon as the pH value is less than 5 (acidic ferrofluid) or over 8 (alkaline

ferrofluid). In all-purpose, stabilizer's can be chemically joined or physically adsorbed on magnetic nanoparticles to form only 1 or dual layer [157, 158], which generates repulsive (mainly as steric repulsion) forces to equilibrium the magnetic and the Vander Waals attractive forces performing on the nanoparticles. Thus, by steric repulsion, the MNPs are stabilized in suspension.

Polymers inclosing functional groups, for example carboxylic acids, phosphates, and sulfates, can fix to the outer of magnetite. Appropriate polymers for coat consist of PPy, PANI, PACA, PMM, and polyesters, such as PLA, PGA, PCL, and their copolymers [159-161]. Surface-modified MNPs with confident biocompatible polymers are tremendously considered for magnetic-field directed drug targeting, and as contrast agents for MRI [162, 163].

Chu et al. have studied a production of polymer layered MNPs by a particular inverse microemulsion [164]. The magnetite particles were first manufactured in an inverse microemulsion, containing of water/sodium bis(2-ethylhexylsulfosuccinate)/ toluene. Subsequently, water, monomers (methacrylic acid and hydroxyethyl methacrylate), cross-linked (N,Nmethylenebis(acrylamide) and an initiator (2,2'-azobis (isobutyronitrile) were adding in reaction assortment under nitrogen, and the polymerization reaction was carried out at 558 °C. Subsequently polymerization, the particles were getting back by precipitation in a superfluous of an acetone/methanol mixture (9:1 ratio). The polymer-coated nanoparticles have superparamagnetic properties then a thin size spreading at a size of almost 80 nm. However, the long-standing constancy of these polymer-coated nanoparticles was not spoken. Polyaniline can also be used for the coating of Fe_3O_4 by oxidative polymerization in the existence of ammonium peroxodisulfate catalyst [165].

Water soluble magnetic Fe_3O_4 NPs were prepared by merging the *in situ* synthesis and putrefaction of a magnetic polymer hydrogel. Fe_3O_4 NPs with an ordinary diameter of 6.3-8.3 nm were manufactured in a cross-linked polyacrylamide hydrogel by co-precipitating iron ions. The putrefaction of the magnetic polymer hydrogel by a solution of NaOH led the transferal of Fe_3O_4NPs into the aqueous medium. The saturation magnetization of Fe_3O_4NPs were 44.6 and 54.7 emu g^{-1} at 300 K and 5 K, correspondingly [166].

Bora et al. [167] studied covalently attachment of BSA molecules with stearic acid coated IONPs. Magnetic property by was reserved even afterward bonding of BSA on Fe_3O_4 nanoparticles. Folic acid (FA)-functionalized Fe_3O_4 nanoparticles were created from iron (III) 3-allylacetylacetonate (IAA) through in situ hydrolysis and ligand adjustment. The γ-carboxylic acid of FA was effectively bonded with ligand of the Fe_3O_4NPs devoid of the destruction of the α-carboxylic acid collection of folic acid, which has a fellow feeling for folate receptors articulated on tumor cells. The magnitude of the folic acid conjugated Fe_3O_4 nanoparticles is 8 nm, revealed superparamagnetic behavior and a comparatively great magnetization at RT. The SAR of the FA-Fe_3O_4 nanoparticles was 670 W g^{-1} in a 230 kHz alternating magnetic field and 100 Oe. The chemo choosy outward modification of magnetite particles using FA produced an original cancer-targeting system for usage in hyperthermia handling [168].

Abbas et al. described the formation of superparamagnetic Alg-Fe_3O_4 as a unique magnetic adsorbent by using chemical in situ co-precipitation procedure. Alginate coated Fe_3O_4NPs is used for the separation of malachite green (MG) by using batch adsorption process. Effects of various adsorption factors like pH, temperature, adsorbent dosed were examined on adsorption properties of MG onto

Alg-Fe_3O_4 nanoparticles. The greatest adsorption capability achieved from Langmuir isotherm equation was 47.84 mg/g. The fallouts revealed that the adsorption of MG on nanoparticles followed pseudo-second-order kinetic model [169].

Magnetic MFe_3O_4/CS NPs were fruitfully synthesized via simple reduction-precipitation method. The adsorption performances of MFe_3O_4/CS NPs to responsive brilliant red X-3B were examined, together with various adsorption parameters and adsorption kinetics. It was found that the adsorption performances of X-3B on MFe_3O_4/CS NPs were powerfully reliant on both early pH and the adsorbent dosage. The adsorption equilibrium row data fitted fine with the Langmuir isotherm model and the adsorption procedure followed the pseudo-second-order kinetic model. Thermodynamic parameters for instance ΔG^o, ΔH^o, and ΔS^o point out that the adsorption was spontaneous and endothermic [170].

Fe nanoparticles were synthesized using green approaches based on tea extract, containing green, oolong and black teas. The unsurpassed technique for degrading MG was Fe NPs fabricated by green tea excerpts because it consist an higher quantity of caffeine/polyphenols which perform as both reducing as well as capping agents in the manufacture of Fe NPs. Moreover, kinetics for the degradation of MG using these Fe nanoparticles follow pseudo first-order reaction kinetics model with higher than 20 kJ/mol activation energy, proposing a chemically diffusion-controlled reaction [171].

IONPs were prepared via facile additive-free synthetic approach for separation of CR dye and heavy metal Cr (VI) from water. These NPs were used to examine auspicious applications in water management. Owing to its lesser size and great surface area, the greater adsorption aptitudes of CR dye and Cr (VI) have been

defined using the Langmuir equation and found to reach up to 253.8 and 17.0 mg g^{-1}, correspondingly [172].

The fabrication of Fe based metal-organic frameworks loaded onto IONPs were formed using chemical method and the exploration of its capacity for the exclusion of MR has been studied [173]. Effective parameters in the choice of a novel adsorbent, i.e. adsorption capability, thermodynamics, and kinetics were inspected. The capability of the manufactured adsorbent in the separation of MR was compared with the metal organic structure (MIL-100(Fe) and IONPs. The outcomes indication that Fe_3O_4@MIL-100(Fe) nanocomposite reveals a greater adsorption capacity.

A unique bimetallic Fe-Zn NPs was fabricated using simple co-precipitation technique and practical for the adsorptive elimination of cancer-causing dye MG and CR present in water. Adsorption experiments were conducted to examine the adsorption method by changing the optimization factors such as pH of solution, time, and preliminary dye concentration. The adsorption procedure was firstly very quick, and the largest adsorption was observed in a period 60 min of contact time [174].

MNPs has been used for elimination of dyes from artificial and actual textile discarded water applying adsorption technique with the distinctive effects of various experimental factors for example, contact time, pH, and coexisting ions were investigated. Computational modeling of the relations of unlike dye molecules with changed surfaces of γ-Fe_2O_3NPs has been performed to obtain greater mechanistic insights on the adsorption behavior [175].

A. Debnath at el. reported that the elimination of anionic organic dye (Congo red) by chemically synthesized Fe_2O_3 nanoparticle adsorbent material from aqueous solution under variables prompting the adsorption ability, like as pH of solution,

adsorbent dosage, temperature, adsorption time and primary concentration, were consistently examined [176].

The synthesis of porous magnetic microspheres nanomaterial by using one step friedel-craft alkylation reaction and this material is used for speedy expulsion of dyes from aqueous solution [177].

For the exclusion of responsive Blue 19 from colored discarded water Fe_3O_4MNPs modified with L-arginine (Fe_3O_4@L-arginine) has been used. In order to observe the impact of self-governing variables on dye elimination and determining the optimum situation, the Box-Behnken Design (BBD) lower than RSM was employed [178].

The γ-Fe_2O_3-NPs-AC was prepared and used as inventive adsorbent for the ultrasonic-assisted exclusion of MB and MG. Response surface methodology and synthetic neural network were practical model and optimize the adsorption of the MB and MG in their separate and double solutions followed by the examination on adsorption isotherm and kinetics [179].

Fe_3O_4 MNPs were fabricated via chemical precipitation technique for successful elimination of methyl violet as a cationic dye from aqueous solutions was examined. To take out methyl violet, the external layer of the MNPs was improved with SDS as an anionic surfactant. Also, the numerous parameters affecting colorant removal were inspected and optimized [180].

The production of superparamagnetic γ-Fe_2O_3 nanoparticles of well-ordered morphology were prepared by flame spray pyrolysis technique. The use of maghemite nanoparticles for the separation of copper (Cu^{2+}), lead (Pb^{2+}) ion from discarded water and metal ion uptake was principally observed by electrostatic attraction mechanism [181].

The materialization of the maximum magnetic Fe_xO_y, Fe_3O_4, on biochar using oxidative hydrolysis of $FeCl_2$ under basic media was executed to synthesize best adsorbent magnetic pine sawdust biochar: MPSB. Sorbent steadiness, parametric, kinetics, isotherm, thermodynamic and sorbent renaissance studies were executed to comprehend the potential of MPSB as adsorbent to eliminate an emerging waste product, sulfamethoxazole (SMX) from aqueous solution [182].

A plausible and sparingly viable co-precipitation manner has been the center of consideration in modern years to synthesize $ZnFe_2O_4$ nanoparticles. The manufactured samples are analyzed by PXRD which verified the prevalence of sharp diffraction peaks, ascribed to its momentous crystalline nature and crystallite size has been predictable to be 11.04 nm. $ZnFe_2O_4$ nanoparticles shows conductivity [183].

Fe_3O_4@HA@Ag MNCs were effectively fabricated by the unpretentious reflux process for the separation of azo dyes from the industrial aqueous media. Fe_3O_4@HA@AgMNCs showed extraordinary catalytic activity to degrade MB in a period of 20 min from the unwanted water. Therefore this newly synthesized Fe_3O_4@HA@Ag MNCs can be an encouraging nanocatalyst for the decrease of industrial unwanted azo dyes like methylene blue throughout the wastewater handling [184].

The manufactured magnetic AC (Fe-AC) was used excellently for the removal of Methylene Blue (MB) dye from aqueous solution. The special impacts of dissimilar batch factors such as adsorbent dosage (0.05-0.2 g/100 mL), early pH (3-9), temperature (298-318 K), early dyestuff concentration (50-250 mg/L) and contact time (5-60 min) on the adsorption procedure was examined. The created AC and Fe-AC adsorbents as unique adsorbents suggestion a great possibilities for the separation of MB dyestuff from aqueous solutions because of the benefit of their producibility

from an inexpensive source, extraordinary adsorption capability and speedy uptake feasibility [185].

For the examination of noxious waste removal and oil water separation effectiveness the magnetic Fe_3O_4 nanoparticle (MNP)-coated fluorinated carbon fabric (CF) membrane has been prepared and methylene blue (MB) and Cu^{2+} ion have been used as adsorbate for estimating the removal performance of the CF membrane. The MNP-coated CF membrane reveals greater adsorption capacity toward cationic MB molecules and Cu^{2+} ions in liquefied phase, ascribed to a synergistic effect that combined with spongy CFs and Fe_3O_4 magnetite [186].

1.11. Objectives of thesis:

Keeping extensive existence, non-toxicity, easily synthesizability of various forms of iron oxides, the author enthusiastic to carry out the further work on of iron oxides in nanostructured form, and to explore the properties for plausible applications, particularly for removal of toxic organic dyes from waste water. The objective of the present work includes:

a) Synthesis of iron oxides nanoparticles in solution phase by chemical co-precipitation method.
b) Characterization of materials by various techniques such as XRD, SEM, FTIR, EDX, BET, UV-Vis, and PL for structural, morphological, functional group identification as well as optical properties determination.
c) Applications of iron oxides nanoparticles as photocatalysts for mineralization of toxic organic dyes.
d) Applications of iron oxides nanoparticles as adsorbent for removal of toxic organic dyes from waste water.

1.12. References:

[1] Taniguchi N. On the basic concept of nano-technology. Proc Intl Conf Prod London, 1974: British Society of Precision Engineering; 1974.

[2] Feynman RP. There's plenty of room at the bottom. Engineering and science. 1960;23:22-36.

[3] Roco MC. National nanotechnology initiative-past, present, future. Handbook on nanoscience, engineering and technology Ed Goddard, WA et al CRC, Taylor and Francis, Boca Raton and London-2007-P. 2007:3.1-3.26.

[4] Drexler KE, Peterson C, Pergamit G. Unbounding the future. William Morrow, New York. 1991:294.

[5] Murray CB, Kagan C, Bawendi M. Synthesis and characterization of monodisperse nanocrystals and close-packed nanocrystal assemblies. Annual Review of Materials Science. 2000;30:545-610.

[6] Fang M, Zeisberg W-M, Condon C, Ogryzko V, Danchin A, Mechold U. Degradation of nanoRNA is performed by multiple redundant RNases in Bacillus subtilis. Nucleic acids research. 2009;37:5114-25.

[7] Kim YT, Han JH, Hong BH, Kwon YU. Electrochemical Synthesis of CdSe Quantum-Dot Arrays on a Graphene Basal Plane Using Mesoporous Silica Thin-Film Templates. Advanced Materials. 2010;22:515-8.

[8] Zhang G, Wang D. Fabrication of heterogeneous binary arrays of nanoparticles via colloidal lithography. Journal of the American Chemical Society. 2008;130:5616-7.

[9] Wang J, Lin M, Yan Y, Wang Z, Ho PC, Loh KP. CdSe/AsS Core-Shell Quantum Dots: Preparation and Two-Photon Fluorescence. Journal of the American Chemical Society. 2009;131:11300-1.

[10] Gautam UK, Vivekchand S, Govindaraj A, Rao C. GaS and GaSe nanowalls and their transformation to Ga_2O_3 and GaN nanowalls. Chemical Communications. 2005:3995-7.

[11] Lee JY, Hong BH, Kim WY, Min SK, Kim Y, Jouravlev MV, et al. Near-field focusing and magnification through self-assembled nanoscale spherical lenses. Nature. 2009;460:498-501.

[12] Stouwdam JW, Janssen RA. Red, green, and blue quantum dot LEDs with solution processable ZnO nanocrystal electron injection layers. Journal of Materials Chemistry. 2008;18:1889-94.

[13] Lee W, Kang SH, Kim J-Y, Kolekar GB, Sung Y-E, Han S-H. TiO_2 nanotubes with a ZnO thin energy barrier for improved current efficiency of CdSe quantum-dot-sensitized solar cells. Nanotechnology. 2009;20:335706.

[14] Mokerov V, Fedorov YV, Velikovski L, Scherbakova MY. New quantum dot transistor. Nanotechnology. 2001;12:552.

[15] Ustinov V, Zhukov A, Kovsh A, Mikhrin S, Maleev N, Volovik B, et al. Long-wavelength quantum dot lasers on GaAs substrates. Nanotechnology. 2000;11:397.

[16] Tiwari JN, Tiwari RN, Kim KS. Zero-dimensional, one-dimensional, two-dimensional and three-dimensional nanostructured materials for advanced electrochemical energy devices. Progress in Materials Science. 2012;57:724-803.

[17] Iijima S. Helical microtubules of graphitic carbon. nature. 1991;354:56.

[18] Kuchibhatla SV, Karakoti A, Bera D, Seal S. One dimensional nanostructured materials. Progress in materials science. 2007;52:699-913.

[19] Huang L, Wang H, Wang Z, Mitra A, Zhao D, Yan Y. Cuprite nanowires by electrodeposition from lyotropic reverse hexagonal liquid crystalline phase. Chemistry of materials. 2002;14:876-80.

[20] Okada T, Kawashima K, Nakata Y, Ning X. Synthesis of ZnO nanorods by laser ablation of ZnO and Zn targets in He and O_2 background gas. Japanese journal of applied physics. 2005;44:688.

[21] Xia H, Feng J, Wang H, Lai MO, Lu L. MnO_2 nanotube and nanowire arrays by electrochemical deposition for supercapacitors. Journal of Power Sources. 2010;195:4410-3.

[22] Li GR, Feng ZP, Zhong JH, Wang ZL, Tong YX. Electrochemical synthesis of polyaniline nanobelts with predominant electrochemical performances. Macromolecules. 2010;43:2178-83.

[23] Park JM, Nalwa KS, Leung W, Constant K, Chaudhary S, Ho K-M. Fabrication of metallic nanowires and nanoribbons using laser interference lithography and shadow lithography. Nanotechnology. 2010;21:215301.

[24] Cao L, Tian H, Zhang Z, Zhang X, Gao C, Wang W. Nucleation and growth of feather-like boron nanowire nanojunctions. Nanotechnology. 2003;15:139.

[25] Yoon SM, Hwang IC, Kim KS, Choi HC. Synthesis of Single-Crystal Tetra (4-pyridyl) porphyrin Rectangular Nanotubes in the Vapor Phase. Angewandte Chemie International Edition. 2009;48:2506-9.

[26] Wang Y, Kim J-S, Lee JY, Kim GH, Kim KS. Diameter-and length-dependent volume plasmon excitation of bismuth nanorods investigated by electron energy loss spectroscopy. Chemistry of materials. 2007;19:3912-6.

[27] Wang YW, Hong BH, Lee JY, Kim JS, Kim GH, Kim KS. Antimony nanowires self-assembled from Sb nanoparticles. The Journal of Physical Chemistry B. 2004;108:16723-6.

[28] Hong BH, Lee JY, Lee CW, Kim JC, Bae SC, Kim KS. Self-assembled arrays of organic nanotubes with infinitely long one-dimensional H-bond chains. Journal of the American Chemical Society. 2001;123:10748-9.

[29] Hong BH, Small JP, Purewal MS, Mullokandov A, Sfeir MY, Wang F, et al. Extracting subnanometer single shells from ultralong multiwalled carbon nanotubes. Proceedings of the National Academy of Sciences of the United States of America. 2005;102:14155-8.

[30] Hong BH, Lee JY, Beetz T, Zhu Y, Kim P, Kim KS. Quasi-continuous growth of ultralong carbon nanotube arrays. Journal of the American Chemical Society. 2005;127:15336-7.

[31] Hwang IC, Heo SW, Singh NJ, Lee JW, Chun Y, Baek SB, et al. Self-Assembled Thermally Highly Stable 1-Dimensional Proton Arrays. The Journal of Physical Chemistry B. 2010;114:7216-21.

[32] Kim KS, Suh SB, Kim JC, Hong BH, Lee EC, Yun S, et al. Assembling Phenomena of Calix [4] hydroquinone Nanotube Bundles by One-Dimensional Short Hydrogen Bonding and Displaced π-π Stacking. Journal of the American Chemical Society. 2002;124:14268-79.

[33] Kim WY, Choi YC, Kim KS. Understanding structures and electronic/spintronic properties of single molecules, nanowires, nanotubes, and nanoribbons towards the design of nanodevices. Journal of Materials Chemistry. 2008;18:4510-21.

[34] Jun Y-w, Seo J-w, Oh SJ, Cheon J. Recent advances in the shape control of inorganic nano-building blocks. Coordination chemistry reviews. 2005;249:1766-75.

[35] Kim KS, Zhao Y, Jang H, Lee SY, Kim JM, Kim KS, et al. Large-scale pattern growth of graphene films for stretchable transparent electrodes. nature. 2009;457:706-10.

[36] Bae S, Kim H, Lee Y, Xu X, Park J, Zheng Y, et al. Nature Nanotechnol. 5, 574 (2010). CrossRef| CAS/Web of Science® Times Cited. 1763;1215.

[37] Pradhan D, Leung K. Vertical growth of two-dimensional zinc oxide nanostructures on ITO-coated glass: effects of deposition temperature and deposition time. The Journal of Physical Chemistry C. 2008;112:1357-64.

[38] Tiwari JN, Pan FM, Tiwari RN, Nandi S. Facile synthesis of continuous Pt island networks and their electrochemical properties for methanol electrooxidation. Chemical Communications. 2008:6516-8.

[39] Nayak BB, Behera D, Mishra BK. Synthesis of Silicon Carbide Dendrite by the Arc Plasma Process and Observation of Nanorod Bundles in the Dendrite Arm. Journal of the American Ceramic Society. 2010;93:3080-3.

[40] Dong X, Ji X, Jing J, Li M, Li J, Yang W. Synthesis of triangular silver nanoprisms by stepwise reduction of sodium borohydride and trisodium citrate. The Journal of Physical Chemistry C. 2010;114:2070-4.

[41] Mann AK, Skrabalak SE. Synthesis of single-crystalline nanoplates by spray pyrolysis: A metathesis route to Bi_2WO_6. Chem Mater. 2011;23:1017-22.

[42] Siril PF, Ramos L, Beaunier P, Archirel P, Etcheberry A, Remita H. Synthesis of ultrathin hexagonal palladium nanosheets. Chemistry of Materials. 2009;21:5170-5.

[43] Vizireanu S, Stoica S, Luculescu C, Nistor L, Mitu B, Dinescu G. Plasma techniques for nanostructured carbon materials synthesis. A case study: carbon nanowall growth by low pressure expanding RF plasma. Plasma Sources Science and Technology. 2010;19:034016.

[44] Jung SH, Oh E, Lee KH, Yang Y, Park CG, Park W, et al. Sonochemical preparation of shape-selective ZnO nanostructures. Crystal growth and design. 2007;8:265-9.

[45] Ren X, Zelenay P, Thomas S, Davey J, Gottesfeld S. Recent advances in direct methanol fuel cells at Los Alamos National Laboratory. Journal of Power Sources. 2000;86:111-6.

[46] Oliveira ECd, Pires CT, Pastore HO. Why are carbon molecular sieves interesting? Journal of the brazilian Chemical Society. 2006;17:16-29.

[47] Hu L, Choi JW, Yang Y, Jeong S, La Mantia F, Cui LF, et al. Highly conductive paper for energy-storage devices. Proceedings of the National Academy of Sciences. 2009;106:21490-4.

[48] Kamarudin SK, Achmad F, Daud WRW. Overview on the application of direct methanol fuel cell (DMFC) for portable electronic devices. International Journal of hydrogen energy. 2009;34:6902-16.

[49] Chen H, Cong TN, Yang W, Tan C, Li Y, Ding Y. Progress in electrical energy storage system: A critical review. Progress in Natural Science. 2009;19:291-312.

[50] Aricò AS, Bruce P, Scrosati B, Tarascon J-M, Van Schalkwijk W. Nanostructured materials for advanced energy conversion and storage devices. Nature materials. 2005;4:366-77.

[51] Ferreira-Aparicio P, Folgado M, Daza L. High surface area graphite as alternative support for proton exchange membrane fuel cell catalysts. Journal of Power Sources. 2009;192:57-62.

[52] Li HQ, Wang YG, Wang CX, Xia YY. A competitive candidate material for aqueous supercapacitors: High surface-area graphite. Journal of Power Sources. 2008;185:1557-62.

[53] Jin YH, Lee SH, Shim HW, Ko KH, Kim DW. Tailoring high-surface-area nanocrystalline TiO_2 polymorphs for high-power Li ion battery electrodes. Electrochimica Acta. 2010;55:7315-21.

[54] Dong Z, Kennedy SJ, Wu Y. Electrospinning materials for energy-related applications and devices. Journal of Power Sources. 2011;196:4886-904.

[55] Mastragostino M, Soavi F. Strategies for high-performance supercapacitors for HEV. Journal of Power Sources. 2007;174:89-93.

[56] Winter M, Brodd RJ. What are batteries, fuel cells, and supercapacitors? : ACS Publications; 2004.

[57] Armand M, Tarascon J-M. Building better batteries. Nature. 2008;451:652-7.

[58] Simon P, Gogotsi Y. Materials for electrochemical capacitors. Nature materials. 2008;7:845-54.

[59] Hu CC, Chang KH, Lin MC, Wu YT. Design and tailoring of the nanotubular arrayed architecture of hydrous RuO_2 for next generation supercapacitors. Nano letters. 2006;6:2690-5.

[60] Shen Q, Jiang L, Zhang H, Min Q, Hou W, Zhu JJ. Three-dimensional dendritic Pt nanostructures: sonoelectrochemical synthesis and electrochemical applications. The Journal of Physical Chemistry C. 2008;112:16385-92.

[61] Teng X, Liang X, Maksimuk S, Yang H. Synthesis of porous platinum nanoparticles. Small. 2006;2:249-53.

[62] Lee H, Habas SE, Kweskin S, Butcher D, Somorjai GA, Yang P. Morphological control of catalytically active platinum nanocrystals. Angewandte Chemie. 2006;118:7988-92.

[63] Wang L, Yamauchi Y. Facile synthesis of three-dimensional dendritic platinum nanoelectrocatalyst. Chemistry of Materials. 2009;21:3562-9.

[64] Wang JN, Su LF, Wu ZP. Growth of highly compressed and regular coiled carbon nanotubes by a spray-pyrolysis method. Crystal Growth and Design. 2008;8:1741-7.

[65] Liu J, Essner J, Li J. Hybrid supercapacitor based on coaxially coated manganese oxide on vertically aligned carbon nanofiber arrays. Chemistry of Materials. 2010;22:5022-30.

[66] Lei W, Liu D, Zhang J, Zhu P, Cui Q, Zou G. Direct synthesis, growth mechanism, and optical properties of 3-D AlN nanostructures with urchin shapes. Crystal Growth and Design. 2009;9:1489-93.

[67] Hwang IC, Kumar R, Kim ND, Chun Y, Lee JW, Kumar P, et al. Controlling metal nanotoppings on the tip of silicide nanostructures. Nanotechnology. 2009;20:245605.

[68] Lyon D, Hubler A. Gap size dependence of the dielectric strength in nano vacuum gaps. IEEE Transactions on Dielectrics and Electrical Insulation. 2013;20:1467-71.

[69] Murphy CJ. Nanocubes and nanoboxes. Science. 2002;298:2139-41.

[70] Nalwa HS. Handbook of nanostructured materials and nanotechnology, five-volume set: Academic Press; 1999.

[71] Montavon G, Sampath S, Berndt C, Herman H, Coddet C. Effects of the spray angle on splat morphology during thermal spraying. Surface and Coatings Technology. 1997;91:107-15.

[72] Senthilnathan V, Ganesan S. Novel spray pyrolysis for dye-sensitized solar cell. Journal of Renewable and Sustainable Energy. 2010;2:063102.

[73] Perednis D, Wilhelm O, Pratsinis S, Gauckler L. Morphology and deposition of thin yttria-stabilized zirconia films using spray pyrolysis. Thin solid films. 2005;474:84-95.

[74] Gleiter H. Nanocrystalline materials. Advanced Structural and Functional Materials: Springer; 1991. p. 1-37.

[75] Siegel RW. Cluster-assembled nanophase materials. Annual Review of Materials Science. 1991;21:559-78.

[76] Reiss G, Hütten A. Magnetic nanoparticles: applications beyond data storage. Nature materials. 2005;4:725-6.

[77] Iida H, Takayanagi K, Nakanishi T, Osaka T. Synthesis of Fe_3O_4 nanoparticles with various sizes and magnetic properties by controlled hydrolysis. Journal of colloid and interface science. 2007;314:274-80.

[78] Derakhshi P, Khorrami S, Lotfi R. An Investigation on synthesis and morphology of nickel doped cobalt ferrite in the presence of surfactant in different calcination temperature by coprecipitation route. World Appl Scie J. 2012;16:156-9.

[79] Kung HH, Ko EI. Preparation of oxide catalysts and catalyst supports-a review of recent advances. The Chemical Engineering Journal and the Biochemical Engineering Journal. 1996;64:203-14.

[80] Kyprianidou-Leodidou T, Caseri W, Suter UW. Size variation of PbS particles in high-refractive-index nanocomposites. The Journal of Physical Chemistry. 1994;98:8992-7.

[81] Wang CC, Zhang Z, Ying JY. Photocatalytic decomposition of halogenated organics over nanocrystalline titania. Nanostructured Materials. 1997;9:583-6.

[82] Gacoin T, Malier L, Boilot J-P. New Transparent Chalcogenide Materials Using a Sol-Gel Process. Chemistry of materials. 1997;9:1502-4.

[83] Sankaran V, Yue J, Cohen R, Schrock R, Silbey R. Synthesis of zinc sulfide clusters and zinc particles within microphase-separated domains of organometallic block copolymers. Chemistry of materials. 1993;5:1133-42.

[84] Yuan Y, Fendler JH, Cabasso I. Photoelectron transfer mediated by size-quantized cadmium sulfide particles in polymer-blend membranes. Chemistry of materials. 1992;4:312-8.

[85] Majetich S, Carter A. Surface effects on the optical properties of cadmium selenide quantum dots. The Journal of Physical Chemistry. 1993;97:8727-31.

[86] Justus B, Tonucci R, Berry A. Nonlinear optical properties of quantum-confined GaAs nanocrystals in Vycor glass. Applied physics letters. 1992;61:3151-3.

[87] Schmidt H. Chemistry of material preparation by the sol-gel process. Journal of Non-Crystalline Solids. 1988;100:51-64.

[88] LaConte L, Nitin N, Bao G. Magnetic nanoparticle probes. Materials Today. 2005;8:32-8.

[89] Patel D, Moon JY, Chang Y, Kim TJ, Lee GH. Poly (D, L-lactide-co-glycolide) coated superparamagnetic iron oxide nanoparticles: Synthesis, characterization and in vivo study as MRI contrast agent. Colloids and Surfaces A: Physicochemical and Engineering Aspects. 2008;313:91-4.

[90] Zhao M, Josephson L, Tang Y, Weissleder R. Magnetic sensors for protease assays. Angewandte Chemie International Edition. 2003;42:1375-8.

[91] Mornet S, Vasseur S, Grasset F, Veverka P, Goglio G, Demourgues A, et al. Magnetic nanoparticle design for medical applications. Progress in Solid State Chemistry. 2006;34:237-47.

[92] Stevens PD, Fan J, Gardimalla HM, Yen M, Gao Y. Superparamagnetic nanoparticle-supported catalysis of Suzuki cross-coupling reactions. Organic letters. 2005;7:2085-8.

[93] Jun YW, Choi JS, Cheon J. Heterostructured magnetic nanoparticles: their versatility and high performance capabilities. Chemical Communications. 2007:1203-14.

[94] Gupta AK, Gupta M. Synthesis and surface engineering of iron oxide nanoparticles for biomedical applications. Biomaterials. 2005;26:3995-4021.

[95] Rebolledo AF, Bomatí-Miguel O, Marco JF, Tartaj P. A facile synthetic route for the preparation of superparamagnetic iron oxide nanorods and nanorices with tunable surface functionality. Advanced Materials. 2008;20:1760-5.

[96] Islam MS, Kusumoto Y, Kurawaki J, Abdulla-Al-Mamun M, Manaka H. A comparative study on heat dissipation, morphological and magnetic properties of hyperthermia suitable nanoparticles prepared by co-precipitation and hydrothermal methods. Bulletin of Materials Science. 2012;35:1047-53.

[97] Cornell R, Schwertmann U. Structure, properties, reactions, occurrence and uses. The iron oxides VCH, Weinheim. 1996:375-95.

[98] Cornell RM, Schwertmann U. The iron oxides: structure, properties, reactions, occurrences and uses: John Wiley & Sons; 2003.

[99] Amelia R, Wu WD, Chen XD, Selomulya C. Assembly of magnetic microcomposites from low pH precursors using a novel micro-fluidic-jet-spray-dryer. Chemical Engineering Research and Design. 2012;90:150-7.

[100] Weiss W, Ranke W. Surface chemistry and catalysis on well-defined epitaxial iron-oxide layers. Progress in Surface Science. 2002;70:1-151.

[101] Giles DE, Mohapatra M, Issa TB, Anand S, Singh P. Iron and aluminium based adsorption strategies for removing arsenic from water. Journal of Environmental Management. 2011;92:3011-22.

[102] Shwertmann U, Cornell R. The Iron Oxides-Structure, Properties, Reactions, Occurrence and Uses. VCH, New York. 1996.

[103] Guo H, Barnard AS. Naturally occurring iron oxide nanoparticles: morphology, surface chemistry and environmental stability. Journal of Materials Chemistry A. 2013;1:27-42.

[104] Bhukal S, Namgyal T, Mor S, Bansal S, Singhal S. Structural, electrical, optical and magnetic properties of chromium substituted Co-Zn nanoferrites $Co_{0.6}Zn_{0.4}Cr_xFe_{2-x}O_4(0\leqslant x\leqslant 1.0)$ prepared via sol-gel auto-combustion method. Journal of Molecular Structure. 2012;1012:162-7.

[105] Sharifi I, Shokrollahi H. Nanostructural, magnetic and Mössbauer studies of nanosized $Co_{1-x}Zn_xFe_2O_4$ synthesized by co-precipitation. Journal of Magnetism and Magnetic Materials. 2012;324:2397-403.

[106] Hilpert S, Wille A. Zusammenhänge zwischen Ferromagnetismus und Aufbau der Ferrite. Zeitschrift für Physikalische Chemie. 1932;18:291-315.

[107] London C. Hall, 1954. Russ ed: Hirshfelder JO, Curtiss Ch F, Bird RB Molekulyarnaya teoriya gazov i zhidkostei Moscow, Izd-vo inostrannoi literatury Publ. 1961.

[108] Hill RJ, Craig JR, Gibbs G. Systematics of the spinel structure type. Physics and chemistry of minerals. 1979;4:317-39.

[109] Marshall L, Dollase W. Cation arrangement in Fe-Zn-Cr spinel oxides. Am Mineral. 1984;69:928-36.

[110] Šepelák V, Rogachev AY, Steinike U, Uecker DC, Krumeich F, Wissmann S, et al. The synthesis and structure of nanocrystalline spinel ferrite produced by high-energy ball-milling method. Materials Science Forum: Trans Tech Publ; 1997. p. 139-44.

[111] Yin Y, Alivisatos AP. Colloidal nanocrystal synthesis and the organic-inorganic interface. Nature. 2004;437:664.

[112] Shobana M, Kwon H, Choe H. Structural studies on the yttrium-doped cobalt ferrite powders synthesized by sol-gel combustion method. Journal of Magnetism and Magnetic Materials. 2012;324:2245-8.

[113] Deraz N, Alarifi A. Structural, morphological and magnetic properties of nano-crystalline zinc substituted cobalt ferrite system. Journal of analytical and applied pyrolysis. 2012;94:41-7.

[114] Iqbal MJ, Ahmad Z, Melikhov Y, Nlebedim IC. Effect of Cu-Cr co-substitution on magnetic properties of nanocrystalline magnesium ferrite. Journal of Magnetism and Magnetic Materials. 2012;324:1088-94.

[115] Zhao L, Yang H, Yu L, Cui Y, Zhao X, Zou B, et al. Structure and magnetic properties of nanocrystalline $CoLa_{0.08}Fe_{1.92}O_4$ ferrite. Journal of magnetism and magnetic materials. 2006;301:445-51.

[116] Maisnam M, Phanjoubam S. Frequency dependence of electrical and magnetic properties of Li-Ni-Mn-Co ferrites. Solid State Communications. 2012;152:320-3.

[117] Deraz N. Glycine-assisted fabrication of nanocrystalline cobalt ferrite system. Journal of Analytical and Applied Pyrolysis. 2010;88:103-9.

[118] Deraz N. Size and crystallinity-dependent magnetic properties of copper ferrite nano-particles. Journal of Alloys and Compounds. 2010;501:317-25.

[119] Cojocariu AM, Soroceanu M, Hrib L, Nica V, Caltun OF. Microstructure and magnetic properties of substituted (Cr, Mn)-cobalt ferrite nanoparticles. Materials Chemistry and Physics. 2012;135:728-32.

[120] Goh S, Chia CH, Zakaria S, Yusoff M, Haw C, Ahmadi S, et al. Hydrothermal preparation of high saturation magnetization and coercivity cobalt ferrite nanocrystals without subsequent calcination. Materials Chemistry and Physics. 2010;120:31-5.

[121] Mathew DS, Juang RS. An overview of the structure and magnetism of spinel ferrite nanoparticles and their synthesis in microemulsions. Chemical Engineering Journal. 2007;129:51-65.

[122] Jung DS, Kang YC. Effects of precursor types of Fe and Ni components on the properties of $NiFe_2O_4$ powders prepared by spray pyrolysis. Journal of magnetism and magnetic materials. 2009;321:619-23.

[123] Verma S, Chand J, Singh M. Effect of In^{3+} ions doping on the structural and magnetic properties of $Mg_{0.2}Mn_{0.5}Ni_{0.3}In_xFe_{2-x}O_4$ spinel ferrites. Journal of Magnetism and Magnetic Materials. 2012;324:3252-60.

[124] Azam A. Microwave assisted synthesis and characterization of Co doped Cu ferrite nanoparticles. Journal of Alloys and Compounds. 2012;540:145-53.

[125] Goldman A. Modern ferrite technology: Springer Science & Business Media; 2006.

[126] Standley KJ. Oxide magnetic materials: Oxford University Press; 1972.

[127] Spaldin N. Magnetic materials. Fundamentals and Device Application, Cambridge. 2003:27-31.

[128] Park J, Hong YK, Kim SG, Kim S, Liyanage LS, Lee J, et al. Maximum energy product at elevated temperatures for hexagonal strontium ferrite ($SrFe_{12}O_{19}$) magnet. Journal of Magnetism and Magnetic Materials. 2014;355:1-6.

[129] Lagutin A, Fedorov G, Vanacken J, Herlach F. Magnetic properties of dysprosium-ittrium ferrite-garnets in pulsed magnetic fields at low temperatures. Journal of magnetism and magnetic materials. 1999;195:97-106.

[130] Bragg W. The structure of magnetite and the spinels. Nature. 1915;95:561.

[131] Bragg WH. XXX. The structure of the spinel group of crystals. The London, Edinburgh, and Dublin Philosophical Magazine and Journal of Science. 1915;30:305-15.

[132] Issa B, Obaidat IM, Albiss BA, Haik Y. Magnetic nanoparticles: surface effects and properties related to biomedicine applications. International journal of molecular sciences. 2013;14:21266-305.

[133] Van Uitert L. Mg-Fe^{3+} Spinels (Mg ferrites) and Mg-Fe^{3+} Spinels with Substitutions. Proc IRE. 1956;44:1294.

[134] Jonker G. Analysis of the semiconducting properties of cobalt ferrite. Journal of Physics and Chemistry of Solids. 1959;9:165-75.

[135] Koops C. On the dispersion of resistivity and dielectric constant of some semiconductors at audiofrequencies. Physical Review. 1951;83:121.

[136] Koval V, Viola G, Tan Y. Biasing effects in ferroic materials. Ferroelectric Materials-Synthesis and Characterization: InTech; 2015.

[137] Bailey SE, Olin TJ, Bricka RM, Adrian DD. A review of potentially low-cost sorbents for heavy metals. Water research. 1999;33:2469-79.

[138] Barakat M. New trends in removing heavy metals from industrial wastewater. Arabian Journal of Chemistry. 2011;4:361-77.

[139] Mak SY, Chen D-H. Fast adsorption of methylene blue on polyacrylic acid-bound iron oxide magnetic nanoparticles. Dyes and pigments. 2004;61:93-8.

[140] Dhoke SK, Khanna A, Sinha TJM. Effect of nano-ZnO particles on the corrosion behavior of alkyd-based waterborne coatings. Progress in Organic Coatings. 2009;64:371-82.

[141] Johnson GA, Benveniste H, Black R, Hedlund L, Maronpot R, Smith B. Histology by magnetic resonance microscopy. Magnetic resonance quarterly. 1993;9:1-30.

[142] Fawell S, Seery J, Daikh Y, Moore C, Chen LL, Pepinsky B, et al. Tat-mediated delivery of heterologous proteins into cells. Proceedings of the National Academy of Sciences. 1994;91:664-8.

[143] Lewin M, Carlesso N, Tung CH, Tang XW, Cory D, Scadden DT, et al. Tat peptide-derivatized magnetic nanoparticles allow in vivo tracking and recovery of progenitor cells. Nature biotechnology. 2000;18:410-4.

[144] Gordon R, Hines J, Gordon D. Intracellular hyperthermia a biophysical approach to cancer treatment via intracellular temperature and biophysical alterations. Medical Hypotheses. 1979;5:83-102.

[145] Chouly C, Pouliquen D, Lucet I, Jeune J, Jallet P. Development of superparamagnetic nanoparticles for MRI: effect of particle size, charge and surface nature on biodistribution. Journal of microencapsulation. 1996;13:245-55.

[146] Chatterjee J, Haik Y, Chen C-J. Size dependent magnetic properties of iron oxide nanoparticles. Journal of Magnetism and Magnetic Materials. 2003;257:113-8.

[147] Pratsinis SE, Vemury S. Particle formation in gases: a review. Powder technology. 1996;88:267-73.

[148] Giersig M, Hilgendorff M. Magnetic nanoparticle superstructures. European journal of inorganic chemistry. 2005;2005:3571-83.

[149] Cao M, Liu T, Gao S, Sun G, Wu X, Hu C, et al. Single-crystal dendritic micro-pines of magnetic α-Fe_2O_3large-scale synthesis, formation mechanism, and properties. Angewandte Chemie International Edition. 2005;44:4197-201.

[150] Mao B, Kang Z, Wang E, Tian C, Zhang Z, Wang C, et al. Template free fabrication of hollow hematite spheres via a one-pot polyoxometalate-assisted hydrolysis process. Journal of Solid State Chemistry. 2007;180:489-95.

[151] Qin Z, Jiao X, Chen D. Preparation of coral-like magnetite through a glucose-assisted solvothermal synthesis. Cryst. Eng. Comm. 2011;13:4646-51.

[152] Massart R. Preparation of aqueous magnetic liquids in alkaline and acidic media. IEEE transactions on magnetics. 1981;17:1247-8.

[153] Raj K, Moskowitz R. Commercial applications of ferrofluids. Journal of Magnetism and Magnetic Materials. 1990;85:233-45.

[154] De Cuyper M, Joniau M. Mechanistic aspects of the adsorption of phospholipids onto lauric acid stabilized magnetite nanocolloids. Langmuir. 1991;7:647-52.

[155] Wooding A, Kilner M, Lambrick DB. "Stripped" magnetic particles. Applications of the double surfactant layer principle in the preparation of

water-based magnetic fluids. Journal of colloid and interface science. 1992;149:98-104.

[156] Zins D, Cabuil V, Massart R. New aqueous magnetic fluids. Journal of Molecular Liquids. 1999;83:217-32.

[157] Shen L, Laibinis PE, Hatton TA. Bilayer surfactant stabilized magnetic fluids: synthesis and interactions at interfaces. Langmuir. 1999;15:447-53.

[158] Sousa MH, Tourinho FA, Depeyrot J, da Silva GJ, Lara MCF. New electric double-layered magnetic fluids based on copper, nickel, and zinc ferrite nanostructures. The Journal of Physical Chemistry B. 2001;105:1168-75.

[159] Wan M, Li J. Synthesis and electrical–magnetic properties of polyaniline composites. Journal of Polymer Science Part A: Polymer Chemistry. 1998;36:2799-805.

[160] Butterworth M, Bell S, Armes S, Simpson A. Synthesis and characterization of polypyrrole-magnetite-silica particles. Journal of colloid and interface science. 1996;183:91-9.

[161] Tartaj P, Morales M, Gonzalez-Carreno T, Veintemillas-Verdaguer S, Serna C. Advances in magnetic nanoparticles for biotechnology applications. Journal of Magnetism and Magnetic Materials. 2005;290:28-34.

[162] Harris L, Goff J, Carmichael A, Riffle J, Harburn J, St. Pierre T, et al. Magnetite nanoparticle dispersions stabilized with triblock copolymers. Chemistry of Materials. 2003;15:1367-77.

[163] Thünemann AF, Schütt D, Kaufner L, Pison U, Möhwald H. Maghemite nanoparticles protectively coated with poly (ethylene imine) and poly (ethylene oxide)-b lock-poly (glutamic acid). Langmuir. 2006;22:2351-7.

[164] Dresco PA, Zaitsev VS, Gambino RJ, Chu B. Preparation and properties of magnetite and polymer magnetite nanoparticles. Langmuir. 1999;15:1945-51.

[165] Deng J, Peng Y, He C, Long X, Li P, Chan AS. Magnetic and conducting Fe_3O_4-polypyrrole nanoparticles with core-shell structure. Polymer international. 2003;52:1182-7.

[166] Xiong Z, Sun ZB, Zheng ML, Cao YY, Jin F, Chen WQ, et al. A facile method for the room-temperature synthesis of water-soluble magnetic Fe_3O_4 nanoparticles: Combination of in situ synthesis and decomposition of polymer hydrogel. Materials Chemistry and Physics. 2011;130:72-8.

[167] Bora D, Deb P. Fatty acid binding domain mediated conjugation of ultrafine magnetic nanoparticles with albumin protein. Nanoscale research letters. 2009;4:138.

[168] Hayashi K, Moriya M, Sakamoto W, Yogo T. Chemoselective synthesis of folic acid-functionalized magnetite nanoparticles via click chemistry for magnetic hyperthermia. Chemistry of Materials. 2009;21:1318-25.

[169] Mohammadi A, Daemi H, Barikani M. Fast removal of malachite green dye using novel superparamagnetic sodium alginate-coated Fe_3O_4 nanoparticles. International journal of biological macromolecules. 2014;69:447-55.

[170] Cao C, Xiao L, Chen C, Shi X, Cao Q, Gao L. In situ preparation of magnetic Fe_3O_4/chitosan nanoparticles via a novel reduction–precipitation method and their application in adsorption of reactive azo dye. Powder Technology. 2014;260:90-7.

[171] Huang L, Weng X, Chen Z, Megharaj M, Naidu R. Green synthesis of iron nanoparticles by various tea extracts: comparative study of the reactivity.

Spectrochimica Acta Part A: Molecular and Biomolecular Spectroscopy. 2014;130:295-301.

[172] Hao T, Yang C, Rao X, Wang J, Niu C, Su X. Facile additive-free synthesis of iron oxide nanoparticles for efficient adsorptive removal of Congo red and Cr (VI). Applied Surface Science. 2014;292:174-80.

[173] Dadfarnia S, Shabani AH, Moradi S, Emami S. Methyl red removal from water by iron based metal-organic frameworks loaded onto iron oxide nanoparticle adsorbent. Applied Surface Science. 2015;330:85-93.

[174] Gautam RK, Rawat V, Banerjee S, Sanroman MA, Soni S, Singh SK, et al. Synthesis of bimetallic Fe-Zn nanoparticles and its application towards adsorptive removal of carcinogenic dye malachite green and Congo red in water. Journal of Molecular Liquids. 2015;212:227-36.

[175] Nassar NN, Marei NN, Vitale G, Arar LA. Adsorptive removal of dyes from synthetic and real textile wastewater using magnetic iron oxide nanoparticles: Thermodynamic and mechanistic insights. The Canadian Journal of Chemical Engineering. 2015;93:1965-74.

[176] Debnath A, Deb K, Das NS, Chattopadhyay KK, Saha B. Simple chemical route synthesis of Fe_2O_3 nanoparticles and its application for adsorptive removal of Congo red from aqueous media: artificial neural network modeling. Journal of Dispersion Science and Technology. 2016;37:775-85.

[177] Pan L, Xu MY, Liu ZL, Du BB, Yang KH, Wu L, et al. Facile method for the synthesis of Fe_3O_4@ HCP core-shell porous magnetic microspheres for fast separation of organic dyes from aqueous solution. RSC Advances. 2016;6:47530-5.

[178] Dalvand A, Nabizadeh R, Ganjali MR, Khoobi M, Nazmara S, Mahvi AH. Modeling of reactive blue 19 azo dye removal from colored textile wastewater using l-arginine-functionalized Fe_3O_4 nanoparticles: optimization, reusability, kinetic and equilibrium studies. Journal of Magnetism and Magnetic Materials. 2016;404:179-89.

[179] Asfaram A, Ghaedi M, Hajati S, Goudarzi A. Synthesis of magnetic γ-Fe_2O_3-based nanomaterial for ultrasonic assisted dyes adsorption: modeling and optimization. Ultrasonics sonochemistry. 2016;32:418-31.

[180] Keyhanian F, Shariati S, Faraji M, Hesabi M. Magnetite nanoparticles with surface modification for removal of methyl violet from aqueous solutions. Arabian Journal of Chemistry. 2016;9:S348-S54.

[181] Rajput S, Singh LP, Pittman CU, Mohan D. Lead (Pb^{2+}) and copper (Cu^{2+}) remediation from water using superparamagnetic maghemite (γ-Fe_2O_3) nanoparticles synthesized by Flame Spray Pyrolysis (FSP). Journal of colloid and interface science. 2017;492:176-90.

[182] Reguyal F, Sarmah AK, Gao W. Synthesis of magnetic biochar from pine sawdust via oxidative hydrolysis of $FeCl_2$ for the removal sulfamethoxazole from aqueous solution. Journal of hazardous materials. 2017;321:868-78.

[183] Vinosha PA, Mely LA, Jeronsia JE, Krishnan S, Das SJ. Synthesis and properties of spinel $ZnFe_2O_4$ nanoparticles by facile co-precipitation route. Optik-International Journal for Light and Electron Optics. 2017;134:99-108.

[184] Amir M, Güner S, Yıldız A, Baykal A. Magneto-optical and catalytic properties of Fe_3O_4@ HA@ Ag magnetic nanocomposite. Journal of Magnetism and Magnetic Materials. 2017;421:462-71.

[185] Altıntıg E, Altundag H, Tuzen M, Sarı A. Effective removal of methylene blue from aqueous solutions using magnetic loaded activated carbon as novel adsorbent. Chemical Engineering Research and Design. 2017;122:151-63.

[186] Zhang J, Shao Y, Hsieh CT, Chen YF, Su TC, Hsu JP, et al. Synthesis of magnetic iron oxide nanoparticles onto fluorinated carbon fabrics for contaminant removal and oil-water separation. Separation and Purification Technology. 2017;174:312-9.

Chapter 2
Characterization Techniques

Chapter-2

Characterization Techniques

"This chapter presents a view on different characterization techniques for the characterization of nanoparticles. Structural as well morphological analysis of IONPs are identified by XRD, SEM, BET and optical propertied determination techniques like UV-Visible absorption spectroscopy and PL. The leading objectives and a brief framework of instrumentation and use of these techniques used for properties determination of materials are discussed in detail."

2.1. Synthesis method:

α-Fe_2O_3, PVP coated Fe_3O_4, $CoFe_2O_4$, $Cd_{0.4}Ni_{0.6}Fe_2O_4$ nanoparticles have been prepared by chemical co-precipitation method because it is conventional and innumerable cost-effective way for the formation of Fe_3O_4 or black iron oxides. This protocol involves of mixing Fe-III and Fe-II in higher basic environments. pH of the reaction, ionic strength and percentage of salts are the aspects which influence the quality of NPs fabricated. However suitable modifications of this procedure have been performed where an excellently control over dimension and magnetic properties is achieved. Stabilizers can also be added in reaction to produce highly stabilized nanoparticles for the paramount properties and uses [1-3].

2.2. Materials employed:

All the chemicals used in the synthesis of NPs were of analytical grade, purchased from Merck and Fischer Scientific chemicals and were used without any further purification. The details of the general experimental technique and materials employed are described in upcoming chapters include:

Ferrous sulphate ($FeSO_4 \cdot 7H_2O$), Ferric chloride ($FeCl_3$), Ammonium hydroxide solution (NH_4OH), Sodium Hydroxide (NaOH), Polyvinyl pyrrolidone (PVP), Cetyl Trimethyl Ammonium bromide (CTAB), Copper chloride ($CuCl_2$), Cobalt Chloride ($CoCl_2$), Rhodamine B (RhB), Congo red dye (CR), Methylene Blue (MB) and distilled water. The structure dyes used in this investigation are is shown in Figure 2.1.

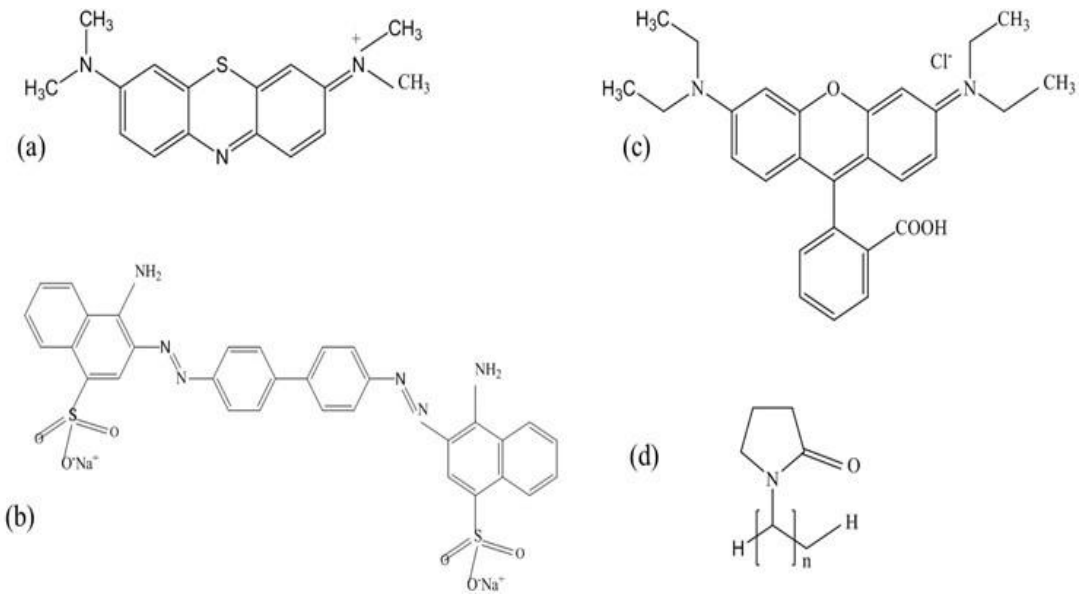

Figure 2.1: (a)-Methylene blue (b)-Rhodamine b6 (c)-Congo red Dye (d)-Polyvinyl pyrolidone (PVP)

2.3. Characterization Technique:

In this chapter the description of instrumental techniques and experimental set up for characterization fabricated nanomaterials and dyes degradation/removal have been discussed. The characterization techniques include X - ray diffraction (XRD), scanning electron microscope (SEM), Energy Dispersive X-ray spectroscopy (EDX), Fourier transform infrared spectroscopy (FTIR), BET surface area analyzer (BET), UV-Visible absorption spectroscopy (UV-Vis) and photoluminescence spectroscopy (PL).

2.3.1. X-Ray Diffraction (XRD):

X-ray diffraction is a precise non-destructive advantageous tool for investigation of crystal size, (often mentioned to as main particle size), morphology, and physical properties of material, thin film, chemical configuration and crystallographic structure [4, 5]. This technique measures innumerable structural properties of the crystalline phase such as imperfection structure, strain, and particle size and phase composition. It defines not only breadth of the film but also defines the arrangement in amorphous material such as polymeric material.

2.3.1.1. Basic Principle:

X-ray diffraction depends on constructive interference of monochromatic X-rays from a crystalline material. The X-rays are produced by a cathode ray tube and are cleaned to create monochromatic radiation, collimated and focused in-to the sample. The X-rays principally act together with electrons present in atoms, collide and specific photons from the incident ray are deflected distant from original. The X-rays interfere constructively and destructively generating a diffraction pattern on the detector. The incident X-ray radiation generated a Bragg's peak if their reflections from the numerous planes interfered constructively. The interference is constructive, what time the phase variation is a multiple of 2λ, this circumstance can be denoted by Bragg's law,

$$n\,\lambda = 2d \sin\theta$$

Where n is an integer, λ is the wavelength of incident wave, d is the gaps between the planes in the atomic lattice and θ is the angle amongst the incident ray and the scattering planes. Schematic diagram of Bragg's Law is shown in Figure 2.2.

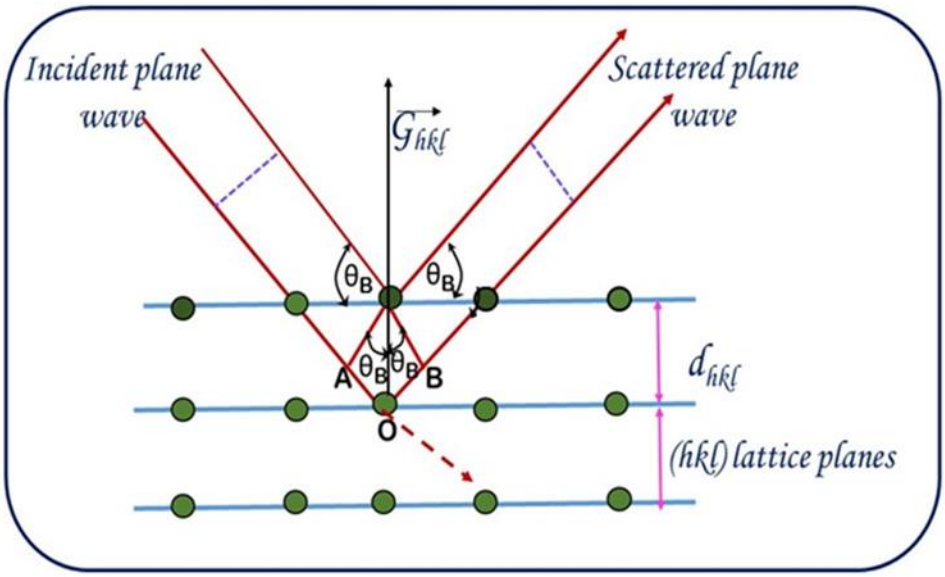

Figure 2.2: Bragg's low

2.3.1.2. Instrumentation:

A characteristic PXRD involves a source of radiation, a monochromator to choose the wavelength, slits to modify the outline of the beam, a sample and a detector. A goniometer is used for acceptable change of the sample and the detector locations. The goniometer mechanism help the material and detector, approve to precise movement. The source of X-rays system involve various components; the most frequent being KĮ and Kα. The definite wavelengths are distinctive of the objective material (Cu, Fe, Mo and Cr). The purpose of monochromators and filters is to absorb undesirable emission with wavelength Kα, while allowing the desired wavelength KĮ to pass through. The X-ray radiation most universally used is that emitted through copper, whose characteristic wavelength for the KĮ radiation is equivalent to 1.5418 Å. The filtered X-rays are collimated and concentrating onto the sample as showed in the Figure 2.3. When the incident ray offensives a powder sample, diffraction arises in each conceivable orientation of 2ș. The diffracted ray may be observed by using a transportable detector for instance a Geiger counter, which is associated to a chart recorder. The counter is fixed to scan over an assortment of 2ș values at a continuous angular velocity. Routinely, a 2ș range of 5 to 70˚ is appropriate to cover the greatest useful part of the powder pattern. The scanning speediness of the counter is generally 2ș of 2Û min^{-1}. A detector records and procedures this X - ray signal and transforms the signal to a count frequency which is then fed to a device for instance a printer or computer monitor. The sample must be milled to fine powder previously loading it in the glass sample holder. Schematic representation of instrumentation of XRD are shown in Figure 2.3.

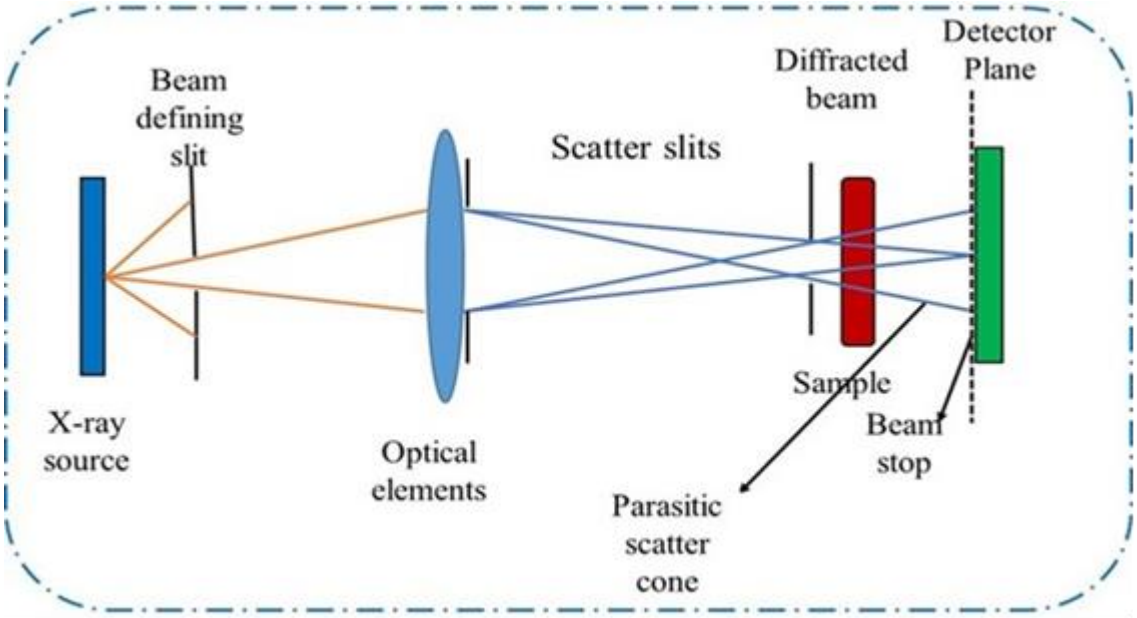

Figure 2.3: Schematic illustration of x-ray diffraction

2.3.1.3. Particle size determination:

As soon as the size of the discrete crystallite is smaller than 0.1 μm, the term particle size is used. For the calculation of mediocre particle size is, scherrer equation is applied [6]. The breadth of the diffracted curve escalates with diminution in particle size of the nanomaterial. The width β is frequently measured in radians, at intensity one and the unchanged to half the maximum intensity (FWHM). One can take β as half the divergence amongst the acute angles, at which the intensity is zero, supposing that the diffraction line is triangular in shape [7, 8] as revealed in Figure 2.4.

$$\beta = (1/2)\ (2X_2 - 2X_1) \text{ or}$$

$$\beta = (X_2 - X_1)$$

The average grain size is computed from the Scherrer formula,

$$D = 0.9\lambda / \beta \cos\theta$$

Where, λ = wavelength of copper Kα line (1.5418 Å).

θ = diffraction angle.

β =FWHM.

D = ordinary particle size.

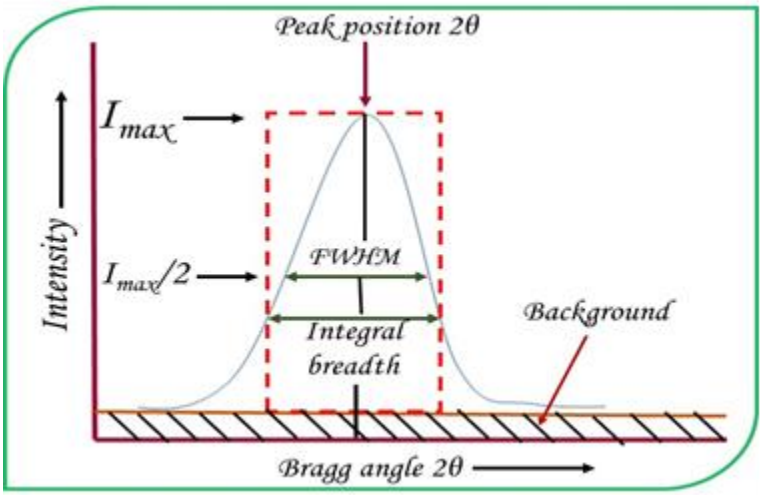

Figure 2.4: Full width half maxima (FWHM)

2.3.1.4. Important application of XRD:

Firstly Peak indexing is identified by XRD spectra and uses are described below:

(a) Particle size calculation:

Ordinary particle size has been computed by using Debye-Scherrer equation [9]

$$D = \frac{0.9\lambda}{\beta \cos\theta} \quad (1)$$

Where *'λ'* = wavelength of X-Ray (0.1541 nm), *'β'* = FWHM, *'θ'* = diffraction angle and *'D'* = particle size. The value of *d* = the interplanar spacing between the atoms is computed by using Bragg's Law [10].

$$n\lambda = 2d \sin\theta \quad (2)$$

(b) Instrumental Broadening:

As soon as particle size is fewer than 100 nm, noticeable widening in x-ray diffraction lines will found. Diffraction pattern will confirmation widening because of particle size and straining. The detected line widening will be used to determine the

average size of the particles. The overall widening of the diffraction peak is owing to the sample and the instrument. The sample broadening is interpret by

$$FW(S)\times\cos\theta=\frac{K\times\lambda}{size}+4\times strain\times\sin\theta \tag{3}$$

The total broadening βt is calculated by the equation

$$Bt^2=\left\{\frac{0.9\lambda}{D\cos\theta}\right\}+\{4\varepsilon\tan\theta\}+\beta_o^2 \tag{4}$$

ε is strain and βo instrumental broadening. The average particle size D and the strain of the experimentally detected widening of numerous peaks will be computed at the similar time using least squares method. Instrumental widening is shown in Figure 2.5 [11]. Williamson and Hall suggested a method for deconvoluting size and strain widening by watching at the peak breadth as a function of 2θ. Here, Williamson-Hall plot is plotted with sin θ on the x-axis and βcosθ on the y-axis (in radians). A linear fit is got for the data. From this fit, particle size and strain are take out from y-intercept and slope correspondingly [12]. The computed particle size is 24 nm and strain is 0.0012. Figure 2.5 [11]. Shows Williamson Hall Plot.

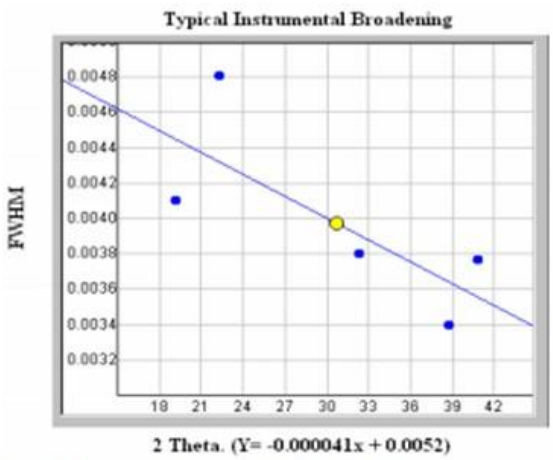

Fig.3. Typical Instrumental Broadening.
y = -0.000041x + 0.0052

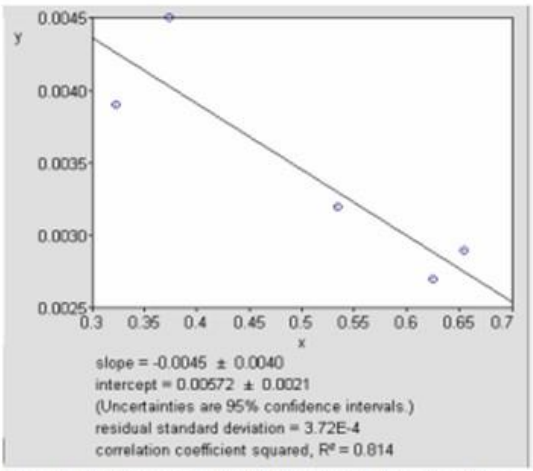

Fig.4. Williamson Hall Plot is indicating line broadening value due to the equipment.

Figure 2.5: Represent instrumental broadening

Line broadening investigation is greatest accurate when the broadening due to particle size effects is at smallest twofold times the contribution owing to instrumental widening. The size range is computed over which this method will be maximum precise. A rough higher limit is expected for reasonable exactness by observing at the particle size that would lead to widening equivalent to the instrumental widening.

(c) Dislocation Density:

In materials science, a dislocation is a crystallographic imperfection, or irregularity, within a crystal structure. The dislocation density (δ) in the sample has been determined using expression [13].

$$\delta = \frac{15\beta \cos\theta}{4aD} \tag{5}$$

Where δ = dislocation density, β = broadening of diffraction line, θ = Bragg's diffraction angle (in degree), a = lattice constant (in nm) and D = particle size (in nm).

(d) Crystallinity Index:

Crystallinity is estimated through comparison of crystallite size as ascertained by SEM particle size determination. Crystallinity index Eq. is presented below:

$$\text{Icry}= \frac{Dp(SEM, TEM)}{Dcry(XRD)} \left(Icry \geq 1.00\right) \tag{6}$$

(e) Specific Surface Area (SSA):

SSA is a material property. It is a resultant scientific value that can be used to decide the category and properties of a material. It has a particular significance in case of adsorption, ununiformed catalysis and reactions on surfaces. SSA is the Surface Area (SA) per mass.

$$SSA = \frac{SApart}{Vpart * density} \tag{7}$$

Here Vpart is particle volume and SApart is particle SA [14]

$$S=6*10^3/D_p\rho \quad (8)$$

(f) Unit Cell Features:

Unit cell features defined from XRD such as structure, point group, density, crystal lattice, space group, packing fraction, bond angle, particle size, lattice parameters [11].

2.3.1.5. Identification of crystal structure of material:

The powder diffraction of a material is the characteristic property of the material and forms a category of fingerprint of the material to be identified. The peaks of the XRD pattern can be matched by means of the standard accessible data for the certification of the structure. For the purpose of comparison, numerous standards patterns are accessible, selected of which Willars Hand book and JCPDS files are, in and National Bureau of Standards.

2.3.2. Scanning Electron Microscope (SEM):

2.3.2.1. Basic Principle:

The SEM is a precise appropriate imaging technique that applied a ray of electrons to obtain extraordinary magnification images of samples. Electrical tools to achieve visually ultrafine 3-dimensional evidences of the surface. SEM analysis is revealed the confirmation about the surface features and elemental composition by the electron-sample interactions. Images of SEM is fashioned by rastering (scanning) a beam crossways the sample and making the image point by point [15, 16].

2.3.2.2. Instrumentation:

The SEM technique is very prosperous instrument that create a largely magnified image by using the electrons instead of light to form an image. The schematic view of the SEM are shown in Figure 2.6. The development of a ray of electrons is formed at the upper of electron microscope by an electron gun. Then the

ray of electron tracks a perpendicular path through the microscope, which is detained inside a vacuum. During this process the electron beam journeys through electromagnetic fields and lenses, which target the beam down in the direction of the sample. When the ray strike the sample, electrons and X-rays are turned out from the sample. These X-rays, backscattered electrons and secondary electrons are collect through the Detectors and then transform them into an indication that is directed to a screen equivalent to a television monitor. After completion of this process it produces the finishing image**.** For the SEM analysis, the powder and completely dried samples were used and located on the carbon tape which was closely attach to the sample holder. SEM JEOL were used to investigation the surface morphology of the sample.

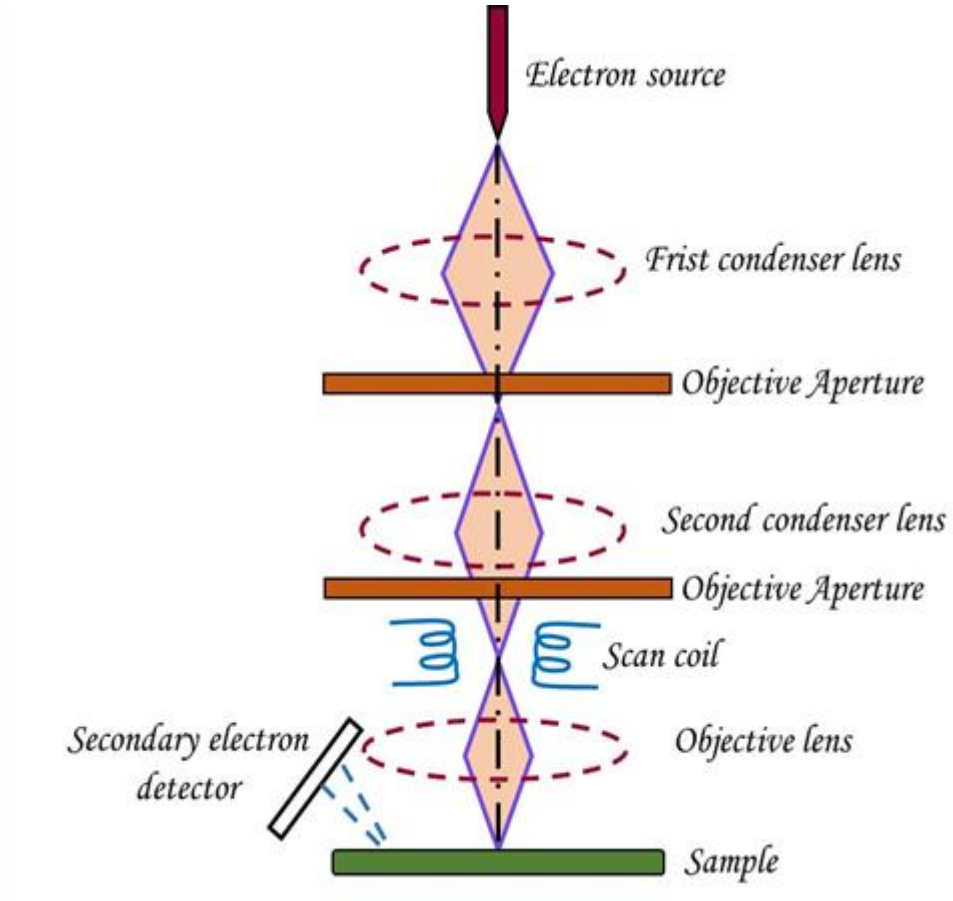

Figure 2.6: Schematic diagram of scanning electron microscope

2.3.2.3. Typical application:

(a) SEM is used for the analysis of morphology of nanoparticles fabricated by a number of synthesizing technique.

(b) SEM is also used for analysis of shape and size of nanoparticles.

2.3.3. Energy dispersive X-ray spectroscopy:

EDX is a chemical microanalysis technique used in conjunction with scanning electron microscopy (SEM) [17]. The EDX detects X-rays give out from the sample in the course of bombardment by an electron ray to characterize the elemental structure of the analyzed volume. Features or phases as lesser as 1 μm or less can be examined. As soon as the sample is bombarded by the SEM's electron ray, electrons are turned out from the atoms comprising the sample's surface. The consequential electron positions are filled by electrons from an upper state, and an X-ray is give out to balance the energy variance between the two electrons' states.

The X-ray energy is distinguishing of the element from which it was released and the superfluous energy is released in the form of an X-ray. The deliverance of X-rays generates spectral lines that are extremely precise to separate elements; thus, by investigating the X-ray emission data the sample in question can be characterized. For instance, a peak identical to the magnitude of energy possessed by x-rays created by an electron in the L-shell going down to the K-shell is recognized as a Kα peak. The peak subsequent to x-rays emitted by electrons transition from upper levels to the K-shell is identified as Kα, Kβ, Kγ, etc as revealed in Figure 2.7. The EDX X-ray detector analyze the relative abundance of produced X-rays versus their energy. The detector is characteristically a lithium drifted silicon. As soon as an incident X-ray strikes the detector, it produces a charge pulse that is proportional to the energy of the X-ray. The charge pulse is renewed to a voltage pulse (which leftovers proportional to

the X-ray energy) by a charge-sensitive preamplifier. The signal is then sent to a multichannel analyzer where the pulses are sorted by voltage. The energy, as examined from the voltage measurement, for apiece incident X-ray is sent to a computer for display and further data estimation. The spectrum of X-ray energy vs. counts is evaluated to find out the elemental composition of the sampled volume.

2.3.3.1. Typical Applications:

(a) A complete elemental spectrum can be taken in only in certain time (seconds).

(b) EDX can be used in semi-quantitative way to analyzed chemical composition by peak-height ratio comparative to a standard.

(c) Corrosion evaluation, phase analysis and distribution.

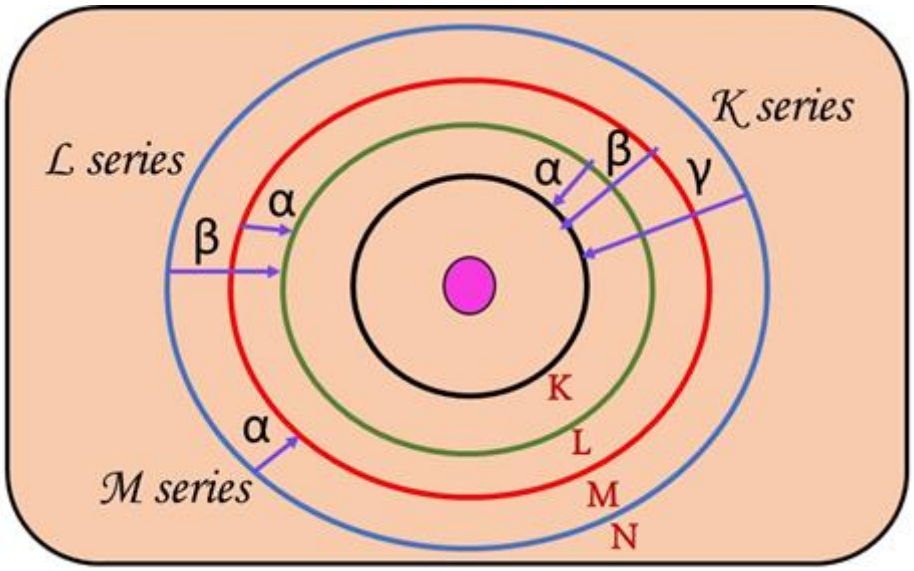

Figure 2.7: Schematic diagram of energy dispersive x-ray spectroscopy

2.3.4. Fourier transform infrared spectroscopy (FTIR):

The FTIR is an important technique for the identification of material by matching spectrum of unidentified compound with reference spectrum (finger printing), analysis of functional groups in unidentified substances. The IR region of the electromagnetic spectrum is deliberated to concealment the range starting from 50 to 12,500 cm^{-1} approximately.

2.3.4.1. Basic Principle:

At what time infrared light is passed through a sample, selected vibrational frequencies are absorbed, although additional frequencies are transmitted devoid of being absorbed. The transitions elaborate in the infrared absorption are interrelated with the vibrational modifications in the molecule. Different coordinating bonds / functional groups have dissimilar vibrational frequencies and therefore the existence of these bonds in a material can be investigated by distinguishing frequency as an absorption band in the infrared spectrum. The plot amongst transmittance and wavenumber is called infrared spectrum.

2.3.4.2. Instrumentation:

FTIR have in modern periods substituted dispersive instruments for maximum applications owing to their superior speed and sensitivity. They have importantly prolonged the abilities of infrared spectroscopy and have been valuable to numerous areas that are very arduous or approximately impossible to evaluate by dispersive instruments. Instead of inspecting every component frequency consecutively, as in a dispersive IR spectrometer, everything frequencies are investigated at the same time in FTIR spectroscopy. In Fourier transform system three rudimentary spectrometer components: radiation source, interferometer and detector.

The functional block Figure of the FTIR spectrometer is presented in the Figure 2.8. Infrared radiation is comes from a broadband source is firstly focused into an interferometer, where it is separated and then recombined subsequently the split beam travel through different optical pathways to produce constructive and destructive interference. Afterward, the resulting beam passes over the sample compartment and reaches to the detector. Preparation of Sample is very informal. Almost all types of samples are investigated by this instrument such as solid, liquid or

gas sample. The sample to be investigated (minimum of 10 µg) should be crushed into KBr matrix or dissolved in an appropriate solvent (CCl_4 and CS_2 are selected). Water should be exclude from sample if possible. In case of solid samples, it is mixed with solid KBr pallet (transparent in the middle - IR region), then milled and pressed. FTIR were performed by using Perkin Elmer FTIR spectrophotometer by stock KBr pellet technique.

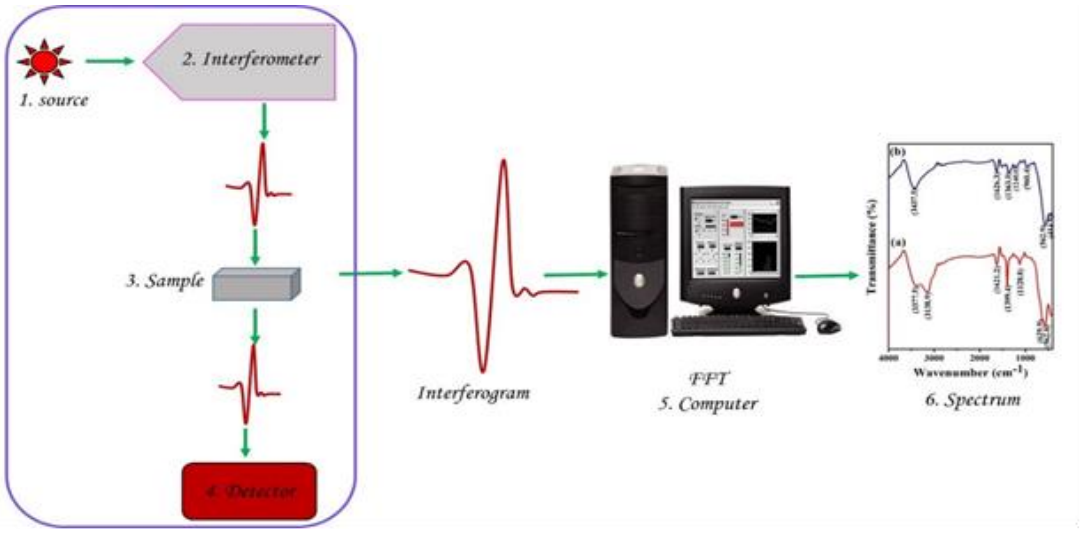

Figure 2.8: Schematic diagram of Fourier transform infra-red spectroscopy

2.3.4.3. Application of FTIR:

(a) The existence of the stabilizer such as polymer coating of IONPs blend was confirmed by means of FTIR spectroscopy[18].

(b) The analysis of bonding is formed in sample is also confirmed by FTIR spectroscopy.

(c) FTIR will also help to investigation of functional groups existing in the NPs, so this technique is used for qualitative investigation of materials. Each one functional group possess one or more distinguishing peaks at not the same wave numbers.

2.3.5. Brunauer, Emmett and Teller (BET):

The BET technique is the most frequent method for analysis of surface area of powder sample and absorbent materials. Nitrogen gas in general employed as the

probe molecule and is unprotected to a solid under investigation at liquid nitrogen circumstances (*i.e.* 77 K). The surface area of the solid is estimated from the measured monolayer capacity and awareness of the cross-sectional area of the molecule being used as a probe. For the case of nitrogen, the cross-sectional area is taken as 16.2 $Å^2$/ molecule.

2.3.5.1. Basic Principle:

The principle of B.E.T surface area analysis is that at smaller pressures gas adsorbs to solids in a monolayer. The surface area covered by this layer is analyzed based on the number of gas molecules in a monolayer and the dimensions of individual molecules. Monolayer creation of gas molecules is thus useful to define the precise surface area, while the principle of capillary condensation can be used to investigate porous physical appearance such as pore volume and pore size distribution. B.E.T analysis be responsible for precise exact surface area evaluation of materials by nitrogen multilayer adsorption measured as a function of relative pressure using a completely automated analyzer. Barrett-Joyner-Halenda (BJH) plot can also be determine pore size dissemination and specific pore volume using adsorption and desorption techniques. Schematic representation of BET is shown in Figure 2.9.

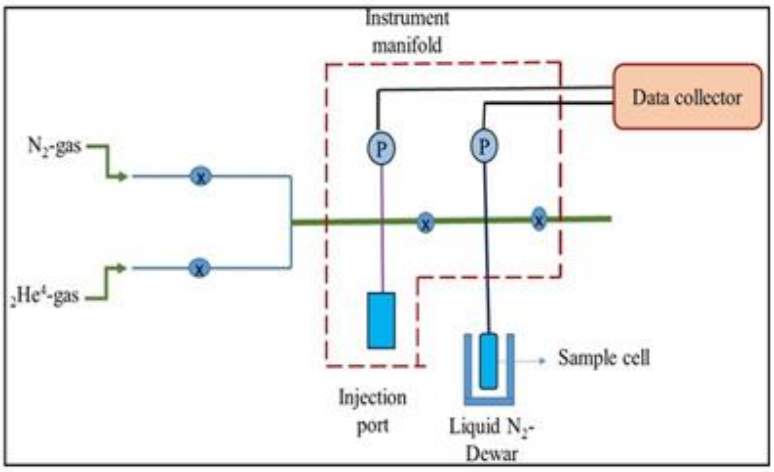

Figure 2.9: Schematic diagram of BET

2.3.5.2. Significant application of BET:

(a) From BET analysis surface properties is analyzed.

(b) Surface area is significant property of nanoparticles for the separation of dyes by adsorption procedure is calculated by BET.

(c) Pore volume, pore radius, pore size distribution is also measured by BET.

2.3.6. UV-Visible spectroscopy:

UV-Visible is a reliable and accurate analytical research laboratory assessment route that permits for the investigation of a material [19]. This absorption spectroscopy refers to in the ultra-violet and visible spectral region. In this range of the electromagnetic spectrum, molecules exhibit electronic transition. When samples are uncovered to light having an energy ($E = h\upsilon$ where *'E'* is energy in joules, '*h'* is Planck's constant 6.62 × 10 – 34 J s and 'υ*'* is frequency in Hertz), that matches a probable electronic transition present inside the molecule, specific of the light energy will be absorbed as the electron is stimulated to a greater energy orbital. An optical spectrometer minutes the wavelengths at which absorption take place, simultaneous with the amount of absorption at respectively wavelength. The resulting spectrum is plot between absorbance (A) versus wavelength (λ). The optical properties of materials can be evaluated with the support of UV-Visible spectra.

2.3.6.1. Basic Principle:

The absorbance of light by molecules in the solution is based on the Beer - Lambert law, $A= I/I_0= \varepsilon*b*c$ where, $I_0$is the intensity of the reference beam and *I* is the intensity of the sample beam, ε is the molar absorptivity with units of $Lmol^{-1}cm^{-1}$, *b* = path length of the sample in centimeters and *c* = concentration given solution expressed in $molL^{-1}$.

2.3.6.2. Instrumentation:

The UV-Visible spectrophotometers are mainly divided into five components like light source, double beams (reference and sample beam), a monochromator, a detector and a recording device. In this instrument a tungsten filament lamp for visible and deuterium discharge lamp for UV is usually used as a source for measurements. The light coming out from source is separated into double beams - the reference beam and the sample beam as displayed in the Figure 2.10. The shape of sample cell and reference cells are rectangular quartz/glass containers; they consist the solution (to be tested) and pure solvent, in that order. The spectrometer minutes the proportion between the reference and sample beam concentrations. The recorder plots the absorbance (A) against the wavelength (λ). The sample is organized into a paste and then liquefied into the solvent to form a dilute sample solution. This sample solution is occupied to mark line of the sample cell. In the current work, UV-Visible absorption examines were performed by Cary win 100 UV-Visible spectrophotometer.

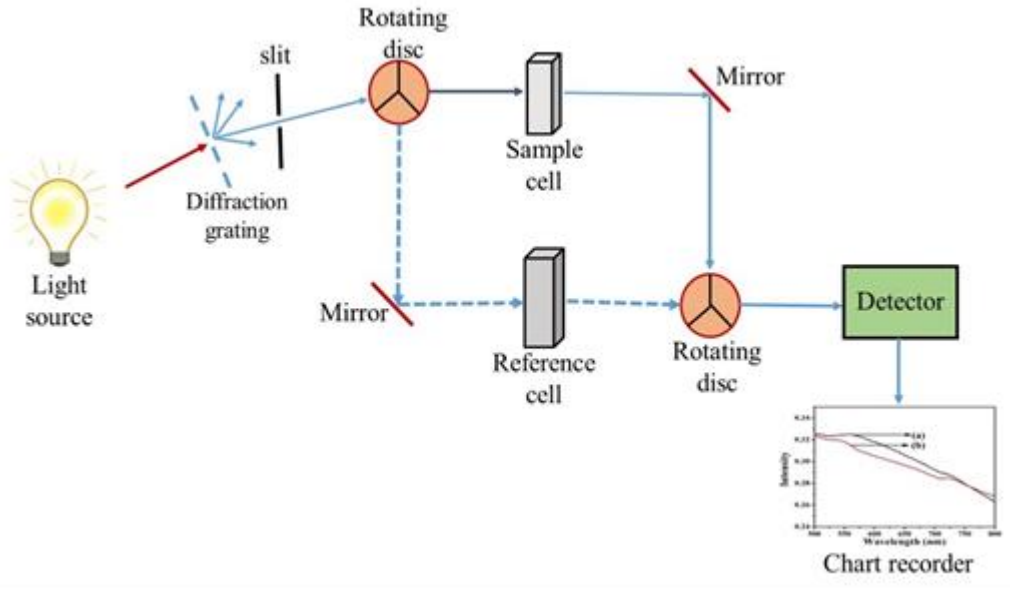

Figure 2.10: Schematic diagram of ultra violet-visible spectroscopy

2.3.6.3. Important application of UV-Vis:

(a) Optical properties of nanomaterials is identified by this technique.

(b) Band gap is also calculated from this technique by using tauc relationship.

(c) Tauc plot is used to calculation of the optical bandgap, or Tauc gap, in semiconductors. The Tauc gap is often used to describe practical optical properties of amorphous materials.

Direct band gap energy of materials was calculated from the Tauc relation:

$$(\varepsilon h\nu)^2 = P(Eg - h\nu) \quad (9)$$

Where ε is the molar extinction coefficient, h is plank constant, v is frequency of light, Eg is the band gap energy and P is the arbitrary constant. The linear part of the $(\varepsilon h\nu)^2$ verses $h\nu$ graph was used to calculate the band gap values. The intercept of tangent at the x axis gives Eg value are shown in Figure 2.11.

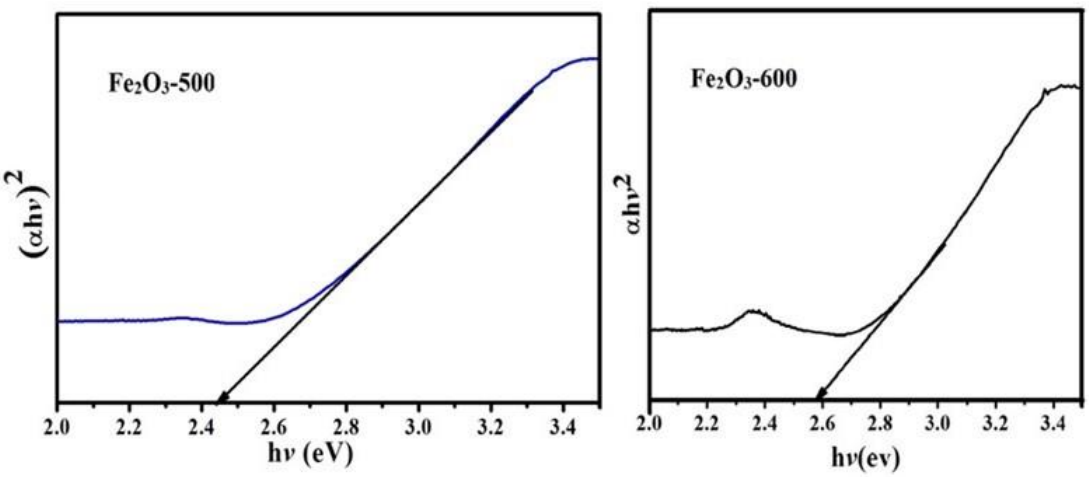

Figure 2.11: Band gap of iron oxide nanoparticle

2.3.7. Photoluminescence Spectroscopy (PL):

PL spectroscopy is a contactless, non-destructive technique to probe the electronic structure of materials. The intensity and spectral content of the radiated photoluminescence is a straight measure of numerous important material properties,

plus band gap determination, dirtiness levels and imperfection detection, recombination mechanisms.

2.3.7.1. Introduction to luminance:

Photoluminescence (PL) is a non-destructive analytical technique is used for the examination of extrinsic and intrinsic properties of semiconductors materials. Photo-excitation process take place at what time light is concentrated onto a sample and it becomes absorbed and imparts superfluous energy to the material. One of the methods this excessive energy can be dissolute by the sample is through the emissions of light. This procedure is known as luminescence. As soon as luminescence is go together with photo-excitation it is termed photoluminescence. If the emission energy is a less significant amount of than the excitation energy, this type of emission is known as 'Stokes emission', as well as, if the emission energy is higher than the excitation energy, this type emission is known as 'Anti-Stokes' emission. Commonly Stokes emission is perceived for the reason that the changeability in energy is caused by the transformation of the exciting light, to a larger or smaller extent; to non-radiating vibrational energy of atoms or ions [20].

In this technique the semiconductor material beneath investigation is excited optically and at that moment the PL spectrum of the extemporaneous emission from radiative recombination in the semiconductor band gap is found. For the time period of the PL procedure, together radiative and nonradiative recombination happens. The PL technique be able to be used to identify the bandgap, impurity levels, imperfections detection and recombination process in the semiconductor materials. Innumerable most significant material properties give a straight measure of the spectral content and intensity of this photoluminescence.

Luminescence is further fragmented up into fluorescence and phosphorescence. A molecule in an excited state radiates energy subsequently outstanding in a metastable state for an objectively long time; the procedure is called as phosphorescence. The luminescence procedure in which the molecule radiates radiation as it falls in a straight line from an excited state to an inferior energy state is acknowledged as fluorescence. The time scale of the procedure is of the order of 10^{-8} s. Fluorescence radiation is owing to acceptable transitions ($\Delta S = 0$) from singlet excited state to the singlet ground state. If a molecule in an excited state releases energy subsequently remaining in a metastable state for an objectively long time, the process is called as phosphorescence. The time scale of the phosphorescence procedure be contingent on the energy gaps between the metastable state and the adjacent energy state to which transition is acceptable and may be of the order of 10^{-6} seconds to minutes, hours or uniform days. This type of transition is owing to not allowed transition ($\Delta S \neq 0$) from the excited metastable state to the lower ground state.

2.3.7.2. Origin of fluorescence and phosphorescence:

The absorption of energy through a molecule increases it to an excited state. This excited state may be rotational, vibrational or electronic are possible but these excited states are depending upon the energy of exciting photons. If the order of energy of exciting photon is 10^{-3} is liable for rotational excited states, if the energy is of the order of 0.1 eV at that moment vibrational states can be excited, and if the energy is of the order of greater than a little electron volts then electronic states can be excited. The analogous spectra are in microwave for rotational, infrared for vibrational and visible as well as ultraviolet array for electronic energy states. A molecule in an excited electronic state can misplace energy and coming back to its

ground state in a number of ways. When the molecule may come back to the ground state through the emission of a photon of equivalent energy in a single step. One more probability is that it may mislay certain of its vibrational energy in collision with other molecules. Therefore descending radiative transition instigates from an inferior vibrational level in the higher electronic state. This phenomenon is named fluorescence and the fluorescent radiation is continuously of lower frequency are presented in Figure 2.12 (a). In the molecular spectra, radiative transitions between electronic states of dissimilar over-all spin are not acceptable according to spin selection rule (spin selection rule $\Delta S = 0$). Figure 2.12 (b) shows a circumstances in which a molecule in its singlet (total spin quantum no $\Delta S = 0$) ground state, absorbs a photon and is elevated to singlet excited state. In collisions the molecule can go through non-radiative transitions to an inferior vibrational level. Now, inferior vibrational level possibly will have the equivalent energy as one of the triplet (S=1) excited state. Then an assured likelihood of the molecule for a move to occur to a triplet state. Further collisions in the triplet state transport the molecule's energy beneath that of the crossover point, so that it is at the present stuck in the triplet state and at the completion of the procedure reaches $v = 0$ level. As the radiative transition from a triplet toward a singlet state is not acceptable ($\Delta S \neq 1$) according to spin selection rule, which means not that it is intolerable but that it has only an insignificant likelihood of occurring. Such transitions have extensive lifetimes, and the resulting phosphorescent radiation may be radiated in the time pause of the order of seconds, minutes or even hours subsequently the preliminary excitation is switched off.

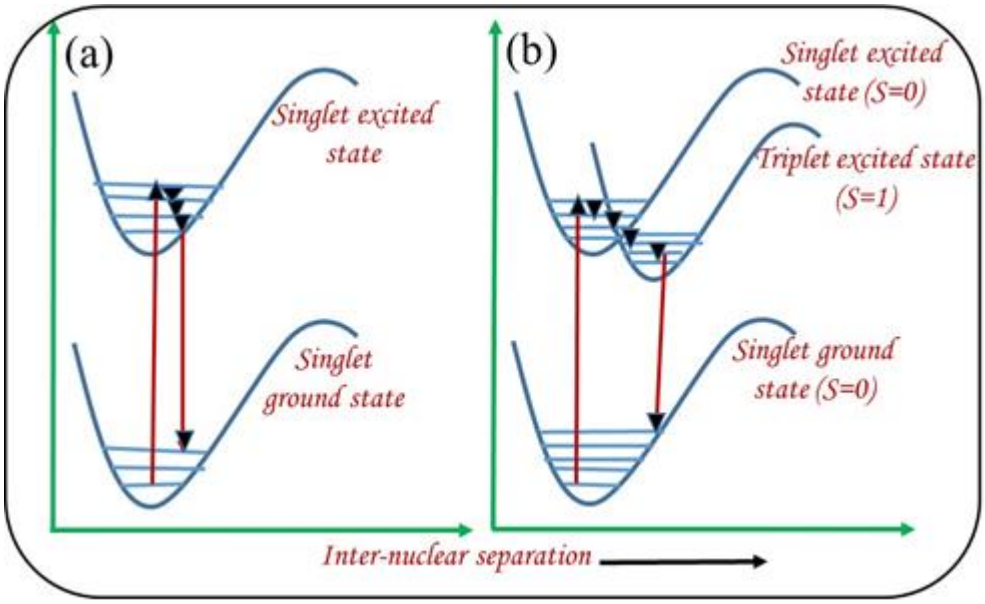

Figure2.12: Schematic diagram of (a) Fluorescence (b) Phosphorescence

2.3.7.3. Instrumentation:

The leading constituents of fluorescence instruments: a source of light, a sample holder and a detector. A schematic illustration of a fluorimeter is presented in Figure 2.13. The light source generate light photons over a wide energy spectrum, typically range of this instrument is 200 to 900 nm. Photons interrupt on the excitation monochromator, which certain transmits light in a contracted range positioned about the specified excitation wavelength. The transmitted light passes through modifiable slits that regulate magnitude and resolution by further limiting the range of transmitted light. The filtered light passes into the sample cell producing fluorescent emission by fluorophors inside the sample. Emitted light come into the emission monochromator, which is positioned at a 90 º angle from the excitation light pathway to eliminate background signal and decrease sound owing to stray light. Once more, emitted light is transmitted in a contracted range centered about the specified emission wavelength and going away through adjustable slits, finally towards the inside the photomultiplier tube (PMT). The signal is amplified and produces a voltage that is proportional to the measured radiated intensity. Sound in the counting procedure

arises mainly in the PMT. Therefore, 28 spectral resolution and signal to noise is directly associated to the particular slit widths. Sample preparation procedure is the identical as that of UV-Visible spectroscopy. In both the cases, the sample cell (cuvette) must be free from impurities.

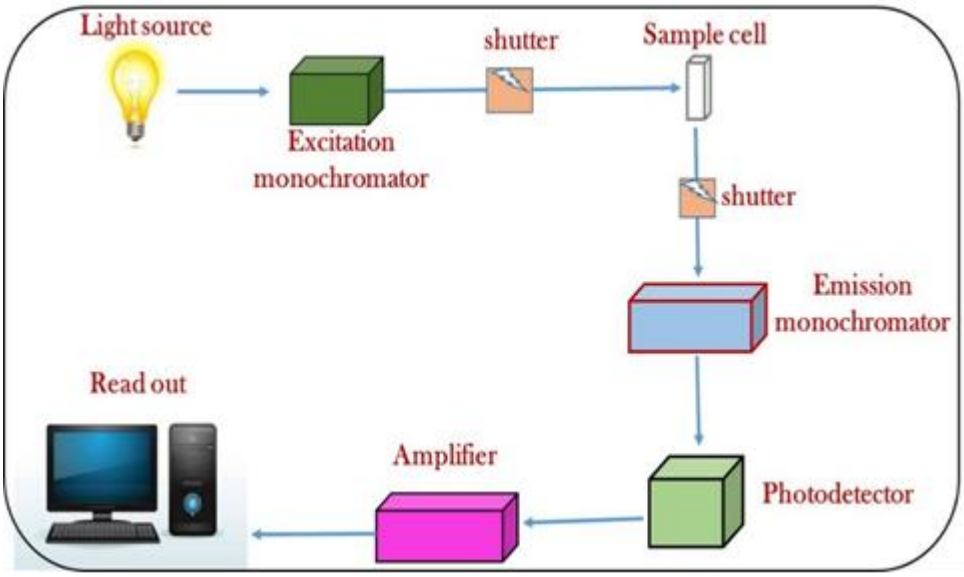

Figure 2.13: schematic diagram of fluorescence spectrophotometer

1.4. Important application:

(a) PL is a frequently used this technique for investigation of the optical and electronic properties of semiconductors nanoparticles.

(b) Photocatalytic activity and band gap is also find out by PL.

2.3.8. Photocatalytic activity:

CR, RhB, MB were used as probe molecules to investigation of the photocatalytic activity of bare and Polymer coated Fe_2O_3 and Fe_3O_4 nanoparticles respectively in response to visible light irradiation. Photocatalytic activity process is shown in Figure 2.14. The photocatalytic activity of as prepared Fe_2O_3-500 and Fe_2O_3-600 materials was determined by photodegradation of dye methylene blue (Meb) under visible light exposure using Xe lamp (1000 W). The photocatalytic degradation efficiency was calculated using the following equation:

(%) degradation = $(A_0 - A)/A_0) \times 100$

Where A_0 represents the initial absorbance of the dye solution and A; the absorbance after irradiation at particular time.

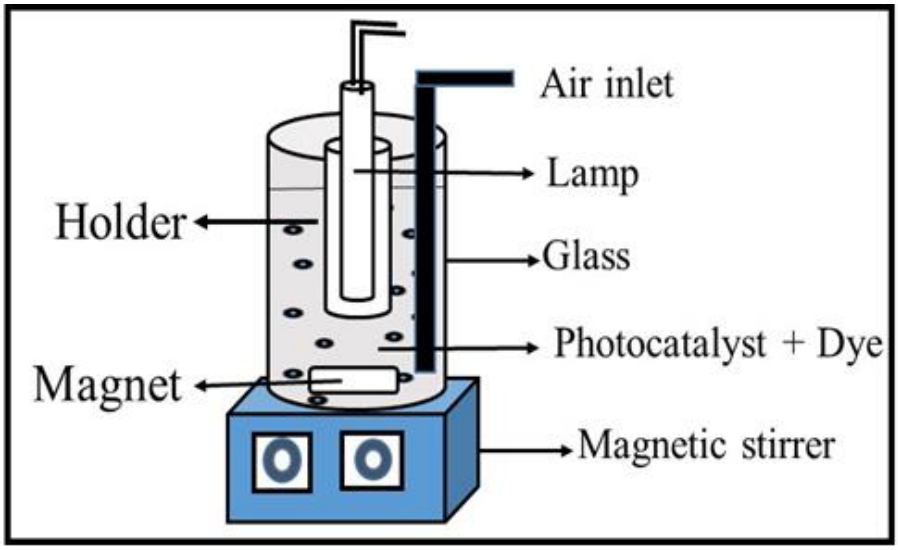

Figure 2.14: Schematic representation of phtocatalytic activity

2.4. References:

[1] Blanco-Andujar C, Ortega D, Pankhurst QA, Thanh NTK. Elucidating the morphological and structural evolution of iron oxide nanoparticles formed by sodium carbonate in aqueous medium. Journal of Materials Chemistry. 2012;22:12498-506.

[2] Ahmed N, Michelin-Jamois M, Fessi H, Elaissari A. Modified double emulsion process as a new route to prepare submicron biodegradable magnetic/polycaprolactone particles for in vivo theranostics. Soft Matter. 2012;8:2554-64.

[3] Ciobanu CS, Iconaru SL, Gyorgy E, Radu M, Costache M, Dinischiotu A, et al. Biomedical properties and preparation of iron oxide-dextran nanostructures by MAPLE technique. Chemistry Central Journal. 2012;6:17.

[4] Als-Nielsen J, McMorrow D. Elements of modern X-ray physics: John Wiley & Sons; 2011.

[5] Bowen DK, Tanner BK. High resolution X-ray diffractometry and topography: CRC press; 2005.

[6] Kaszkur Z. Nanopowder diffraction analysis beyond the Bragg law applied to palladium. Journal of applied crystallography. 2000;33:87-94.

[7] Azaroff LV, Buerger MJ. The powder method in X-ray crystallography. 1953.

[8] Bunn CW. Chemical crystallography: an introduction to optical and x-ray methods: Clerendon Press; 1961.

[9] Sun Y, Xia Y. Shape-controlled synthesis of gold and silver nanoparticles. Science. 2002;298:2176-9.

[10] Theivasanthi T, Alagar M. X-ray diffraction studies of copper nanopowder. arXiv preprint arXiv:10036068. 2010.

[11] Theivasanthi T, Alagar M. Electrolytic synthesis and characterizations of silver nanopowder. arXiv preprint arXiv:11110260. 2011.

[12] Theivasanthi T, Alagar M. An insight analysis of nano sized powder of jackfruit seed. arXiv preprint arXiv:11100346. 2011.

[13] Subbaiah YV, Prathap P, Reddy KR. Structural, electrical and optical properties of ZnS films deposited by close-spaced evaporation. Applied Surface Science. 2006;253:2409-15.

[14] Antony J, Nutting J, Baer DR, Meyer D, Sharma A, Qiang Y. Size-dependent specific surface area of nanoporous film assembled by core-shell iron nanoclusters. Journal of Nanomaterials. 2006;2006.

[15] Goldstein JI, Newbury DE, Echlin P, Joy DC, Lyman CE, Lifshin E, et al. Special Topics in Scanning Electron Microscopy. Scanning electron microscopy and x-ray microanalysis: Springer; 2003. p. 195-270.

[16] Egerton RF. Physical principles of electron microscopy: Springer; 2005.

[17] Lyman CE, Newbury DE, Goldstein J, Williams DB, Romig Jr AD, Armstrong J, et al. Scanning electron microscopy, X-ray microanalysis, and analytical electron microscopy: a laboratory workbook: Springer Science & Business Media; 2012.

[18] Businova P, Chomoucka J, Prasek J, Hrdy R, Drbohlavova J, Sedlacek P, et al. Polymer coated iron oxide magnetic nanoparticles: preparation and characterization. Nanocon. 2011;9:21-3.

[19] Hong R, Li J, Chen L, Liu D, Li H, Zheng Y, et al. Synthesis, surface modification and photocatalytic property of ZnO nanoparticles. Powder Technology. 2009;189:426-32.

[20] Bergman L, McHale JL. Handbook of luminescent semiconductor materials: CRC Press; 2011.

Chapter 3
Effect of Annealing Temperature on α-Fe_2O_3 Nanostructures and Optical Properties

Chapter-3

Effect of annealing temperature on structural, optical and photocatalytic properties of α-Fe_2O_3 nanostructures

In the present work α-Fe_2O_3 nanostructures have been synthesized by chemical co-precipitation followed by annealing at 500 and 600°C for 3 h. Nanoparticle powders were characterized by X-ray diffraction (XRD), scanning electron microscope (SEM), energy dispersive X-ray spectroscopy (EDX), Fourier transform infra-red spectroscopy (FTIR), particle size distribution, Brunauer Emmett Teller analysis (BET), photoluminescence and UV-Visible spectroscopy. XRD confirmed the formation of crystalline α-Fe_2O_3 nanoparticles while SEM confirmed the formation of rice grain and spherical shapeα-Fe_2O_3nanostructures at 500 and 600 °C. From EDX and FTIR results formation of α-Fe_2O_3 is further established. BET analysis confirmed the mesoporous behavior of nanoparticles. UV-Visible and photoluminescence spectra have been used to determine band gap and photo-oxidation behavior of dye methylene blue. Both Fe_2O_3-500 and Fe_2O_3-600 nanostructures exhibit exceptionally high photocatalytic activity however the same is higher for Fe_2O_3-500 than that of Fe_2O_3-600 for degradation of methylene blue (Meb).

3.1. Introduction:

Nowadays, water pollution has become the major threat to the living organism. Large amount of dangerous waste effluents reaches from industrial sectors, due to speedy industrialization in different fields. Since the natural degradation and conventional treatments are not much effective and not environmentally benign, these noxious waste pose solemn ecological problems. Although the chemical industries played a momentous character in development of human civilization, but simultaneously they release large quantities of chemicals, particularly persistent organic pollutants, causing potential harm to many ecosystems. Among all chemicals, dyes, surfactants, chloro-organics etc are some notable class of aquatic hazards responsible for environmental pollution.

The textile industries consume enormous volumes of water in dissimilar processes and release large amount of textile wastewater, which is heavily charged with unconsumed organic chemicals including dyes which are well-known carcinogenic organic substances. The dyes when discharged into environment cause serious ill effect on the aquatic life, surrounding ecosystem and human being [1]. Reductive enzymes in the liver can catalyze azo linkage via reductive cleavage to produce aromatic amines and thus can lead to intestinal cancer [2, 3]. Exclusion of dyes and other commercial colorants from continual waste water effluents of textile, paper mills and other colorant manufactures is now the subject of considerable concern of environmental remediation. Many N- containing dyes undergo ordinary reductive anaerobic degradation to produce potentially carcinogenic aromatic amines [4]. Several physical treatment methods, such as activated carbon adsorption, flocculation, reverse osmosis, chemical oxidation and biological treatments have been used and demonstrated the clean-up process for water treatment. However, the above

techniques are either slow or non-destructive, since they just transfer the organic compounds from water to other phase, thus causing secondary pollution.

Advanced oxidation processes (AOPs) is an effective route for degradation of organic pollutants. Among the AOPs, heterogeneous photocatalysis has emerged as a more efficient technique, for destruction of most of the organic pollutants. Direct photo catalytic reaction by using semiconductor powders has been shown to effectively degrade numerous kinds of pollutants together with dye pollutants and in many cases even completely mineralize the compounds [5]. Several semiconductors, such as TiO_2, ZnO, Fe_2O_3, ZrO_2, WO_3, SnO_2, CdS, GaP, ZnS etc have been used as heterogeneous photocatalyst and shown its efficiency in degrading a wide range of organics into readily biodegradable molecules and eventually mineralized those to harmless products.

The ideal photocatalyst should be biologically and chemically inert, stable toward photocorrosion, suitable towards visible or proximate UV light, cost effective and nontoxic. In this regard, TiO_2 is a suitable photocatalyst, under the photon energy of 300 nm $< \lambda <$ 390 nm, hence has wide-ranging application in photocatalytic treatment of water. Most investigations of the photo-assisted decomposition of dyes used TiO_2 as a model photo catalyst owing to its high photocatalytic efficiency, chemical and biological stability. Several reports have been available on TiO_2 and TiO_2 based mixed oxide photocatalysis for degradation of a number of organic pollutants in water. But TiO_2 photocatalysis requires ultra-violet light to cause charge separation on the semiconductor surface. α-Fe_2O_3 is a low cost, abundant, stable, nontoxic, easily synthesisable and widely used photocatalyst with band gap ~ 2.2 eV (visible region absorption edge at ~ 565 nm) [6-8]. Though α-Fe_2O_3 is an efficient photocatalyst due to its high absorptive efficiency in the red light of visible region,

which contributes around 43 % of solar radiation [9], however charge carriers (electron-holes) recombination is a serious limitation with α-Fe_2O_3 photocatalyst.

Nanoscale materials have distinctive properties differing from their molecular and bulk forms, such as quantum confinement, enabling superior catalytic performance including the high selectivity and high reactivity [10]. The use of nanocrystalline metal oxides in the photocatalytic oxidation of organic molecules represents a promising remediation strategy for wastewater systems. It has been shown that the photocatalytic efficiency of semiconductor nanoparticles is greatly influenced by size, shape and crystallinity in the photocatalytic reactions [11, 12]. Further, the architectural dependence of photocatalytic activity has the vast scope and still open to be explore a lot because different shape α-Fe_2O_3 nanostructures can be fabricated via wet chemical synthetic routes like sol-gel process [13], hydrothermal [14-16], chemical precipitation [17] and by many other methods [18-20]. Jiao and co-workers synthesised α-Fe_2O_3 nanourichin in a simple and facile manner in aqueous phase and shape dependent photocatalytic activity has been evaluated for degradation of various dyes like Congo red, Eosin and Methylene blue [21]. Further, it has been reported that the annealing temperature play a critical role on absorption properties, thus affecting phtocatalytic properties of semiconducting nanostructures [22].

In this study, α-Fe_2O_3 nanostructures have been prepared via co-precipitation method in aqueous phase and effect of annealing temperature on size, shape and optical properties, thus on photocataltytic degradation of dye Methylene blue have been investigation.

3.2. Experimental:

3.2.1. Materials:

All chemicals used in this work were analytical grade and used without further purification. Ferric chloride hexa-hydrate ($FeCl_3 \cdot 6H_2O$), ferrous sulphate hepta-

hydrate ($FeSO_4 \cdot 7H_2O$), ammonium hydroxide (NH_4OH, 26% of ammonia) and methylene blue (MB) were purchased from Merck India. Double distilled water was used as solvent. All the glasswares were cleaned by concentrated acid. The dried glasswares were used in all the experiments.

3.2.2. Synthesis of Fe_2O_3 nanostructures:

In this study α-Fe_2O_3 nanostructures have been prepared by co-precipitation method using Fe^{2+} and Fe^{3+} ions. Aqueous solutions Fe^{2+} and Fe^{3+} were prepared by dissolving ferric chloride and ferrous sulphate in double distilled water. The solutions Fe^{2+} and Fe^{3+}ions were mixed in 2:1 molar ratio and heated at 90°C for 10 minutes. After heating, the solution was precipitated by adding ammonia solution with continuous stirring on the magnetic stirrer at 90 °C until pH reached to 11. The reaction mixture was again heated at 90 °C for 2 h. Black colored particles of iron oxide were precipitated. These particles were separated from the solution using a strong magnet and washed many times with double distilled water. The powder was then dried in oven at 100 °C for overnight. The overall reaction can be written as

$$Fe^{2+} + 2Fe^{3+} + 8OH^- \rightarrow Fe_2O_3 + 4H_2O$$

The products were annealed at 500˚C and 600 °C for 3 h to get Fe_2O_3-500 and Fe_2O_3-600 samples.

3.2.3. Characterization:

The XRD patterns of as prepared Fe_2O_3 nanoparticles were recorded on Pananalytical's X'Pert Pro X-ray diffractometer in the 2θ range 10 to 80˚ with step size of 0.025˚. Scanning electron microscope (SEM) images of the products were observed on JEOL 6490 LB equipment. The SEM micrographs were obtained at an operating voltage of 3 kV. FTIR spectra of as prepared Fe_2O_3-500 and Fe_2O_3-600 samples were characterized by the Perkin Elmer Spectrum RXI. The particles size

distribution of the materials has been observed on Zetasizer Nano Series ZS 90. Brunauer-Emmett-Teller (BET) analysis of all the materials was done on BELSORP MINI (II) equipment. Photoluminescence spectral studies of the materials have been carried out on spectrofluorometer (Perkin Elmer LS 55) at excitation wavelength 425 nm. UV-Visible spectra were recorded in absorption mode on Cary 100 spectrophotometer in the wavelength region 200-800 nm.

3.3. Photocatalytic activity:

The photocatalytic activity of as prepared Fe_2O_3-500 and Fe_2O_3-600 materials was determined by photodegradation of dye methylene blue (Meb) under visible light exposure using Xe lamp (1000 W). 100 mg amount of Fe_2O_3 was first dispersed in 100 mL of 50 ppm Meb solution and stirred for 30 minutes in the dark condition in order to achieve the adsorption equilibrium. The solution was irradiated by visible light in a photocatalytic chamber. During irradiation, solution was agitated using a magnetic stirrer and air was bubbled into the reaction medium to provide a constant supply of oxygen. After desired time interval, an aliquot of solution was isolated, centrifuged and its absorbance was measured on UV-Visible spectrophotometer to calculate the percentage degradation. The same procedure was repeated for Fe_2O_3-600 nanoparticles also. The photocatalytic degradation efficiency was calculated using the following equation:

$$(\%)\ \text{degradation} = ((A_0 - A)/A_0) \times 100$$

Where A_0 represents the initial absorbance of the dye solution and A; the absorbance after irradiation at particular time.

3.4. Results and discussions:

Crystal structure, phase and purity of as synthesized materials were determined using X-ray diffraction (XRD) analysis. All the diffraction peaks in the

XRD pattern of as synthesized materials Fe_2O_3-500 and Fe_2O_3-600, obtained by annealing of precipitates at 500 and 600 ºC are shown in Figure 3.1 a & b. In the XRD pattern, peaks correspond to (012), (104), (110), (113), (124), (116), (214), (300) and (208) lines are well matched with JCPDS file no 33-0664, indicating that both the samples are phase pure α-Fe_2O_3. Furthermore, it is obvious from the diffraction pattern that the XRD peaks are intense and broad; indicating good crystalline and small size α-Fe_2O_3 materials are formed. The Scherer's formula (Equation 1) has been used to evaluate the crystallites size of as synthesized materials using (110) reflection peaks of XRD pattern of Fe_2O_3-500 and Fe_2O_3-600 [23].

$$d = \frac{0.9\,\lambda}{\beta\,cos} \qquad (1)$$

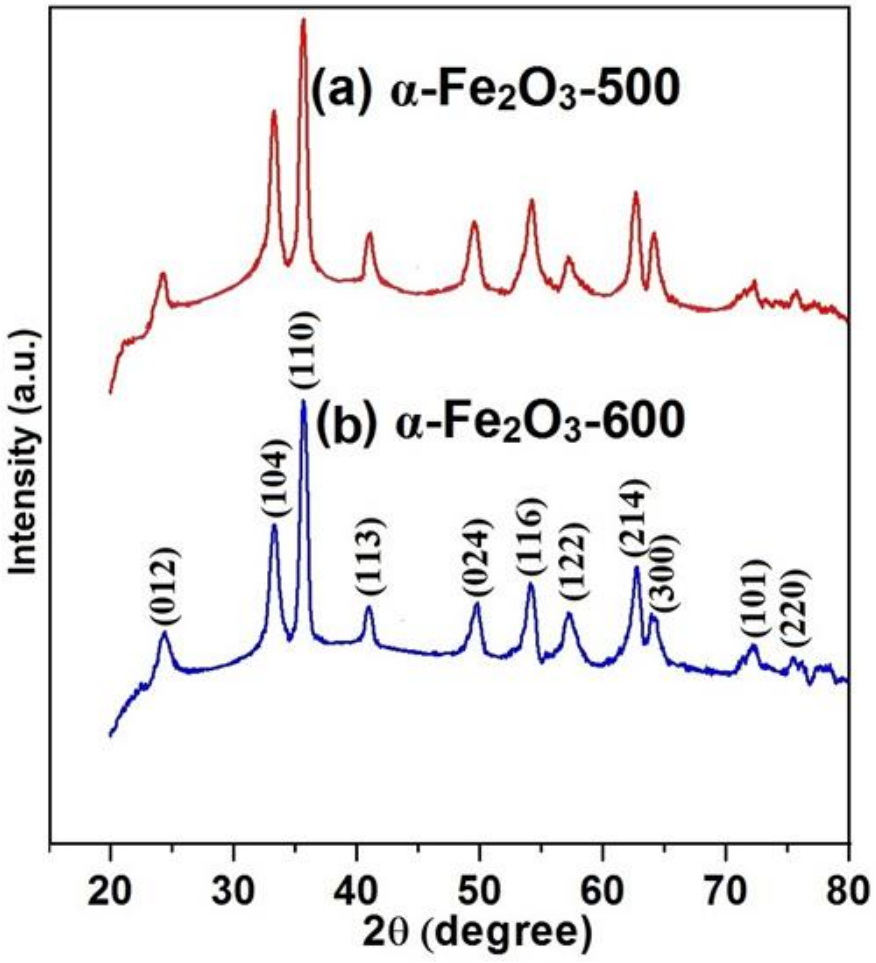

Figure 3.1: XRD spectra of (a) α-Fe_2O_3-500 (b) α-Fe_2O_3-600

Where *d* is the crystallites size (in nm), λ the wavelength (in nm), β is the full width at half maxima (FWHM) and θ is the Bragg's diffraction angle. The average crystallites size of the materials Fe_2O_3-500 and Fe_2O_3-600 has been derived as 51 and 38 nm respectively, using above equation.

The Brunauer-Emmett-Teller (BET) analysis was used to determine surface area of as synthesized Fe_2O_3-500 and Fe_2O_3-600 materials. The surface area (a_p) of Fe_2O_3-500, and Fe_2O_3-600 NPs has been found to be 26.881 and 16.372 m^2g^{-1} respectively. The pore volume (V_p) of Fe_2O_3-500, and Fe_2O_3-600 NPs has been found to be 0.2652 and 02105 cm^3g^{-1} respectively. From above data it is obvious that as the surface area decreases, corresponding pore volume decreases. Figure 3.2 shows the nitrogen adsorption-desorption isotherm plots for Fe_2O_3-500 and Fe_2O_3-600 materials, which are typical type IV curves along with H4 hysteresis curve according to the IUPAC classification and shows the presence of mesoporous phases [24].

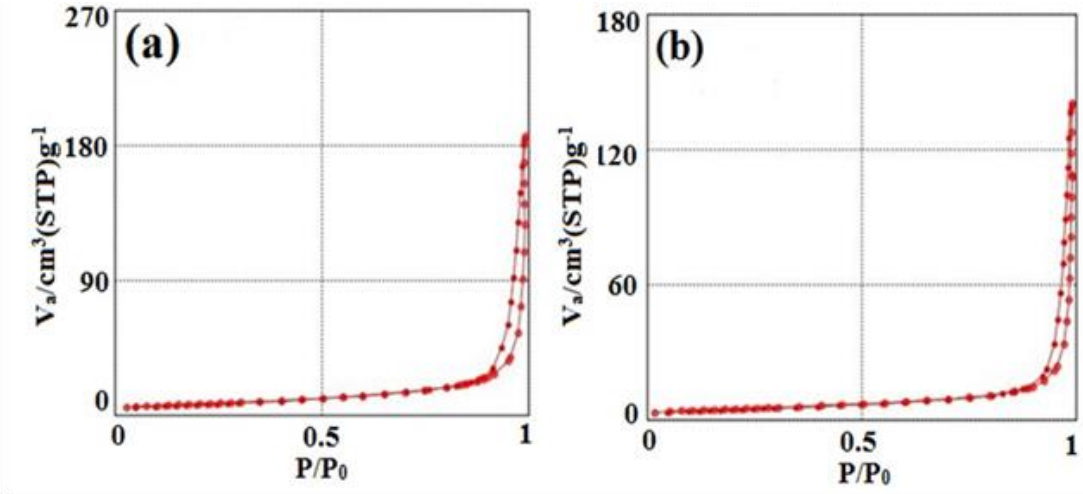

Figure 3.2: BET Plot of (a) α-Fe_2O_3-500 (b) α-Fe_2O_3-600

Structural, morphological and compositional investigations of as synthesized products were examined using SEM and EDX analysis depicted in Figure 3.3. In the SEM micrograph, approximately 45 nm long and 9 nm wide rice grain structured Fe_2O_3-500 particles are observed (Figure 3.3 a). Interestingly, on increasing the

annealing temperature, almost spherical shape Fe_2O_3-600 particles with diameter about 50 nm are formed (Figure 3.3 b). Corresponding EDX patterns of the samples Fe_2O_3-500 and Fe_2O_3-600 (Figure 3.3 c & d) show that Fe:O ratio in both the samples is almost 2:3, suggesting that the materials are composed of Fe and O elements in 2:3 ratio.

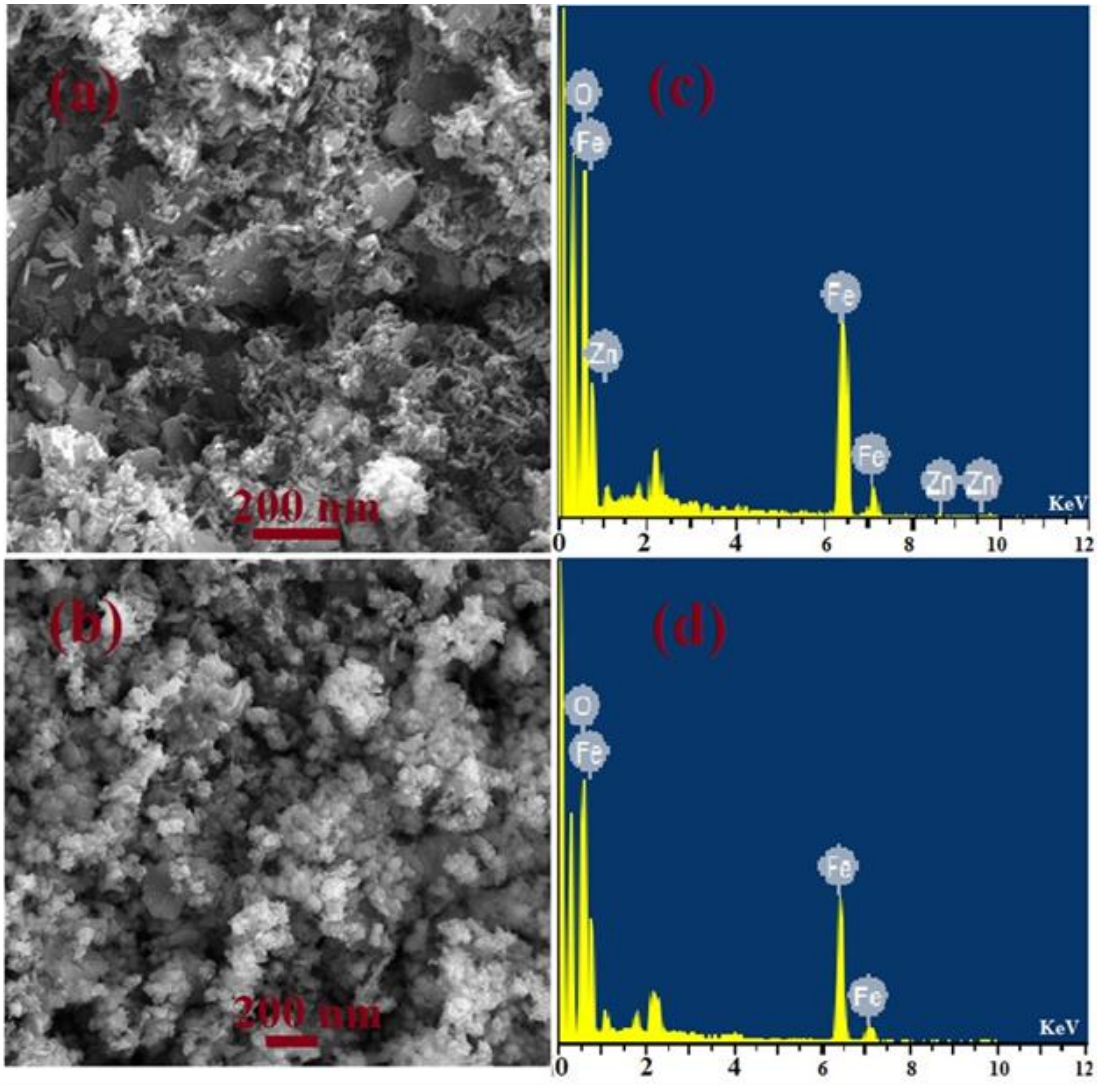

Figure 3.3: SEM Image of (a) α-Fe_2O_3-500 (b) α-Fe_2O_3-600 (c) EDX spectra of α-Fe_2O_3-500 (d) α-Fe_2O_3-600

The particle size distribution of Fe_2O_3 -500 and Fe_2O_3 -600 materials have been studied on Zetasizer and the results are shown in Figure 3.4. For particles size distribution study, the materials were mixed in DMSO and sonicated. From particle

size distribution curves, it is obvious that size distribution of both samples is wide. The size of particles varies from 10 to 40 nm with maxima at 20 nm and from 30 to 60 nm with maxima at 46 nm for the samples Fe_2O_3-500 and Fe_2O_3 -600 respectively. The results are in agreement of sizes of Fe_2O_3-500, Fe_2O_3-600 materials determined from XRD and SEM analysis.

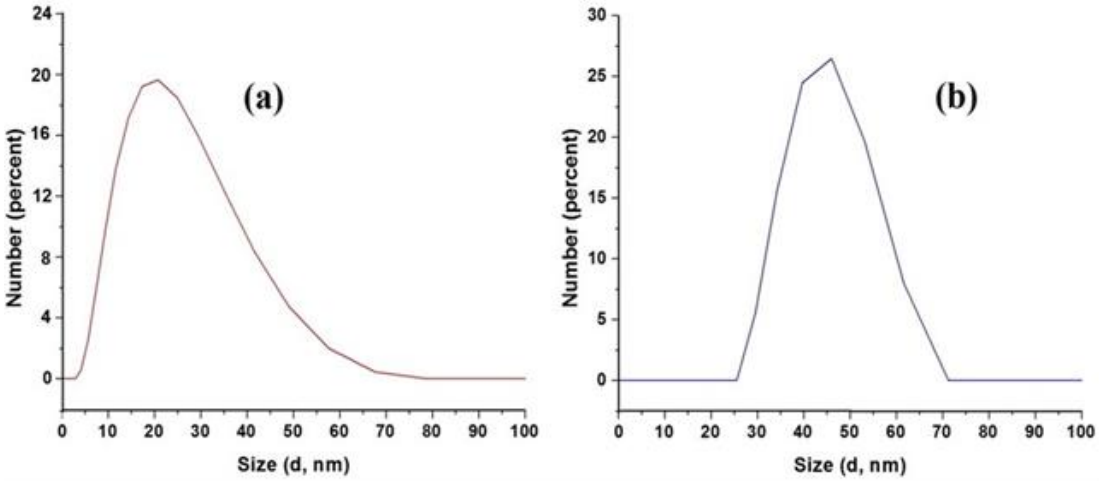

Figure 3.4: Particle size distribution graph of (a) α-Fe_2O_3-500 (b) α-Fe_2O_3-600

Figure 3.5 shows the FTIR spectra for Fe_2O_3-500 and Fe_3O_4-600 nanoparticle. In the FTIR spectra of both samples, the strong peaks located at 536 and 464 cm^{-1}, are characteristic of Fe-O vibration modes of α-Fe_2O_3 and can be referred to the A_2u/Eu and Eu band, respectively. The peak at 535.5-535.7 cm^{-1} is due to overlap of A_2u and Eu vibrations, with the dipolar moments parallel to and perpendicular to the c axis, respectively while the band at 464 cm^{-1} is owing to the Eu vibration, which lies perpendicular to the c axis [25].The observed peak at 1637-1638 cm^{-1} in the FTIR spectrum of Fe_2O_3-500 andFe_2O_3-600 is due to N-H bending vibration of NH_2 group. The broad peak in case of Fe_2O_3-500 at 3422.7 cm^{-1} is due to overlapped O-H and N-H stretching vibrations of adsorbed H_2O and NH_2. This band is not visible in spectrum of Fe_2O_3-600 probably due to higher annealing temperature.

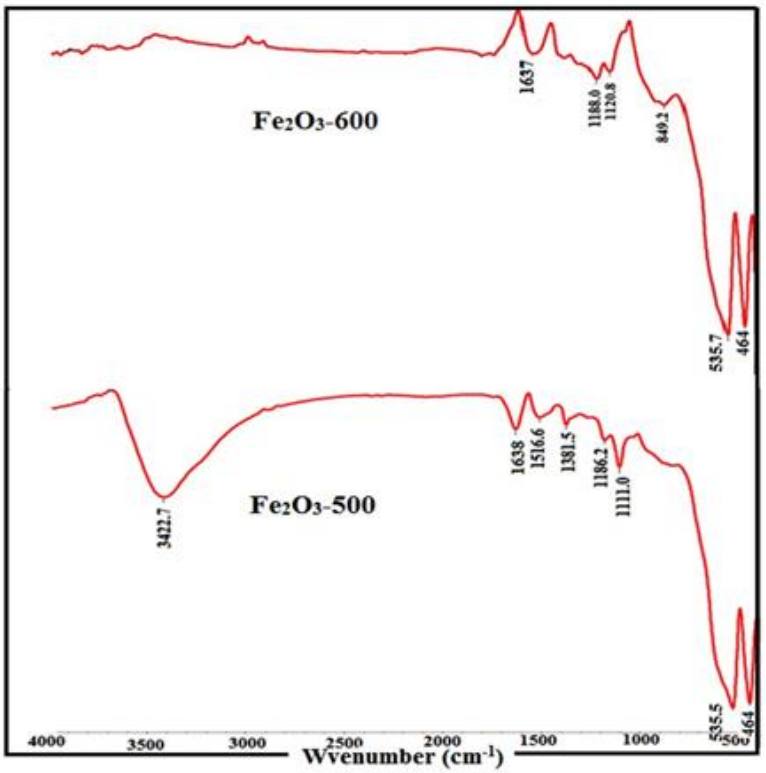

Figure 3.5: FTIR spectra of (a) α-Fe_2O_3-500 (b) α-Fe_2O_3-600

In the condensed phase, Fe^{3+} exhibits three types of electronic transitions, first due to ligand field transition, second due to ligand metal charge transfer (LMCT from O^{2-} to Fe^{3+}) and third correspond to paired excitation of magnetically coupled Fe^{3+} ions occupying the adjacent sites in the crystals [26]. The UV-Vis absorption spectra of as-synthesised hematite α-Fe_2O_3-500 and α-Fe_2O_3-600 NPs are shown in Figure 6. Absorption peak at around 377, 397 and 450 nm are due to $^6A_1 \rightarrow {}^4T_1({}^4P)$, $^6A_1 \rightarrow {}^4E({}^4D)$ and $^6A_1 \rightarrow {}^4E$, $^4A_1({}^4G)$ transitions respectively for both the samples Fe_2O_3-500 and Fe_2O_3-600. Moreover, a characteristic feature at 546 nm has been assigned to $^6A_1 + {}^6A_1 \rightarrow {}^4T_1({}^4G) + {}^4T_1({}^4G)$ transition of Fe-Fe pair in the two samples[27]. Direct band gap energy of materials was calculated from the Tauc relation:

$$(\varepsilon h\nu)^2 = P(Eg - h\nu) \quad (1)$$

Where ε is the molar extinction coefficient, h is plank constant, ν is frequency of light, Eg is the band gap energy and P is the arbitrary constant. The linear part of the $(\varepsilon h\nu)^2$

verses *hv* graph (Figure 3.6) was used to calculate the band gap values. The intercept of tangent at the x axis gives *Eg* value. The *Eg* values for the materials Fe_2O_3 -500 and Fe_2O_3 600 have been found as 2.44 and 2.58 eV respectively using above relation (Figure 3.7).

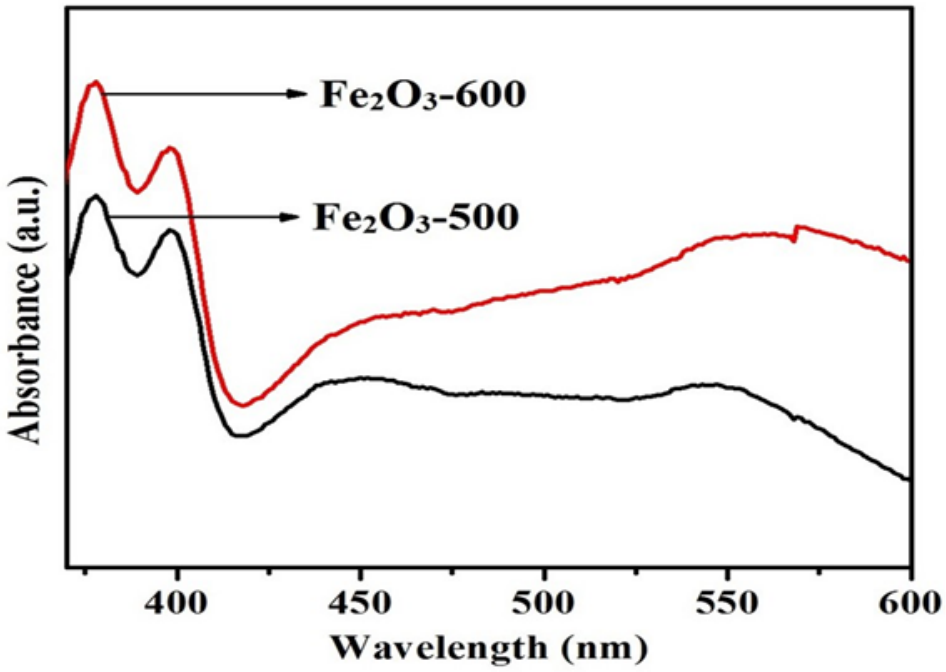

Figure 3.6: UV-Visible spectra of (a) α-Fe_2O_3-500 (b) α-Fe_2O_3-600

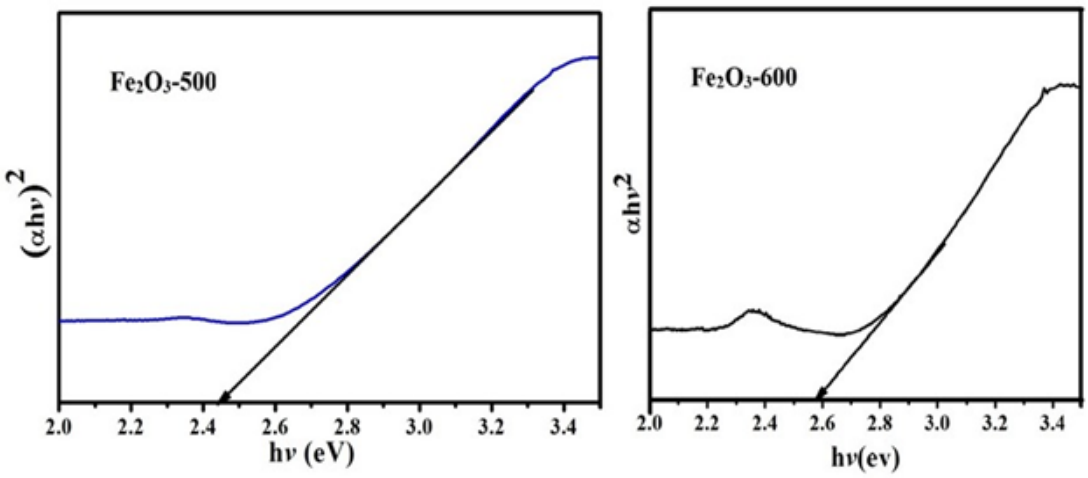

Figure 3.7: Band gap of (a) α-Fe_2O_3-500 (b) α-Fe_2O_3-600

Contaminants photodegradation capability of the above synthesized Fe_2O_3-500 and Fe_2O_3-600 photocatalysts was evaluated by recording photodegradation behavior

of dye methylene blue (Meb) under visible light irradiation. In the present study, continuous air bubbling was done to ensure the presence of O_2, which was used as oxidizing agent. Figure 3.8 shows the variation in the UV-visible absorbance spectra of Meb solution (50 mg/L) with different irradiation time in presence of Fe_2O_3-500 and Fe_2O_3-600 nanostructures.

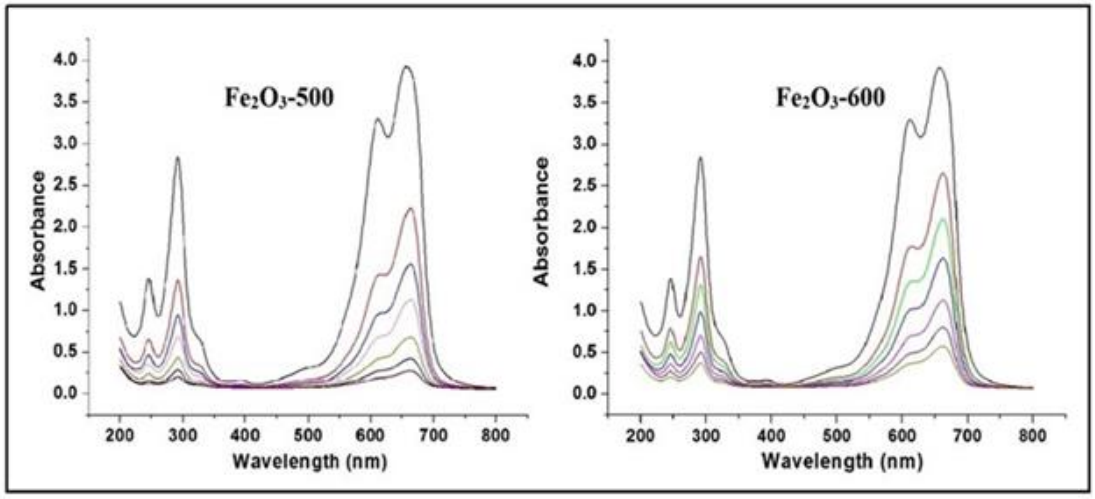

Figure 3.8: Photodegradation behaviour of (a) α-Fe_2O_3-500 (b) α-Fe_2O_3-600

Figure 3.9 shows the extent of degradation of Meb in presence of Fe_2O_3-500 and Fe_2O_3-600 NPs under visible light irradiation for 60 minutes time. It is evident from the spectra that 92.8 and 85% degradation of Meb takes place in presence of Fe_2O_3-500 and Fe_2O_3-600respectively under visible light irradiation for 60 minutes of time. The results show that both the photocatalysts are effective for degradation of Meb, however photodegradation capacity of Fe_2O_3-500 is the higher than Fe_2O_3-600. Applying the Langmuir Hinshelwood model for determining the oxidation rate of the photocatalysis of dye Meb:

$$Rate(r) = -\frac{dC}{dt} = -\frac{k'KC}{1} + KC \qquad (2)$$

Where *k* is the rate constant (mg/L min^{-1}), *C* is the concentration of dye, *K* is the adsorption constant of the dye (L/mg), and *t* is the illumination time (minutes). Integrating equation (2) the rate law can be rearranged as:

$$ln\,{}^{C}/_{C_0} = -kt \qquad (3)$$

Here C_0 is the initial concentration of dye solution, *C* the concentration after time *t* and *k* is the rate constant. A graph has been plotted between lnC/C_0 versus t (Figure 3.10) where rate constant k can be determined by the slope of fitting curve. From the above graph, the rate constant values for Fe_2O_3-500 and Fe_2O_3-600 catalysts have been determined as 0.042, and 0.031 min^{-1} respectively. The results demonstrate that both Fe_2O_3-500 and Fe_2O_3-600 good photocatalysts, however phtocatalytic activity of Fe_2O_3-500 is higher than Fe_2O_3-600 for degradation of dye Meb.

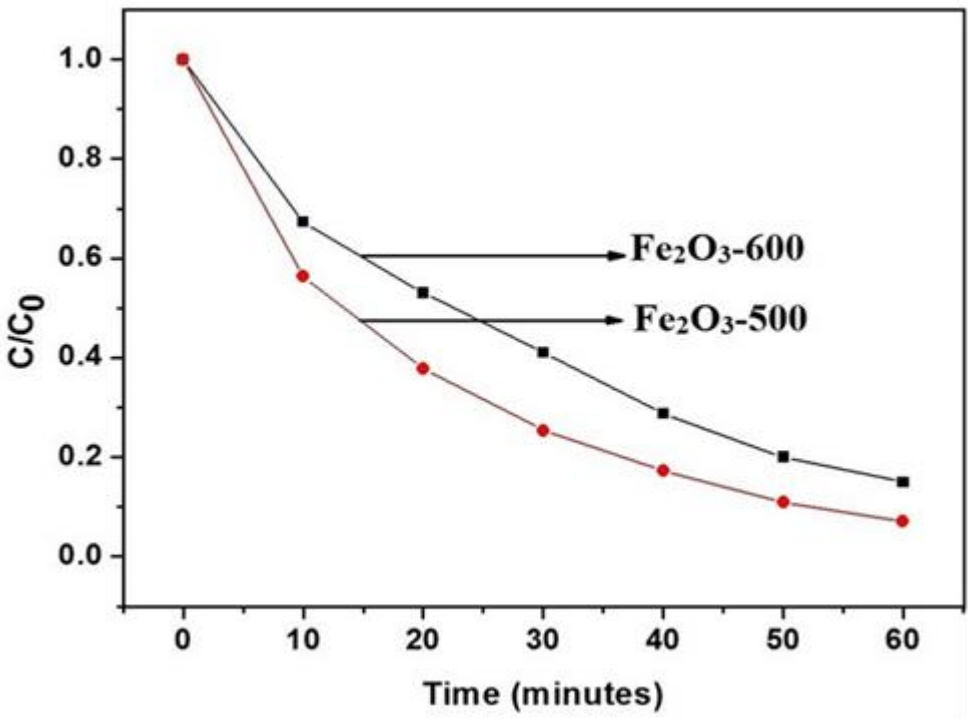

Figure 3.9: Extent degradation of (a) α-Fe_2O_3-500 (b) α-Fe_2O_3-600

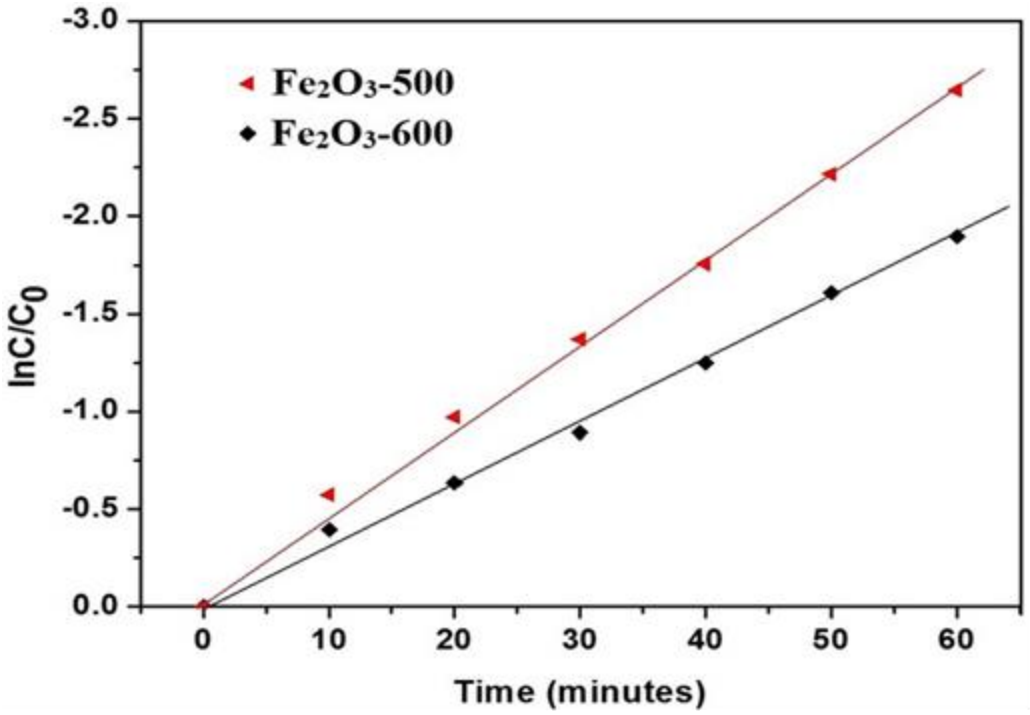

Figure 3.10: Kinetics of (a) α-Fe_2O_3-500 (b) α-Fe_2O_3-600

It is known that the photocatalytic efficiency of semiconductor photocatalysts depends on various properties like band gap, phase/crystal structure, particle size, shape, surface area, surface defects and presence of bound molecules on the surface [21, 28]. Surface area of the catalysts has direct correlation with their photocatalytic activity. If surface area is higher, photocatalytic activity will be larger because then greater number of active sites will be available to accommodate larger number of substrate molecules. In this investigation the photocatalytic activity of Fe_2O_3-500 is higher than Fe_2O_3-600 because the surface area of former is higher than that of later.

A major limitation of achieving high photocatalytic activity is the fast recombination of charge carriers (electron-holes) which are generated by illumination of photocatalyst by electromagnetic radiation. Retardation of recombination of electron-hole is the prime requirement for a photocatalysts in photochemical reactions. Since photoluminescence emission results due to radiative recombination of electrons and holes, it can be used to monitor the recombination behavior, and thus

availability of these charge carriers in photochemical reactions using semiconductor photocatalysts [29]. Electron-hole recombination process has been studied by recording PL spectra of the materials Fe_2O_3-500 and Fe_2O_3-600. Figure 3.11 shows the PL spectra of Fe_2O_3-500 and Fe_2O_3-600 materials at excitation wavelength 425 nm. In the PL spectra of both Fe_2O_3-500 and Fe_2O_3-600 materials, the peak at 654 nm is attributed to $^6A_1 \rightarrow {}^4T_1(^4G)$ ligand field transition of Fe^{3+} [30]. The emission intensity of Fe_2O_3-500 is lower than that of Fe_2O_3-600 indicating that recombination rate of electron-holes in case of Fe_2O_3-500 is lower than that of Fe_2O_3-600. This leads to higher photocatalytic activity of Fe_2O_3-500 than Fe_2O_3-600 as observed in Figure 3.11. The probable reason for decrease of PL intensity of Fe_2O_3-500 is availability of shape dependent (rice grain shape Fe_2O_3-500) defect states in the forbidden gap, giving rise to relaxation of excited electrons to lower levels in the band gap.

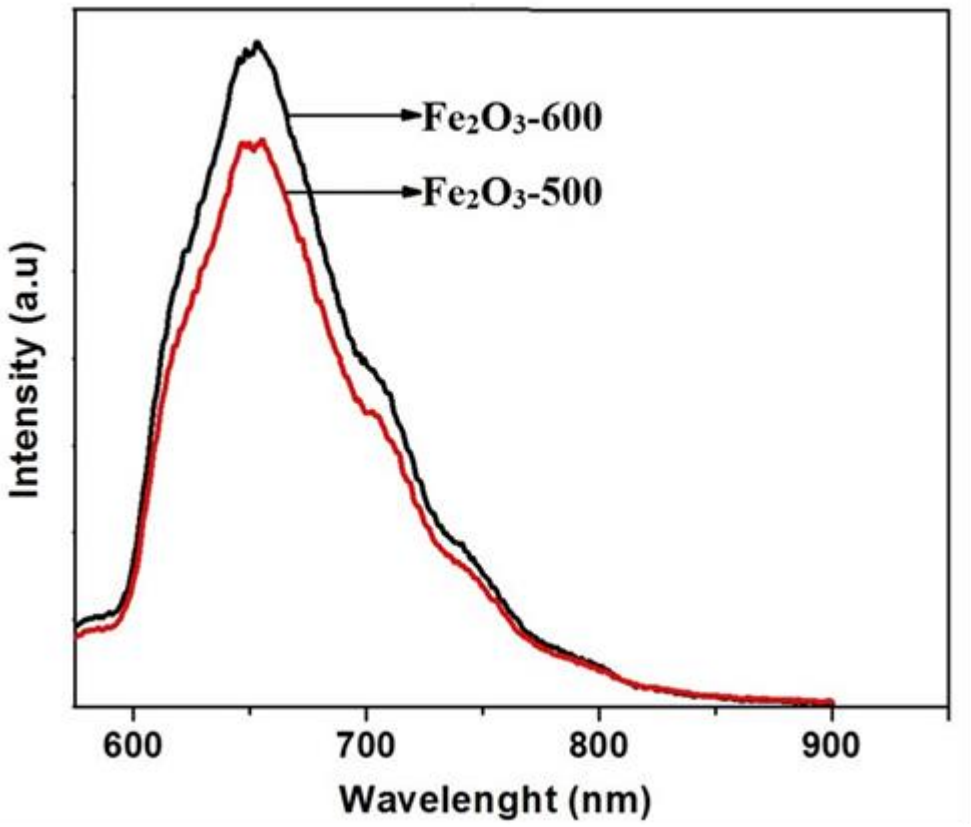

Figure 3.11: PL spectra of (a) α-Fe_2O_3-500 (b) α-Fe_2O_3-600

Conclusively, on the basis on the basis of above results and analysis it can stated that the photocatalytic activity of the samples Fe_2O_3-500 and Fe_2O_3-600 achieved due to large surface area, good optical absorbance in the visible region and efficient separation of electron-holes. On the basis of above facts a possible mechanism of photocatalytic degradation process of dye Meb is shown schematically in Figure 3.12. Due to high surface area, and thus availability of greater number of active sites, the samples accommodated larger number of substrate molecules. On visible light illumination, electrons in the valance band of α-Fe_2O_3 are excited to conduction band leaving holes in valance band. The hydroxyl groups present at the surface of photocatalysts react with holes to produce hydroxyl radicals while dissolved oxygen reacts with photogeneated electrons yielding superoxide and consequently hydroperoxide radicals, followed by hydrogen peroxide. These products react with dye Meb, ultimately converting them to carbon dioxide and water molecules. The reaction steps taking place for photocatalytic degradation of Meb can be sum up as bellow [20].

$$\alpha\text{-}Fe_2O_3\text{-}500\ /\alpha\text{-}Fe_2O_3\text{-}600 + h\nu \rightarrow \alpha\text{-}Fe_2O_3\text{-}500\ /\alpha\text{-}Fe_2O_3\text{-}600\ (e^- - h^+) \quad (4)$$

$$h^+ + H_2O \rightarrow {}^{\cdot}OH + H^+ \quad (5)$$

$$e^- + O_2 \rightarrow O_2^- \rightarrow HO_2^{\cdot} \quad (6)$$

$$O_2^- + Meb \rightarrow Meb^{+\cdot} - O_2 \quad (7)$$

$${}^{\cdot}OH + Meb^{+\cdot} \rightarrow CO_2 + H_2O \quad (8)$$

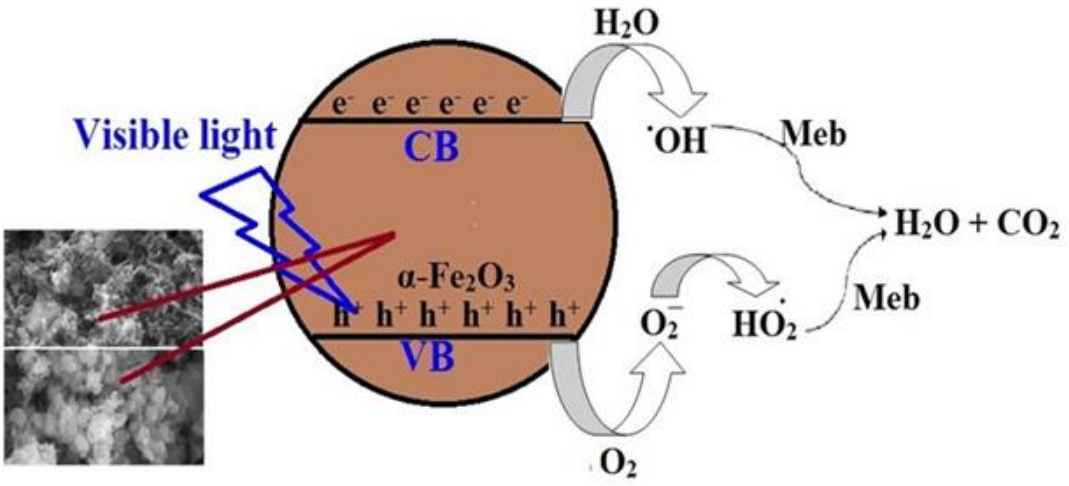

Figure 3.12: Schematic representation of photodegadation (a) α-Fe_2O_3-500 (b) α-Fe_2O_3-600

3.5. Conclusion:

In summary, α-Fe_2O_3-500 and α-Fe_2O_3-600 structures have successively been synthesized by chemical co-precipitation followed by annealing at 500 °C, 600 °C. XRD and SEM studies revealed formation of rice grain like α-Fe_2O_3-500 (45 nm long and 9 nm diameter) and spherical α-Fe_2O_3-600 (50 nm diameter) nanocrystals. The photocatalytic activity results revealed that the α-Fe_2O_3-500 and α-Fe_2O_3-600 are effective photocatalysts, however α-Fe_2O_3-500 has the higher photocatalytic activity than α-Fe_2O_3-600 for degradation of Meb. The surface area (a_p) of Fe_2O_3-500, and Fe_2O_3-600 NPs has been found to be 26.881, 16.372 m^2g^{-1} respectively and the pore volume (V_p) of Fe_2O_3-500, and Fe_2O_3-600 NPs has been found to be 0.2652, 02105 cm^3g^{-1} respectively. From above data it is obvious that as the surface area decreases, corresponding pore volume decreases. From UV-Visible absorption spectra band gap values for the materials Fe_2O_3 -500 and Fe_2O_3 600 have been found as 2.44 and 2.61 eV respectively. In the PL spectra of Fe_2O_3-500 and Fe_2O_3-600 materials, the peak at 654 nm is due to $^6A_1 \rightarrow {}^4T_1({}^4G)$ ligand field transition of Fe^{3+}. The emission peak of

Fe_2O_3-500 is lower than Fe_2O_3-600 due to availability of shape dependent (rice grain shape Fe_2O_3-500) defect states in the forbidden gap, giving rise to relaxation of excited electrons to lower levels in the band gap thus lowering the recombination rate of electron-holes in case of Fe_2O_3-500 than that of Fe_2O_3-600. This leads to higher photocatalytic activity of Fe_2O_3-500 than that of Fe_2O_3-600. The photocatalytic activity of Fe_2O_3-500 is higher than Fe_2O_3-600 because the surface area of former is higher than the later. Summarily, photocatalytic activity of the samples Fe_2O_3-500 and Fe_2O_3-600 achieved due to large surface area, good optical absorbance in the visible region and efficient separation of electron-holes.

3.6. References:

[1] Qu X, Brame J, Li Q, Alvarez PJ. Nanotechnology for a safe and sustainable water supply: enabling integrated water treatment and reuse. Accounts of chemical research. 2012;46:834-43.

[2] Chung K-T, Stevens SE, Cerniglia CE. The reduction of azo dyes by the intestinal microflora. Critical reviews in microbiology. 1992;18:175-90.

[3] Chung KT. The significance of azo-reduction in the mutagenesis and carcinogenesis of azo dyes. Mutation Research/Reviews in Genetic Toxicology. 1983;114:269-81.

[4] Brown D, Hamburger B. The degradation of dyestuffs: Part III-Investigations of their ultimate degradability. Chemosphere. 1987;16:1539-53.

[5] Teja AS, Koh PY. Synthesis, properties, and applications of magnetic iron oxide nanoparticles. Progress in crystal growth and characterization of materials. 2009;55:22-45.

[6] Kim JY, Youn DH, Kim JH, Kim HG, Lee JS. Nanostructure-preserved hematite thin film for efficient solar water splitting. ACS applied materials & interfaces. 2015;7:14123-9.

[7] Baumanis C, Bloh JZ, Dillert R, Bahnemann DW. Hematite photocatalysis: Dechlorination of 2, 6-dichloroindophenol and oxidation of water. The Journal of Physical Chemistry C. 2011;115:25442-50.

[8] Wang X, Peng KQ, Hu Y, Zhang FQ, Hu B, Li L, et al. Silicon/hematite core/shell nanowire array decorated with gold nanoparticles for unbiased solar water oxidation. Nano letters. 2013;14:18-23.

[9] Pradhan GK, Padhi DK, Parida K. Fabrication of α-Fe_2O_3 nanorod/RGO composite: a novel hybrid photocatalyst for phenol degradation. ACS applied materials & interfaces. 2013;5:9101-10.

[10] Yu W, Liu H, An X. Novel catalytic properties of supported metal nanoclusters. Journal of Molecular Catalysis A: Chemical. 1998;129:L9-L13.

[11] Zhang Z, Hossain MF, Takahashi T. Self-assembled hematite (α-Fe_2O_3) nanotube arrays for photoelectrocatalytic degradation of azo dye under simulated solar light irradiation. Applied Catalysis B: Environmental. 2010;95:423-9.

[12] Zhou X, Yang H, Wang C, Mao X, Wang Y, Yang Y, et al. Visible light induced photocatalytic degradation of rhodamine B on one-dimensional iron oxide particles. The Journal of Physical Chemistry C. 2010;114:17051-61.

[13] Wang X, Chen X, Gao L, Zheng H, Ji M, Tang C, et al. Synthesis of β-FeOOH and α-Fe_2O_3 nanorods and electrochemical properties of β-FeOOH. Journal of Materials Chemistry. 2004;14:905-7.

[14] Yu J, Yu X, Huang B, Zhang X, Dai Y. Hydrothermal synthesis and visible-light photocatalytic activity of novel cage-like ferric oxide hollow spheres. Crystal Growth and Design. 2009;9:1474-80.

[15] Jiao Y, Liu Y, Yin B, Zhang S, Qu F, Wu X. Hybrid α-Fe_2O_3@ NiO heterostructures for flexible and high performance supercapacitor electrodes and visible light driven photocatalysts. Nano Energy. 2014;10:90-8.

[16] Jia CJ, Sun LD, Yan ZG, You LP, Luo F, Han XD, et al. Single-Crystalline Iron Oxide Nanotubes. Angewandte Chemie. 2005;117:4402-7.

[17] Yan B, Su X. The synthesis and luminescence of $YP_xV_{1-x}O_4:Dy^{3+}$ microcrystalline phosphors by in situ co-precipitation composition of hybrid precursors. Mater Chem Phys. 2005;93:552-6.

[18] Li S, Zhang H, Wu J, Ma X, Yang D. Shape-control fabrication and characterization of the airplane-like FeO(OH) and Fe_2O_3 nanostructures. Crystal growth & design. 2006;6:351-3.

[19] Cheng X-L, Jiang JS, Jin CY, Lin CC, Zeng Y, Zhang QH. Cauliflower-like α-Fe_2O_3 microstructures: Toluene–water interface-assisted synthesis, characterization, and applications in wastewater treatment and visible-light photocatalysis. Chemical Engineering Journal. 2014;236:139-48.

[20] Umar A, Akhtar M, Dar G, Baskoutas S. Low-temperature synthesis of α-Fe_2O_3 hexagonal nanoparticles for environmental remediation and smart sensor applications. Talanta. 2013;116:1060-6.

[21] Jiao Y, Liu Y, Qu F, Umar A, Wu X. Visible-light-driven photocatalytic properties of simply synthesized α-Iron (III) oxide nanourchins. Journal of colloid and interface science. 2015;451:93-100.

[22] Lv J, Gong W, Huang K, Zhu J, Meng F, Song X, et al. Effect of annealing temperature on photocatalytic activity of ZnO thin films prepared by sol-gel method. Superlattices and Microstructures. 2011;50:98-106.

[23] Chen C, Yu B, Liu J, Dai Q, Zhu Y. Investigation of ZnO films on Si< 111> substrate grown by low energy O^+ assisted pulse laser deposited technology. Materials letters. 2007;61:2961-4.

[24] Barick K, Singh S, Aslam M, Bahadur D. Porosity and photocatalytic studies of transition metal doped ZnO nanoclusters. Microporous and Mesoporous Materials. 2010;134:195-202.

[25] Jubb AM, Allen HC. Vibrational spectroscopic characterization of hematite, maghemite, and magnetite thin films produced by vapor deposition. ACS Applied Materials & Interfaces. 2010;2:2804-12.

[26] Pandey G. Fe-EBT Chelate Complex: A Novel Mean for Growth of α-FeOOH and γ-Fe_2O_3 Nanostructures. Acta Metallurgica Sinica (English Letters). 2014;27:1127-33.

[27] Sherman DM, Waite TD. Electronic spectra of Fe^{3+} oxides and oxide hydroxides in the near IR to near UV. American Mineralogist. 1985;70:1262-9.

[28] Zhang X, Qin J, Hao R, Wang L, Shen X, Yu R, et al. Carbon-doped ZnO nanostructures: facile synthesis and visible light photocatalytic applications. The Journal of Physical Chemistry C. 2015;119:20544-54.

[29] Haldar KK, Sinha G, Lahtinen J, Patra A. Hybrid colloidal Au-CdSe pentapod heterostructures synthesis and their photocatalytic properties. ACS applied materials & interfaces. 2012;4:6266-72.

[30] Mitra S, Das S, Mandal K, Chaudhuri S. Synthesis of a α-Fe_2O_3 nanocrystal in its different morphological attributes: growth mechanism, optical and magnetic properties. Nanotechnology. 2007;18:275608.

Chapter 4

Synthesis and Characterization of Polyvinyl Pyrrolidone (PVP) Coated Fe_3O_4 Nanoparticles by Chemical co-precipitation Method and Removal of Congo Red Dye by Adsorption Process

Chapter-4

Synthesis and characterization of polyvinyl pyrrolidone (PVP) coated Fe_3O_4 nanoparticles by chemical co-precipitation method and removal of Congo red dye by adsorption process

The present paper deals synthesis of poly vinyl pyrrolidone (PVP) coated magnetite nanoparticles by chemical co-precipitation method. The samples were characterized using X-ray diffraction (XRD), scanning electron microscopy (SEM), energy dispersive X-ray spectroscopy (EDX), Fourier transform infrared spectroscopy (FTIR) and Brunner Emmett teller (BET) methods. The surface area, pore volume and pore radius were calculated by the BET analysis. The EDX and FTIR analysis demonstrated the fabrication of PVP coated Fe_3O_4 NPs. The as synthesized Fe_3O_4/PVP has successfully been used as an adsorbent for elimination of Congo red dye in aqueous medium.

4.1. Introduction:

Industrial effluent treatment is a provocative operation to restraint water contamination and to sustain ecosystem [1, 2]. Azo dyes are a renowned class of colouring compounds which are comprehensively been used in engineering applications. Congo red, a cationic dye, is benzidine derivative of azo dye and its structure is very stable. Even a slight concentration of the dye is revealed to be a foremost environmental threat [3-5], Exposure to MB leads to increase of heart beat, vomiting, shock, jaundice, quadriplegia, and tissue necrosis in humans [5, 6]. Various methods like ultrafiltration, reverse osmosis, coagulation, sedimentation chemical oxidation, membrane separation processes, electrochemical, aerobic, anaerobic microbial degradation etc. are accessible for waste water handling, however these methods have limitations like formation of inferior waste products which have to be further treated. Further, these procedures are time spending and price demanding [7-9]. In this regard the adsorption procedure is an efficient approach to take out pollutants present in the effluent water. Since the water management by adsorption method entirely dependent on excellence of the adsorbent, the improvement of effective and low cost sorbent materials is challenging task before material chemists. In the previous years number of adsorbents like activated carbon, zeolites, clay minerals, chitosan, lignocelluloses, biosorbents and functionalized polymers have been employed however, maximum of these materials are either not economic and effective or have associated difficulties of separation and generation of secondary wastes [10-14].

Due to large surface-to-volume ratio, nanomaterials are advanced class of adsorbent. In the recent years iron oxide nanoparticles, specially magnetite (Fe_3O_4) and maghemite (γ-Fe_2O_3), are the frequently used magnetic importers in various

biomedical applications such as magnetic resonance imaging contrast development agents, hyperthermia, manipulating cell membranes, biosensors, cataloging, and in drug delivery [15]. The proficient, economic, accessible and non-toxic monodisperse synthesis of Fe_3O_4 nanoparticles is extremely preferred for potential environmental applications. Fe_3O_4 is a potential, inexpensive and effortlessly synthesizable adsorbent with additional benefit of ease of solid–liquid separation using an external magnetic field. A. Debnath *at el*. reported the removal of an anionic organic dye (Congo red) using chemically synthesized Fe_2O_3 NPs as adsorbent and effect of pH, adsorbent dosage, temperature, adsorption time and primary concentration on adsorption were examined [16]. M. Saad et al. used sol-gel method to synthesize γ-Fe_2O_3-activated carbon nanocomposite for the selective removal of two-fold mixture of dyes containing reactive red 223 dye (RR) and Malachite Green dye (MG) by ultrasonic assisted adsorption method [17]. Nanosized magnetic iron oxide particles have been studied broadly as a novel adsorbent with great surface area and slight diffusion resistance by S. Shariati et al. [18]. In another report magnetic iron oxide nanoparticles have been used for elimination of dyes from artificial and actual textile wastewater by using adsorption technique and the effect of different experimental parameters viz. contact time, pH coexisting ions were investigated [19]. Porous magnetic microspheres, synthesized by one step friedel-craft alkylation reaction, been used for fast separation of dyes from aqueous solution [20]. Magnetite/reduced graphene oxide (MRGO) nanocomposites prepared via solvothermal approach has been developed to prepare for separation of dye waste product [21]. Further, the additional advantages like ease of synthesis, recovery, nonexistence of secondary waste product, cost-effectiveness as well as environmental friendliness makes these materials suitable candidates for effective treatment of effluent water [22].

Co-precipitation method is a cost effective, environmental friendly and biocompatible technique. [23, 24], however ultra-small Fe_3O_4 nanoparticles have not been efficaciously prepared by this technique yet. Owing to large surface area and dipole-dipole interactions of magnetic nanoparticles have tendency to agglomerate, hence the challenging issue associated with the use of Fe_3O_4 nanoparticles as adsorbent is the stabilization. Polymers implanting on magnetic nanoparticles is unique attractive procedures of surface modification [25, 26]. In the number previous reports it has been shown the decoration of polymeric layer of lipids, proteins, dendrimers, gelatin, dextran, chitosan, poly (vinyl alcohol) (PVA), etc. over NPs can effectively stabilize magnetic nanoparticles [27-32]. M. Vadivel et al. demonstrated that PVP coating successfully controls structural, morphological, dielectric and magnetic properties of $CoFe_2O_4$magnetic nanoparticles [33].In this study we used PVP polymer as coating material because it is water solvable, neutral, non-hazardous, and is frequently used in innumerable applications [33, 34]. Since the polymer PVP is attached to magnetic nanoparticles by covalent bonds, the complete magnetic fluid (ferrofluid) becomes stable for an extensive age of time.

In present paper we synthesized PVP coated Fe_3O_4 nanoparticles via co-precipitation technique, structural and optical properties have been considered with respect to the variation in concentration of polymer and adsorption study has been examined for elimination of Congo red dye from aqueous solution.

4.2. Experimental analysis:

4.2.1. Materials required:

All the chemicals used in this work were analytical grade and used as supplied. Ferric chloride hexa-hydrate ($FeCl_3 \cdot 6H_2O$), ferrous sulphate hepta-hydrate ($FeSO_4 \cdot 7H_2O$), poly vinyl pyrrolidone (PVP), ammonium hydroxide (NH_4OH, 26 %

of ammonia) and Congo red dye (CR) were procured from Merk. De-ionized water was used as solvent. All the glasswares were cleaned by concentrated acid. The dried apparatus were used in the completely experiments.

4.2.2. Synthesis of PVP coated iron oxide nanoparticles:

The PVP coated Fe_3O_4 nanoparticles were fabricated by chemical co-precipitation method. In the typical experiment, 50 mL aqueous solution of 0.017 M of ferric chloride, 50 mL aqueous solution of 0.033 M of ferrous sulfate and 1 g polyvinyl pyrrolidone (PVP) were mixed in 250 ml lessened flask. The solution mixture was stirred for 30 minutes time to achieve a standardized solution. 0.25 M of ammonia solution was mixed in 50 ml of distilled water and added gradually to above solution mixture until pH reaches 11. The solution mixture was vigorously stirred on motorized stirrer for 3 h at room temperature. The solution appeared black color, which is symbolic of formation of Fe_3O_4. The precipitate was magnetically separated using an enduring magnet bar, liquefied in methanol and again separated by magnet bar. This process was repeated 4 times to remove the surplus amine molecules. Black powdered PVP coated Fe_3O_4 nanoparticles were dried at room temperature for whole day time and calcinated at 400℃ for 4 h. In analogous way Fe_3O_4/PVP (2g) and Fe_3O_4/PVP (3g) materials were synthesized using 2 g and 3 g PVP.

4.2.3. Batch adsorption studies:

In this study, batch process was applied to estimate the adsorption process and the experiments were performed at room temperature (25 ± 1˚C) in 250 ml stoppered conical flask consisting of 50 mL solutions under study. In various adsorption experiments like impact of pH on extent of adsorption, contact time for adsorption isotherm experiments, 40 mg of adsorbent Fe_3O_4/PVP (1g) was assorted in 50 mL concentration of Congo red dye solutions. pH of the solutions was maintain by the

addition of appropriate quantity of 0.1 M HCl and 0.1 M NaOH solutions. After mixing of adsorbent into the investigation solution, beaker was shaken for a preferred contact time in an electrically thermostated reciprocating shaker at 150 rpm. In order to achieve the equilibrium condition, a proportion of solution was withdrawn at consistent time interval, centrifuged and investigated for residual Congo red using UV-visible spectrophotometer (carry 100). The adsorption amount was calculated via the subsequent equation:

$$q = \frac{(Co - Ce)V}{m} \quad (1)$$

The sorption efficiency, A %, of the Congo red dye was calculated from:

$$A\ (\%) = \frac{(Co - Ce)V}{Co} \quad (2)$$

Where C_0 and Ce are initial and equilibrium concentrations Congo red dye in mg L^{-1}, V is the volume of solution in mL and m is the amount of adsorbent in mg.

4.3. Characterization:

The X-ray diffraction patterns of as prepared PVP coated Fe_3O_4 materials were observed on Pananalytical's X'Pert Pro X-ray diffractometer in the 2θ range 10 to 80° with step size of 0.025°. Scanning electron microscope (SEM) images of the products were carried out on JEOL 6490 LB equipment. The scanning electron microscopic images were attained at an operating electrical energy of 3 kV. FT-IR spectra of as prepared Fe_3O_4/PVP (1g), Fe_3O_4/PVP (2g) and Fe_3O_4/PVP (3g) samples were recorded on Perkin Elmer Spectrum two equipment. Brunauer-Emmett-Teller (BET) analysis of all the materials was carried out on BELSORP MINI (II) equipment. UV-Visible spectra were record in absorption mode with a carry 100 spectrophotometer in the 200-800 nm regions.

4.4. Results and discussion:

4.4.1. XRD:

In order to examine phase, crystal arrangement and purity of above synthesized Fe_3O_4/PVP (1g), Fe_3O_4/PVP (2g) and Fe_3O_4/PVP (3g) materials XRD analysis was done and patterns are shown in Figure 4.1 a-c. The X-ray diffraction peaks in the XRD pattern of these materials are readily indexed as magnetite Fe_3O_4 phase. From the XRD pattern it is evident that as synthesized materials, obtained by calcination of precipitate at 400 ºC for 3 hour are phase pure Fe_3O_4. Furthermore, it is observable from the diffraction pattern that the XRD peaks are sharp and broadened; indicating formation of good crystalline and small sizes Fe_3O_4/PVP materials. The diffraction peaks analogous to (311), (400), (511), (440), (620) and (533) are quite identical to distinguishing peaks of the Fe_3O_4 crystal with the cubic spinal structure.

Size of the crystal of Fe_3O_4/PVP (1g), Fe_3O_4/PVP (2g) and Fe_3O_4/PVP (3g) materials was calculating using Scherer formula.

$$D = \frac{0.9\,\lambda}{\beta cos\theta} \qquad (1)$$

Where *D* is the crystallites size (in nm), λ the wavelength (in nm), $\beta$is the full width at half maxima (FWHM) and $\theta$is the Bragg's diffraction angle.

Though Scherrer equation is approximate, however it gives an idea about crystallites size, for the particle's dimension lower than 100 nm[35]. The width of diffraction peaks has contribution for the pair of instrumental and sample dependent effects. To decouple overhead contributions, diffraction pattern from line widening of an accepted material (Al_2O_3) was collected to describe the instrumental broadening. The instrumental corrected β_{hkl} for a selected diffraction peak of the materials was calculated using the equation,

$$\beta_{hkl} = [(\beta^2_{hkl})\text{measured} - (\beta^2)\text{instrumental}]^{1/2} \qquad (2)$$

The XRD peak (311) was used to define average particle's size. The calculated average crystallite's sizes of the materials Fe_3O_4/PVP (1g), Fe_3O_4/PVP (2g) and Fe_3O_4/PVP (3g) found to be 35, 32 and 30 nm respectively.

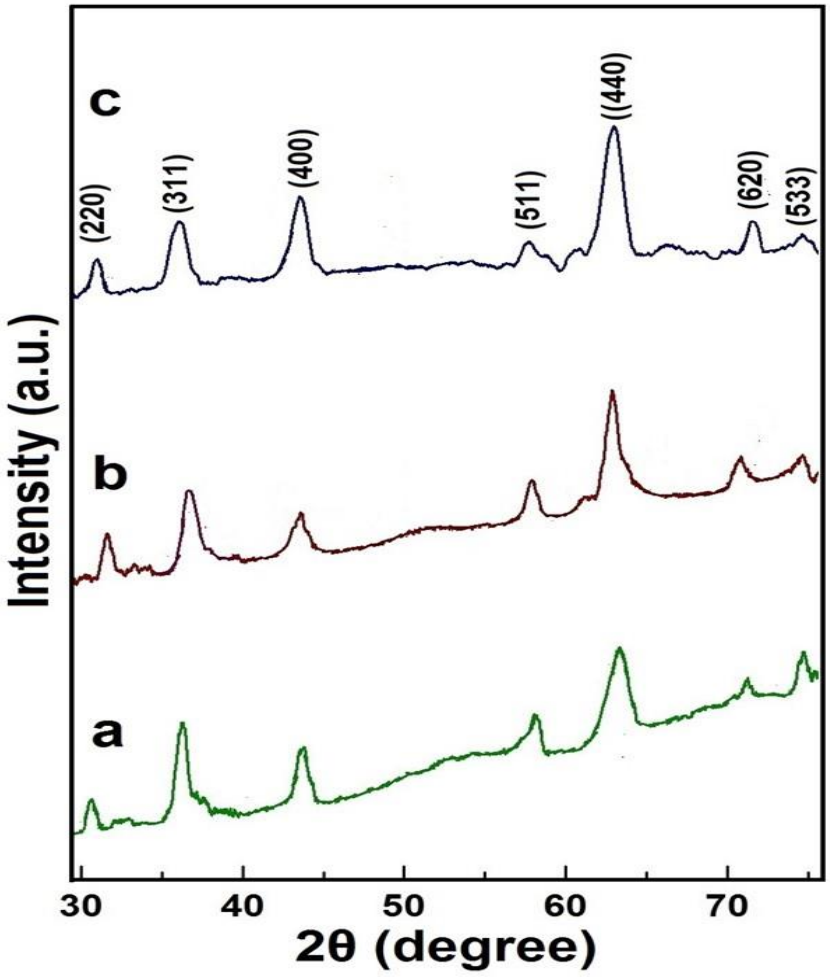

Figure 4.1: XRD patterns of (a) Fe_3O_4/PVP (1g) (b) Fe_3O_4/PVP (2g) (c) Fe_3O_4/PVP (3g) nanoparticles formed by calcination at 400 °C temperature.

4.4.2. FESEM and EDX:

FESEM images (Figure 4.2) indicate that the morphology of the Fe_3O_4 nanoparticles are roughly spherical in shape. As per reports, globular shape NPs form because the nucleation rate per unit area remains isotopic at the interface between the Fe_3O_4 magnetic nanoparticles [36, 37]. Figure 4.2 a-c show the typical FESEM micrographs of the samples Fe_3O_4/PVP (1g), Fe_3O_4/PVP (2g) and Fe_3O_4/PVP (3g) which are of nano-aggregates of ultrafine particles. Agglomeration found in these

samples is owing to the magnetic dipole–dipole interaction between NPs [38]. EDX pattern (Figure.2d, 2e, 2f) shows the composition of elements present in material. Strong peak of Fe and O were found in our sample and the percentage of Fe: O is found as 3:4.

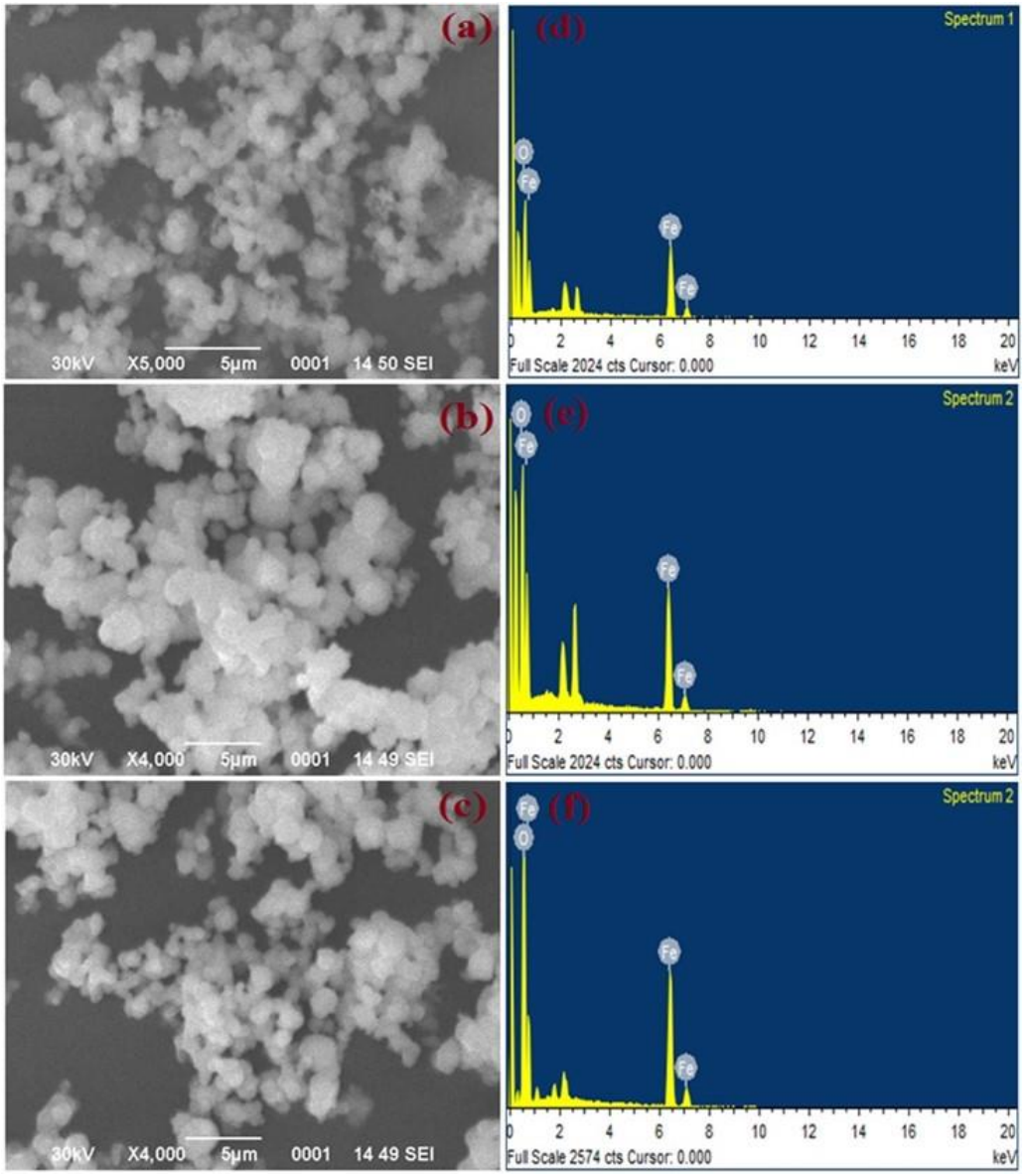

Figure 4.2: The SEM image of (a)Fe_3O_4/PVP (1g), (b) Fe_3O_4/PVP (2g) and (c) Fe_3O_4/PVP (3g) NPs. EDX pattern of (d) Fe_3O_4/PVP (1g), (e) Fe_3O_4/PVP (2g) and (f) Fe_3O_4/PVP (3g) NPs.

4.4.3. FTIR:

The FTIR spectra of Fe_3O_4 nanoparticles coated with disparate quantity of PVP are displayed in Figure 4.3. In FTIR spectra one peak found in the range 3444-

3401 cm^{-1} is owing to stretching frequency of -OH band of adsorbed water molecules on the surface of PVP coated Fe_3O_4 NPs while the peaks obtained between 1615-1642 cm^{-1} in these samples are ascribed to stretching frequency of C=O. Two vibration bands perceived at 572 and 633 cm^{-1} in these samples are the frequencies of magnetite [39]. The one vibrational band at 572 cm^{-1} has been ascribed to IR active T_{1u} mode of vibration of in Fe_3O_4 nanoparticles [40]. On increasing the extent of PVP, the C=O absorption bands shifts as of 1680 to 1662 cm^{-1}. The results indication that iron oxide is bonded with carbonyl group in PVP and the interaction between PVP and Fe_3O_4 diminution of the particle size, which contribute to surface significance of nanoparticles. The peak situated at 1289 cm^{-1} is owing to C–N stretching vibration of N-vinyl pyrrolidone. Overall, these FTIR spectra Further validate the formation of magnetite NPs which are coated with PVP through C=O interaction.

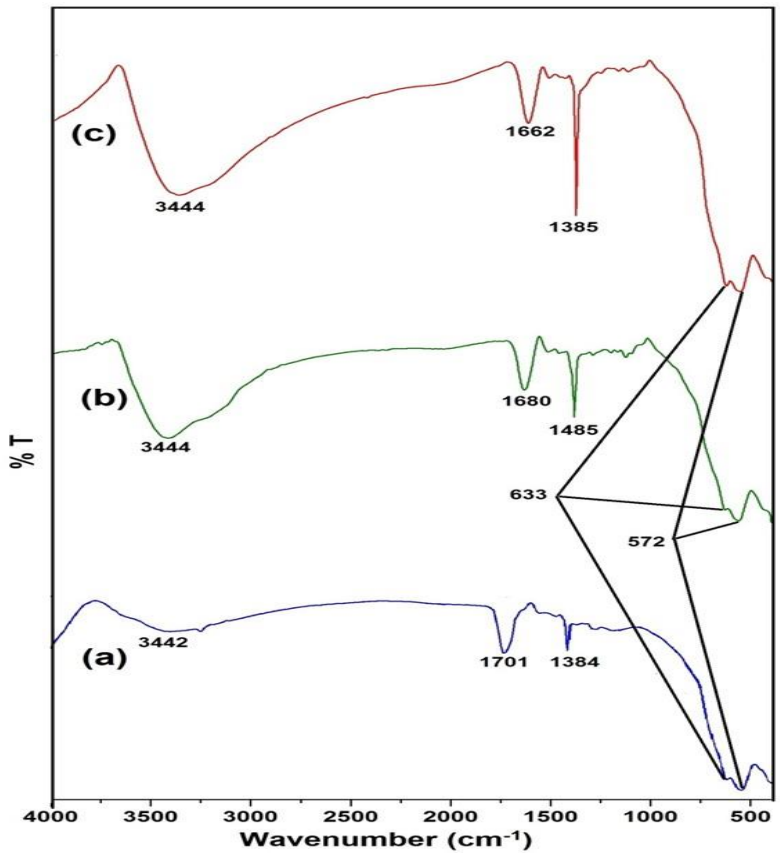

Figure 4.3: FTIR spectra of (a) Fe_3O_4/PVP (1g) (b) Fe_3O_4/PVP (2g) (c) Fe_3O_4/PVP (3g)

4.4.4. BET:

Nitrogen adsorption/desorption isotherm plots have been used to evaluate pore diameter (Dp) pore volume (Vp) and the surface area (S) of the synthesized materials in this study. The surface area of adsorbent material has immense significance in the adsorption process. Extra-large surface area is favorable for the adsorption procedure because then more active site is available for the adsorption of adsorbent. The isotherm profile of Fe_3O_4/PVP (1g) indicates dissimilar porosity (a mixture of type IV and type II, according to IUPAC classification). While the samples Fe_3O_4/PVP (2g) and Fe_3O_4/PVP (3g) show a predominance of type IV with H_2 hysteresis loop. In example of sample Fe_3O_4/PVP (1g), there is a high proportion of type II isotherms, the characteristic of mesoporous powders (H_4 hysteresis loop), which is fascinating for particular processes (catalysis and adsorption). The profile of pore diameter dissemination is presented in Figure 4.4 b (according to the BJH method revealed in Figure 4.5) demonstrates a broad pore size distribution, with the mainstream of the porous diameter situated in the array from 0 to 100 A˚. A rise in the quantity of iron in the sample composition stimulated variations in the hysteresis behavior, which can be accredited towards the closing of the pores by iron oxide. Table 4.1 presents detail description of the standards of the surface area, overall pore volume, and the ordinary pore diameter of the samples, which point to the textural outcome, promoted by a rise in the extent of iron. Samples with higher iron amount seem to have a lesser ratio of left over organic substances after the calcination process.

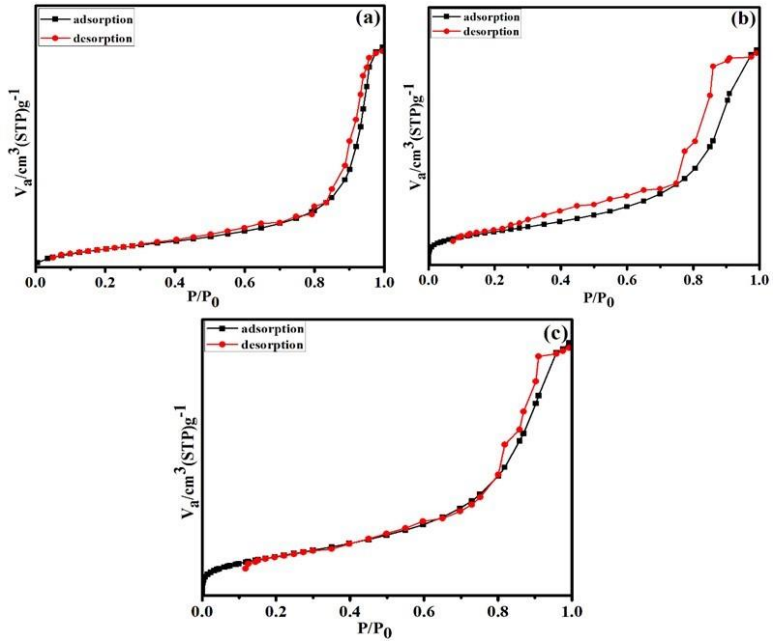

Figure 4.4: N_2 adsorption-desorption isotherms of (a) Fe_3O_4/PVP (1g) (b) Fe_3O_4/PVP (2g) (c) Fe_3O_4/PVP (3g) nanoparticles.

Sample	S (m^2/gm.)	Vp (cm^2/gm.)	Dp (nm)
Fe_3O_4/PVP (1g)	82.490	0.2991	1.21
Fe_3O_4/PVP (2g)	110.94	0.2877	7.99
Fe_3O_4/PVP (3g)	88.142	0.2128	6.06

Table 4.1: Values of the surface area, total pore volume, and the average pore diameter of the samples.

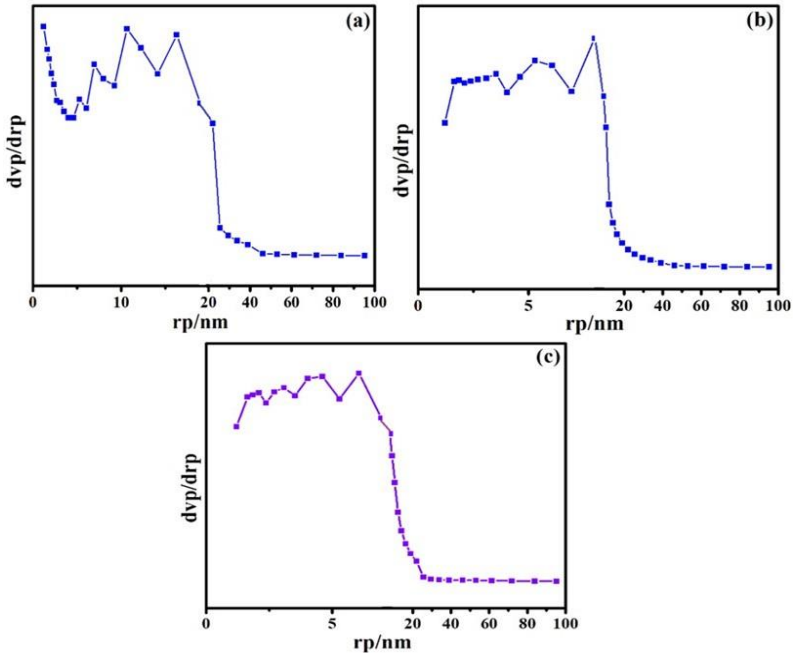

Figure 4.5: BJH plot of (a) Fe_3O_4/PVP (1g) (b) Fe_3O_4/PVP (2g) (c) Fe_3O_4/PVP (3g) NPs.

4.4.5. Adsorption study:

4.4.5.1. Effect of pH:

The pH of the sorbent media governs charge of the surface of adsorbent, the degree of ionization and speciation of adsorbate which play critical role on the sorption capability [41]. In this study the influence of pH on sorption of Congo red dye on the layer of Fe_3O_4/PVP (1g) (40 mg) NPs was conducted at room temperature in the pH range 2 to 11. In the adsorption analysis, Fe_3O_4/PVP (1g) was used as adsorbent because it shown sufficiently extraordinary surface area and the maximum pore volume among three materials. Desired pH was maintained by the addition 0.1 M HCl and 0.1 M NaOH solutions. The extent of adsorption of dye as a function of pH on the surface of Fe_3O_4/PVP (1g) is depicted in Figure 4.6. From the graph it appears that the adsorption of dye is minimum at pH 2, rises with increase of pH and attains peak at pH 5. Thereafter the extent of adsorption decreases attains minima at pH 10 and become constant on further increase of pH.

Congo red dye is an anionic dye and releases anionic $-SO_3^-$ ions on dissociation, thus solution become alkaline in aqueous media. The extent of adsorption of these ions on the sorbent surface is first and foremost influenced by the surface charge of the adsorbent, which in turn depend on the solution pH. At low pH the both, sorbent Fe_3O_4/PVP and dye Congo red are highly protonated due to greater concentration and greater mobility of H^+ ions. Therefore at low pH, the extent of adsorption of dye by surface of sorbent is low. On increasing the pH, the concentration of H^+ ions diminishes, therefore Congo red dye removal increases and maxima achieved at pH 5, for the reason that of higher concentration of anionic charged ligand accessible for sorption. At higher pH, the sorbent Fe_3O_4/PVP is

deprotonated and thus become reluctant to adsorption of negatively charged Congo red dye.

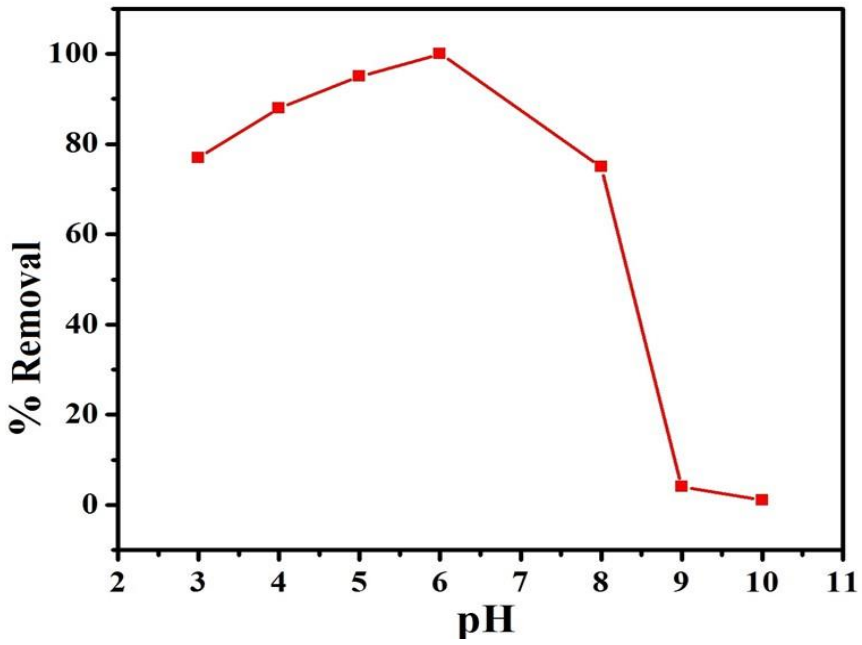

Figure 4.6: Effect of pH on adsorption of Congo red dye on the surface of Fe_3O_4/PVP (1g)

4.4.5.2. Effect of contact time:

In order to evaluate the degree of dye adsorption by adsorbent Fe_3O_4/PVP (1g) with course of time, series of tests were performed taking five Congo red dye concentrations viz.; 10, 20, 30, 40 and 50 ppm at constant pH 6. The sorption studies were performed between 0-90 minutes in the time step of 10 minutes. The extent of Congo red adsorption took place rapidly as experiments commenced however it becomes slow later and attained plateau at equilibrium, which reached on 90 minutes of time. The uptake of Congo red dye was 12.03, 23.76, 35.43, 46.93, and 57.6 mg/g^{-1} respectively for 10, 20, 30, 40 and 50 ppm sorbate solutions (Figure 4.7). The equilibrium time for Congo red dye was 90 minutes for all five dye concentrations. From the curves, it is concluded that the equilibrium time was not depends upon the initial concentration of Congo red.

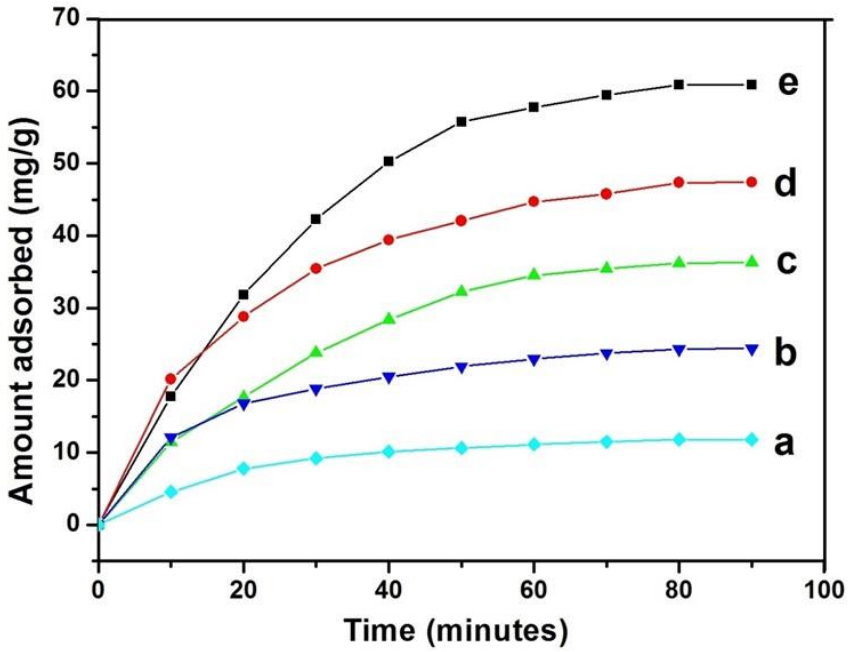

Figure 4.7: Effect of contact time and initial metal ions concentration on adsorption Congo red dye on the surface of Fe_3O_4/PVP (1g) at pH 6 on room temperature.

4.4.5.3. Adsorption isotherm:

With a view to explore the sorption mechanism at the surface of adsorbent Fe_3O_4/PVP (1g), Langmuir and Freudlich isotherms models were examined for the observed data. According to Langmuir sorption isotherm, the surface of sorbent is homogeneous and each sorption sites have equal sorbate affinity. Further, the adsorption at single site does not disturb sorption at neighboring cite[42] (equation 3).

$$\frac{C_e}{q_e} = \frac{1}{Q^0 b} + \frac{C_e}{Q^0} \qquad (3)$$

Here C_e is the equilibrium concentration (mg/L^{-1}) of dye Congo red, q_e the quantity adsorbed per unit weight of sorbent adsorbent Fe_3O_4/PVP at equilibrium (mg/g^{-1}), Q^0(mg/g^{-1}) and b is Langmuir constants, showing monolayer sorption ability and energy of sorption

The Freundlich isotherm model defines the equilibrium at assorted surface and does not undertake monolayer formation. The equation in the linear for can be written as:

$$\log q^{e} = \log K_F + \frac{1}{n}\log C_e (4)$$

In equation (4), n and K_F are Freundlich isotherm constants, representing concentration of sorption and relative sorption capability of sorbent. The n and K_F value can be calculated from the slope and intercept of the log qe versus log C_e plots.

Figure 4.8 shows the linear plots between Ce/qe versus Ce. Values of Langmuir constants Q^0 and *b* have been calculated from the slope and intercept of the graph (Table 4.2). Figure 4.9 indicates the Freundlich isotherm plots, *log qe* versus log *Ce*. The value of correlation coefficient R^2 was higher for Freundlich isotherm than that of Langmuir isotherm for Congo red dye, indicating suitable fitting of Freundlich isotherm is this study. Using Langmuir isotherm plot the maximum sorption capacity of adsorbent Fe_3O_4/PVP for dye Congo red has been determined as 113.63 mg/g.

Langmuir isotherm model		Freundlich isotherm model	
R^2	0.9889	R^2	0.9946
Q^0 (mg/g)	113.63	n	1.41
b (L/mg)	0.2914	K_f	24.37

Table 4.2: Values of Langmuir and Freundlich sorption constants for removal of dye Congo red at pH 5 at room temperature.

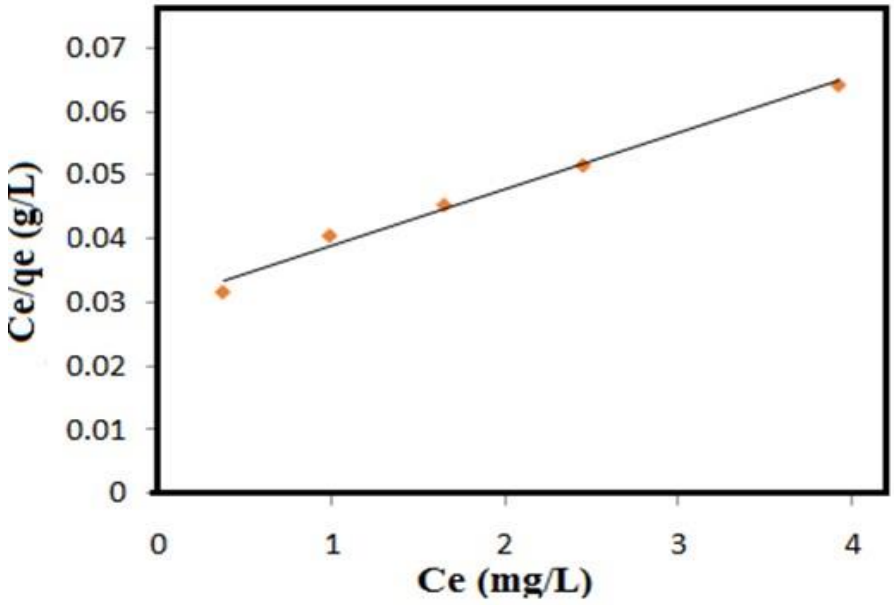

Figure 4.8: Langmuir isotherm plot

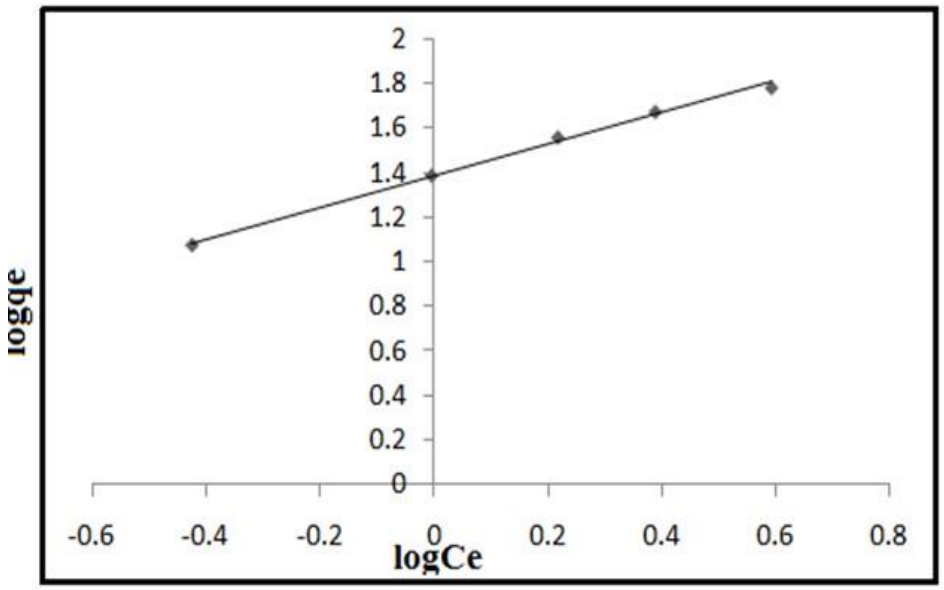

Figure 4.9: Freundlich isotherm plot

4.4.5.4. Sorption kinetics:

In the batch adsorption experiment, Lagergren pseudo first order and pseudo second order kinetics models are the extensively used rate equations for determining the adsorption of solute from a liquid solution and these models have been used to

understand the kinetics of present study. The Lagergren pseudo first order kinetics equation [43] can be expressed as:

$$\log(qe - qt) = \log qe - \frac{k1}{2.303}t \quad (5)$$

In equation (5) qe and $q_t$are amount of dye (mg/g^{-1}) adsorbed at equilibrium and at time *t*, respectively and k_1 is the rate constant of Lagergren pseudo first order sorption (min^{-1}).The *qe* and the value of rate constant $k_1$have been calculated from the slope and intercepts of plots between log (qe-qt) versus *t*, as revealed in Figure 4.10.

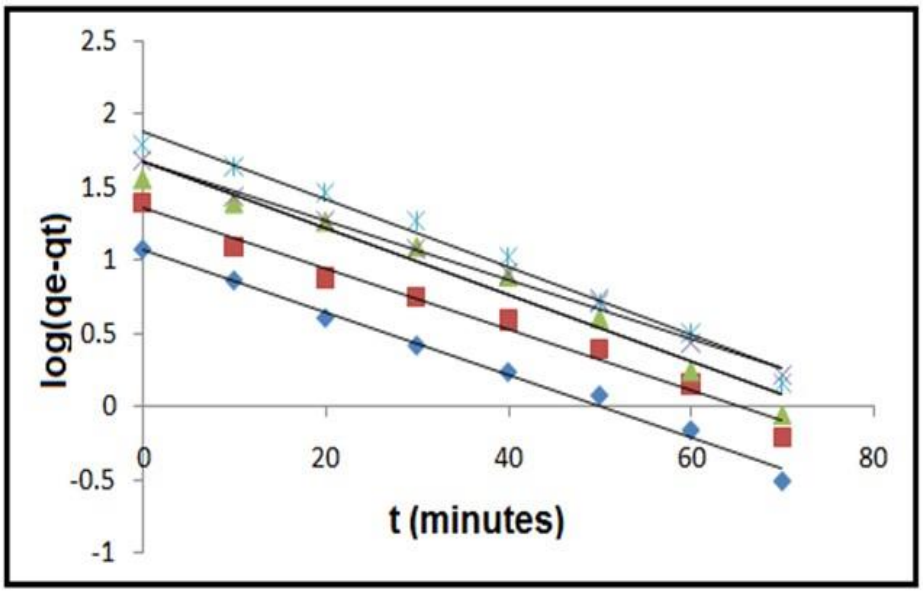

Figure 4.10: Pseudo first order kinetics

The kinetics data of dye adsorption has also been studied by pseudo second order equation [44]:

$$\frac{t}{qt} = \frac{1}{k_2 q_e^2} + \frac{1}{q_e}t \quad (6)$$

$$h = k_2' q_e^2 \quad (7)$$

Where k_2 is the rate constant and h is the original adsorption rate. The rate constant k_2 and qe have been determined from respectively slope and intercept t/qt against *t* plot (Figure 4.11). The experimental values of qe, computed values of qe, rate constants and correlation constants (R^2) for both pseudo first order and pseudo second order

equations are tabulated in Table 4.3. Closeness experimental and computed qe values for different kinetics models indicate their suitableness of rate kinetics [45]. Comparing the experimental and calculated qe values for pseudo first order and pseudo second order models, it has been found that the qe(exp.) and qe(calc.) values are more closer in instance of pseudo first order kinetics than pseudo second order (Table 4.3), indicating foemer is suitable rate kinetics model. Correlation coefficient values (R^2) are very high for both pseudo first and second order kinetics models, however these values are greater in situation of pseudo second order kinetics than the pseudo first order kinetics. Therefore it has been resolved that the pseudo second order kinetics is the appropriate kinetics to reach the equilibrium for dye Congo red at the adsorbent Fe_3O_4/PVP surface.

Dye conc; C_0 (ppm)	Pseudo first order kinetics				Pseudo second order kinetics			
	qe(exp.) (mg/g)	qe(calc.) (mg/g)	K_1 (min^{-1})	R^2	Qe(calc.) (mg/g)	K_2 (g/mg/min)	h (mg/g/min)	R^2
10	11.82	11.80	0.0529	0.991	12.98	0.00999	1.67	0.999
20	24.38	22.69	0.0461	0.982	28.57	0.00243	1.98	0.999
30	36.31	39.81	0.0507	0.994	52.63	0.00054	1.48	0.987
40	47.40	47.53	0.0461	0.994	58.82	0.00087	3.02	0.999
50	60.91	76.03	0.0484	0.985	90.90	0.00032	2.63	0.991

Table 4.3: Comparison of pseudo-first-order and pseudo-second-order kinetic models for removal Congo red by Fe_3O_4/PVP (1g) in different experimental conditions

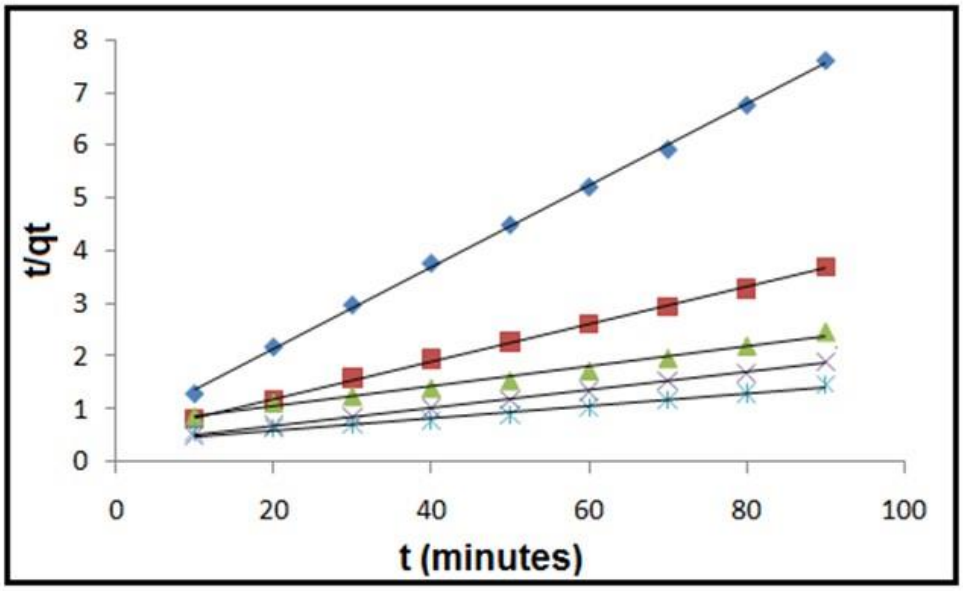

Figure 4.11: Pseudo second order kinetics

4.5. Conclusion:

Fe_3O_4 nanoparticles coated with varied amount of poly vinyl pyrrolidone (PVP) were successfully manufactured by a co-precipitation method. The synthesis route followed by calcination at 400 ºC led to evolution of crystalline cubic inverse spinel structure Fe_3O_4/PVP nanoparticles with excellent adsorptive properties owing to high surface area and pore volume. Adsorption study performed using Fe_3O_4/PVP (1g) as adsorbent since it shown high surface area and the highest pore volume. The highest adsorption was found at pH 6 using Fe_3O_4/PVP (1g) as adsorbent. The equilibrium time for Congo red dye was 90 minutes and it is independent of the initial concentration of Congo red dye. The correlation coefficient R^2 was higher for Freundlich isotherm than that of Langmuir isotherm for Congo red dye, indicating suitable fitting of Freundlich isotherm is this study. Pseudo second order kinetics is the appropriate kinetics to reach the equilibrium for dye Congo red at the adsorbent Fe_3O_4/PVP surface. Therefore, it has been concluded that PVP coated Fe_3O_4 NPs are effective adsorbent for elimination of dye Congo red and hence it may be used for wastewater remediation on industrial scale.

4.6. References:

[1] Rocher V, Siaugue JM, Cabuil V, Bee A. Removal of organic dyes by magnetic alginate beads. Water Research. 2008;42:1290-8.

[2] Tian Y, Ji C, Zhao M, Xu M, Zhang Y, Wang R. Preparation and characterization of baker's yeast modified by nano-Fe_3O_4: application of biosorption of methyl violet in aqueous solution. Chemical Engineering Journal. 2010;165:474-81.

[3] Devi CT, Ravikumar R, Kavitha N, Deepa SV. Impact of agitation for the color removal from dye effluent using isolated fungal species. Journal of Environmental Research and Development. 2013;7:1559.

[4] Murugesan K, Kalaichelvan P. Synthetic dye decolourization by white rot fungi. Indian journal of experimental biology. 2003;41:1076-87.

[5] Chen S, Zhang J, Zhang C, Yue Q, Li Y, Li C. Equilibrium and kinetic studies of methyl orange and methyl violet adsorption on activated carbon derived from Phragmites australis. Desalination. 2010;252:149-56.

[6] Uddin MT, Islam MA, Mahmud S, Rukanuzzaman M. Adsorptive removal of methylene blue by tea waste. Journal of Hazardous Materials. 2009;164:53-60.

[7] Nasuha N, Hameed B, Din ATM. Rejected tea as a potential low-cost adsorbent for the removal of methylene blue. Journal of Hazardous Materials. 2010;175:126-32.

[8] Martin MJ, Artola A, Balaguer MD, Rigola M. Activated carbons developed from surplus sewage sludge for the removal of dyes from dilute aqueous solutions. Chemical Engineering Journal. 2003;94:231-9.

[9] Rauf M, Qadri SM, Ashraf S, Al-Mansoori KM. Adsorption studies of Toluidine Blue from aqueous solutions onto gypsum. Chemical Engineering Journal. 2009;150:90-5.

[10] Shafeeyan MS, Daud WMAW, Houshmand A, Shamiri A. A review on surface modification of activated carbon for carbon dioxide adsorption. Journal of Analytical and Applied Pyrolysis. 2010;89:143-51.

[11] Panuccio MR, Sorgonà A, Rizzo M, Cacco G. Cadmium adsorption on vermiculite, zeolite and pumice: batch experimental studies. Journal of Environmental Management. 2009;90:364-74.

[12] Hizal J, Apak R. Modeling of cadmium (II) adsorption on kaolinite-based clays in the absence and presence of humic acid. Applied Clay Science. 2006;32:232-44.

[13] Bamgbose J, Adewuyi S, Bamgbose O, Adetoye A. Adsorption kinetics of cadmium and lead by chitosan. African Journal of Biotechnology. 2010;9:2560-5.

[14] Panda G, Das S, Guha A. Biosorption of cadmium and nickel by functionalized husk of Lathyrus sativus. Colloids and Surfaces B: Biointerfaces. 2008;62:173-9.

[15] Gupta AK, Gupta M. Synthesis and surface engineering of iron oxide nanoparticles for biomedical applications. Biomaterials. 2005;26:3995-4021.

[16] Debnath A, Deb K, Das NS, Chattopadhyay KK, Saha B. Simple chemical route synthesis of Fe_2O_3 nanoparticles and its application for adsorptive removal of Congo red from aqueous media: artificial neural network modeling. Journal of Dispersion Science and Technology. 2016;37:775-85.

[17] Saad M, Tahir H. Synthesis of carbon loaded γ-Fe_2O_3 nanocomposite and their applicability for the selective removal of binary mixture of dyes by ultrasonic adsorption based on response surface methodology. Ultrasonics sonochemistry. 2017;36:393-408.

[18] Shariati S, Khabazipour M, Safa F. Synthesis and application of amine functionalized silica mesoporous magnetite nanoparticles for removal of chromium (VI) from aqueous solutions. Journal of Porous Materials. 2017;24:129-39.

[19] Nassar NN, Marei NN, Vitale G, Arar LA. Adsorptive removal of dyes from synthetic and real textile wastewater using magnetic iron oxide nanoparticles: Thermodynamic and mechanistic insights. The Canadian Journal of Chemical Engineering. 2015;93:1965-74.

[20] Pan L, Xu M-Y, Liu Z-L, Du B-B, Yang K-H, Wu L, et al. Facile method for the synthesis of Fe_3O_4@ HCP core–shell porous magnetic microspheres for fast separation of organic dyes from aqueous solution. RSC Advances. 2016;6:47530-5.

[21] Sun H, Cao L, Lu L. Magnetite/reduced graphene oxide nanocomposites: one step solvothermal synthesis and use as a novel platform for removal of dye pollutants. Nano Research. 2011;4:550-62.

[22] Gupta V, Nayak A. Cadmium removal and recovery from aqueous solutions by novel adsorbents prepared from orange peel and Fe_2O_3 nanoparticles. Chemical Engineering Journal. 2012;180:81-90.

[23] Mohapatra S, Pramanik N, Mukherjee S, Ghosh SK, Pramanik P. A simple synthesis of amine-derivatised superparamagnetic iron oxide nanoparticles for bioapplications. Journal of materials science. 2007;42:7566-74.

[24] Zhang Y, Wang SN, Ma S, Guan JJ, Li D, Zhang XD, et al. Self-assembly multifunctional nanocomposites with Fe_3O_4 magnetic core and CdSe/ZnS quantum dots shell. Journal of Biomedical Materials Research Part A. 2008;85:840-6.

[25] Fan QL, Neoh KG, Kang ET, Shuter B, Wang SC. Solvent-free atom transfer radical polymerization for the preparation of poly (poly (ethyleneglycol) monomethacrylate)-grafted Fe_3O_4 nanoparticles: synthesis, characterization and cellular uptake. Biomaterials. 2007;28:5426-36.

[26] Yong Y, Bai Y, Li Y, Lin L, Cui Y, Xia C. Preparation and application of polymer-grafted magnetic nanoparticles for lipase immobilization. Journal of Magnetism and Magnetic Materials. 2008;320:2350-5.

[27] Suh WH, Suslick KS, Stucky GD, Suh Y-H. Nanotechnology, nanotoxicology, and neuroscience. Progress in neurobiology. 2009;87:133-70.

[28] Kellar KE, Fujii DK, Gunther WH, Briley-Sæbø K, Bjørnerud A, Spiller M, et al. NC100150 injection, a preparation of optimized iron oxide nanoparticles for positive-contrast MR angiography. Journal of Magnetic Resonance Imaging. 2000;11:488-94.

[29] Zhao X, Milton Harris J. Novel degradable poly (ethylene glycol) hydrogels for controlled release of protein. Journal of pharmaceutical sciences. 1998;87:1450-8.

[30] Jeong YI, Nah JW, Na HK, Na K, Kim IS, Cho CS, et al. Self-assembling nanospheres of hydrophobized pullulans in water. Drug development and industrial pharmacy. 1999;25:917-27.

[31] Massia SP, Stark J, Letbetter DS. Surface-immobilized dextran limits cell adhesion and spreading. Biomaterials. 2000;21:2253-61.

[32] Hao R, Xing R, Xu Z, Hou Y, Gao S, Sun S. Synthesis, functionalization, and biomedical applications of multifunctional magnetic nanoparticles. Advanced Materials. 2010;22:2729-42.

[33] Vadivel M, Babu RR, Ramamurthi K, Arivanandhan M. Effect of PVP concentrations on the structural, morphological, dielectric and magnetic properties of $CoFe_2O_4$ magnetic nanoparticles. Nano-Structures & Nano-Objects. 2017;11:112-23.

[34] Le Garrec D, Gori S, Luo L, Lessard D, Smith D, Yessine MA, et al. Poly (N-vinylpyrrolidone)-block-poly (D, L-lactide) as a new polymeric solubilizer for hydrophobic anticancer drugs: in vitro and in vivo evaluation. Journal of Controlled Release. 2004;99:83-101.

[35] Hitkari G, Singh S, Pandey G. Structural, optical and photocatalytic study of ZnO and ZnO–ZnS synthesized by chemical method. Nano-Structures & Nano-Objects. 2017;12:1-9.

[36] Lu W, Shen Y, Xie A, Zhang W. Green synthesis and characterization of superparamagnetic Fe_3O_4 nanoparticles. Journal of Magnetism and Magnetic Materials. 2010;322:1828-33.

[37] Kim DK, Mikhaylova M, Zhang Y, Muhammed M. Protective coating of superparamagnetic iron oxide nanoparticles. Chemistry of Materials. 2003;15:1617-27.

[38] Jadhav S, Nikam D, Khot V, Thorat N, Phadatare M, Ningthoujam R, et al. Studies on colloidal stability of PVP-coated LSMO nanoparticles for magnetic fluid hyperthermia. New Journal of Chemistry. 2013;37:3121-30.

[39] Cornell RM, Schwertmann U. The iron oxides: structure, properties, reactions, occurrences and uses: John Wiley & Sons; 2003.

[40] Yan H, Zhang J, You C, Song Z, Yu B, Shen Y. Influences of different synthesis conditions on properties of Fe_3O_4 nanoparticles. Materials Chemistry and Physics. 2009;113:46-52.

[41] El-Ashtoukhy E-S, Amin NK, Abdelwahab O. Removal of lead (II) and copper (II) from aqueous solution using pomegranate peel as a new adsorbent. Desalination. 2008;223:162-73.

[42] Hasan S, Singh K, Prakash O, Talat M, Ho Y. Removal of Cr (VI) from aqueous solutions using agricultural waste 'maize bran'. Journal of Hazardous Materials. 2008;152:356-65.

[43] Lagergren S. About the theory of so-called adsorption of soluble substances. 1898.

[44] Ho Y-S, McKay G. The kinetics of sorption of divalent metal ions onto sphagnum moss peat. Water research. 2000;34:735-42.

[45] Febrianto J, Kosasih AN, Sunarso J, Ju YH, Indraswati N, Ismadji S. Equilibrium and kinetic studies in adsorption of heavy metals using biosorbent: a summary of recent studies. Journal of hazardous materials. 2009;162:616-45.

Chapter 5

Synthesis, Characterization of Fe_3O_4, $CoFe_2O_4$ Nanomaterials and its Application in Photodegradation of Rhodamine B Dye

Chapter-5

Synthesis, characterization of Fe_3O_4, $CoFe_2O_4$ nanomaterials and their application in photodegradation of Rhodamine B dye

Cobalt ferrite has attracted considerable attention in recent years due to its unique physical Properties such as high Curie temperature, large magnetocrystalline anisotropy, moderate saturation magnetization, large magneto restrictive coefficient, excellent chemical stability and mechanical hardness. Magnetic nanoparticles were successfully prepared by co-precipitation method using Fe(III) and Co(II) in the presence of NH_4OH, at 90˚C. The structure, morphology and magnetic properties of as-prepared were characterized via X-ray diffraction (XRD), High resolution Scanning electron microscope (HRSEM), Energy dispersive x-ray spectroscopy (EDX), Fourier transform Infrared (FTIR) and UV-Visible spectroscopy,. XRD revealed the crystallographic structure of the synthesized sample. HRSEM images have shown the nearly spherical shape and particle size and morphology of cobalt ferrite nanoparticles. The EDS spectra have shown strong peaks of Fe, Co and O.

5.1. Introduction:

In the ancient few centuries, magnetic nanoparticles of spinel ferrite fascinates great curiosity, owing to their characteristic properties, such as, catalytic, optical, magnetic as well as electrical properties [1]. They have prospective applications in a number of fields like electromagnetic absorbers, microwave devices, catalysis, sensors, water purification, antibacterial, nanoelectronics, high density storage media, drug delivery, and magnetic resonance imaging [2]. The universal formula of spinel ferrite is represented by the formula AB_2O_4, where A and B assume the role of divalent and trivalent cations correspondingly. In an unexceptional spinel structure, complete divalent cations take of the tetrahedral sites, although the trivalent cations supersede the octahedral interstices [3]. The universal formula of Spinel ferrite nanoparticles are represented by a $A^{2+}Fe_2^{3+}O_4$, where A^{2+} has been switched by appropriate divalent metal ions such as Co, Cu, Mg, Zn, Mn and Ni etc. Cobalt ferrite $CoFe_2O_4$ is one and only one of the greatest momentous magnetic materials which can be extensively used in electronic technologies, specifically on magnetic and magneto-optical recording media as a consequence of their extraordinary magneto crystalline anisotropy, temperate saturation magnetization, mechanical inflexibility, and high coercivity and chemical steadiness [4-6]. Singh and co-workers reported zinc and nickel doped cobalt ferrite nanomaterial synthesized by reverse micelle technique and investigate the photocatalytic capability for degradation of RhB under visible light irradiation [7, 8].The material consequently synthesized, would be investigated for the photocatalytic degradation of RhB using visible light. The prepared photocatalyst is characterized by using so many characterization techniques to study the structural, morphological and optical properties.

5.2. Experimental section:

5.2.1. Materials used:

All chemicals used in this work were analytical grade and used devoid of further purification. Ferric chloride hexa-hydrate ($FeCl_3 \cdot 6H_2O$), ferrous sulphate hepta-hydrate ($FeSO_4 \cdot 7H_2O$), Cobalt chloride ($CoCl_2$) ammonium hydroxide (NH_4OH, 26% of ammonia) and Rhodamin B (RhB) were purchased from Merck India. Double distilled water was used as solvent. All the glasswares were washed by concentrated acid. The dried glasswares were used in all the experiments.

5.2.2. Synthesis procedure:

In this study Fe_3O_4 nanostructures have been synthesized by the simple co-precipitation method using Fe^{2+} and Fe^{3+} ions. Aqueous solutions Fe^{2+} and Fe^{3+} were prepared by dissolving ferric chloride and ferrous sulphate in double distilled water. The solutions Fe^{2+} and Fe^{3+} ions were mixed in 2:1 molar ratio and heated at 80 °C for 10 minutes. Subsequently heating, the solution was precipitated by addition of ammonia solution with uninterrupted stirring on the magnetic stirrer at 80 °C until pH reached to 13. The reaction mixture was all over again heated at 80 °C for 2 h. Black colored nanoparticles of iron oxide were precipitated. These nanoparticles were separated from the solution by using a strong magnet and washed several times with double distilled water. The powder was then dried in oven at 100 °C for overnight. The overall reaction can be written as

$$Fe^{2+} + 2Fe^{3+} + 8OH^- \rightarrow Fe_3O_4 + 4H_2O$$

The products were annealed at 400 °C for 3 h to get Fe_3O_4 nanoparticles and the same procedure follow for the synthesis of $CoFe_2O_4$ nanoparticles.

5.2.3. Photocatalytic activity:

The photocatalytic activity of as prepared Fe_3O_4 and $CoFe_2O_4$ materials was determined by photodegradation of dye rhodamin (Rhb) under visible light exposure

using Xe lamp (1000 W). 100 mg quantity of Fe_3O_4 was first dispersed in 100 mL of 50 ppm Rhb solution and stirred for 30 minutes in the murky condition in order to achieve the adsorption equilibrium. The solution was irradiated by visible light in a photocatalytic compartment. Throughout irradiation, solution was agitated using a magnetic stirrer and air was bubbled into the reaction medium to be responsible for a constant resource of oxygen. After desired period interval, an aliquot of solution was isolated, centrifuged and its absorbance was measured on UV-Visible spectrophotometer to calculate the proportion degradation. The similar procedure was repeated for $CoFe_2O_4$ nanoparticles also. The photocatalytic degradation efficiency was calculated using the following equation:

(%) degradation = $((A_0 - A)/A_0) \times 100$

Where A_0 represents the original absorbance of the dye solution and A; the absorbance subsequently irradiation at particular time.

5.3. Characterization technique:

The XRD patterns of as prepared Fe_3O_4 and $CoFe_2O_4$ nanoparticles were recorded on Pananalytical's X'Pert Pro X-ray diffractometer in the 2θ range 20 to 80◦ with step size of 0.025◦. High resolution Scanning electron microscope (HRSEM) images of the prepared nanomaterial were observed on SUPRA 40, Ziess equipment. The HRSEM micrographs were achieved at an operating voltage of 3 kV. EDX (Quantax 200 with X-Flash e Bruker) clearly identified the elements present in the nanoparticles. FTIR spectra of as prepared Fe_3O_4 and $CoFe_2O_4$ samples were characterized by the Perkin Elmer Spectrum RXI in the range 4000-400 cm^{-1}. UV-Visible spectra were recorded in absorption mode on Cary 100 spectrophotometer in the wavelength region 200-800 nm.

5.4. Results and discussion:

5.4.1. Structural study:

Figure 5.1 (a, b) shows the XRD patterns of $Fe_3O_4$and $CoFe_2O_4$samples, prepared by chemical co-precipitation methods. The structural analysis of the samples were made with the aid of X'pert software and the crystal structure of the samples was found to be inverse cubic spinel type. Using Scherer's equation, the average sizes of the crystals were estimated to be 33 nm for Fe_3O_4, 35 nm $CoFe_2O_4$ sample. XRD pattern of Fe_3O_4, $CoFe_2O_4$ is match with JCPDS standard cards no. 861358, 770426 with no extra phases and space group is fd-3m.

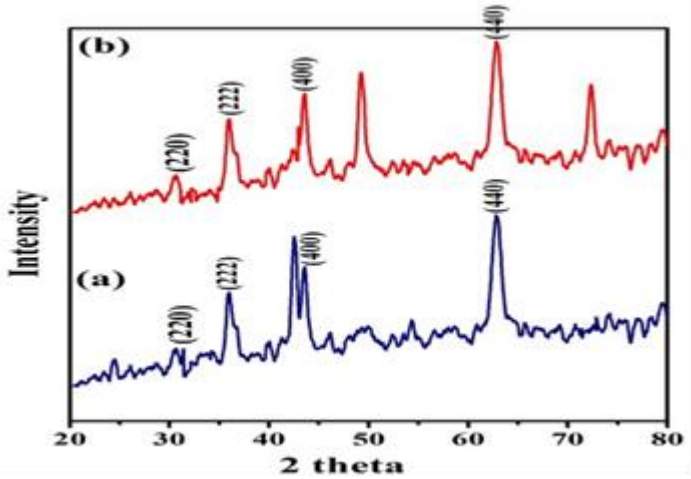

Figure 5.1: XRD of (a) Fe_3O_4 (b) $CoFe_2O_4$

5.4.2. Morphological and elemental study:

The morphology structure of the prepared ferrite nanoparticles is investigated by using HRSEM technique. Surface morphology of the prepared sample Fe_3O_4, $CoFe_2O_4$and are as revealed in Figure 5.2 (a, b). HRSEM image of sample (a) demonstrate the formation of porous, microstructure, spongy and similar to network like structure and (b) confirmations that the sample has an insignificant, sphere-shaped in shape and homogeneous crystallites structure which are homogeneously distributed. It can be observed that sample exhibit entirely interannular network with

homogenous cavities and pores. The pores structure is accredited to the release of considerable amount of gases during calcination process. Figure 5.2 (c, d) exhibit the EDX investigation of Fe_3O_4 and CoF_2O_4nanoparticles carried out at room temperature for the elemental corroboration and purity of the sample. The EDX spectrum confirms the homogeneity and gradient of the elements Fe, O, Co are present in the sample.

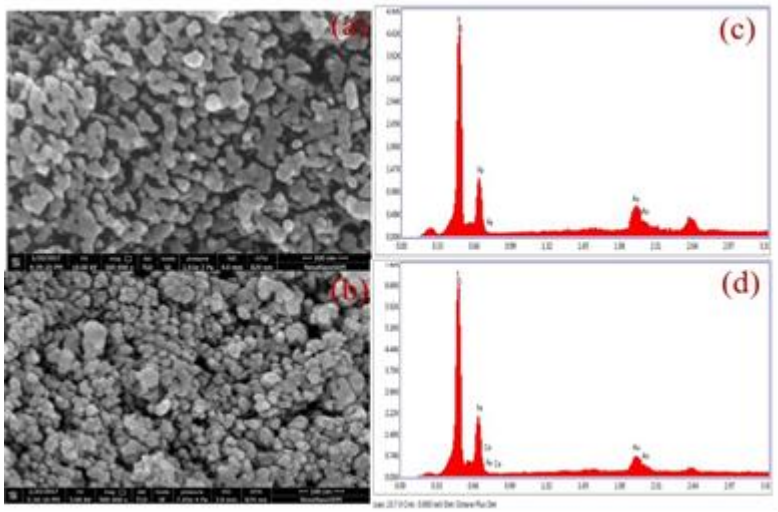

Figure 5.2: SEM image of (a) Fe_3O_4 (b) $CoFe_2O_4$

5.4.3. Functional study:

FTIR spectra of Fe_3O_4 and $CoFe_2O4$ nanoparticles is recorded in range 4000-400 cm^{-1}. In Figure 5.3 (a, b) shows the metal oxygen bond in 400-600 cm^{-1} range.

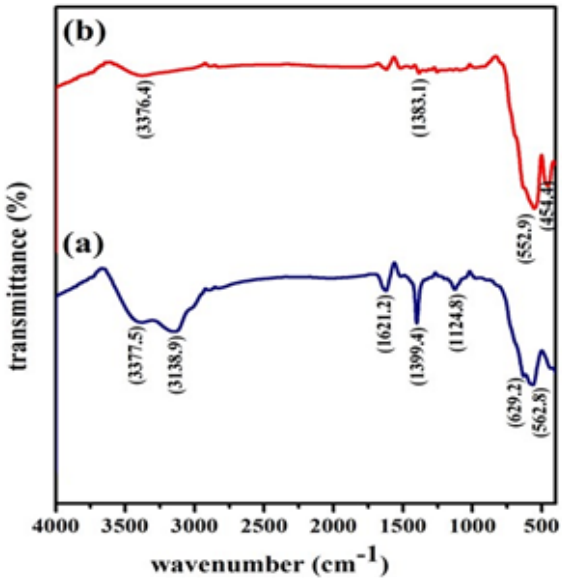

Figure 5.3: FTIR spectra of (a) Fe_3O_4 (b) $CoFe_2O_4$

5.4.4. UV-Visible spectrophotometer:

The optical properties were investigated by using UV-Vis spectrophotometer for pure Fe_3O_4 and $CoFe_2O_4$ ferrite nanostructures as presented in Figure 5.4 (a, b). Uninterrupted band gap energy of materials was calculated from the Tauc relation:

$$(\varepsilon h\nu)^2 = P\,(Eg - h\nu) \quad (1)$$

Where ε is the molar extinction coefficient, h is plank constant, ν is frequency of light, Eg is the band gap energy and P is the arbitrary constant. The linear part of the $(\varepsilon h\nu)^2$ verses hν graph (Figure 5.4. a) was used to calculate the band gap values. The intercept of tangent at the x axis gives Eg value. The Eg values for the $Fe_3O_4$and $CoFe_2O_4$materials 2.8, 2.9 eV using above relation (Figure 5.4 c, d).

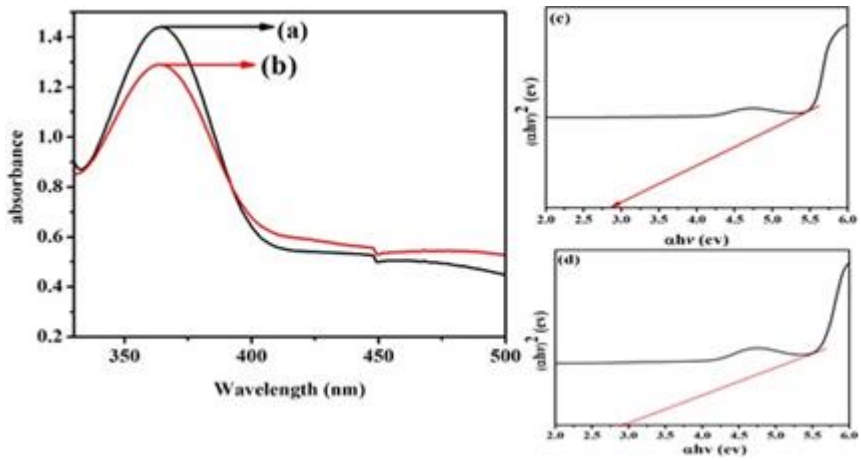

Figure 4: UV-Visible spectra of (a) Fe_3O_4 (b) $CoFe_2O_4$

5.5. Photodegradation study:

The photocatalytic degradation of Rhodamine B (RhB) in contradiction of the irradiation time are shown in the UV-Visible spectra in Figure 5.5 (a, b). In case of Rhodamine B dye show two absorption peaks at 503 and 558 nm owing to characteristics absorption of completely de-ethylated and tetraethylated Rhodamine B molecule correspondingly [9]. Then Figure 5.5 (c, d) shows the Fe_3O4 and $CoFe_2O_4$ follow Frist order kinetics. The value of R^2 is 0.91 for both sample.

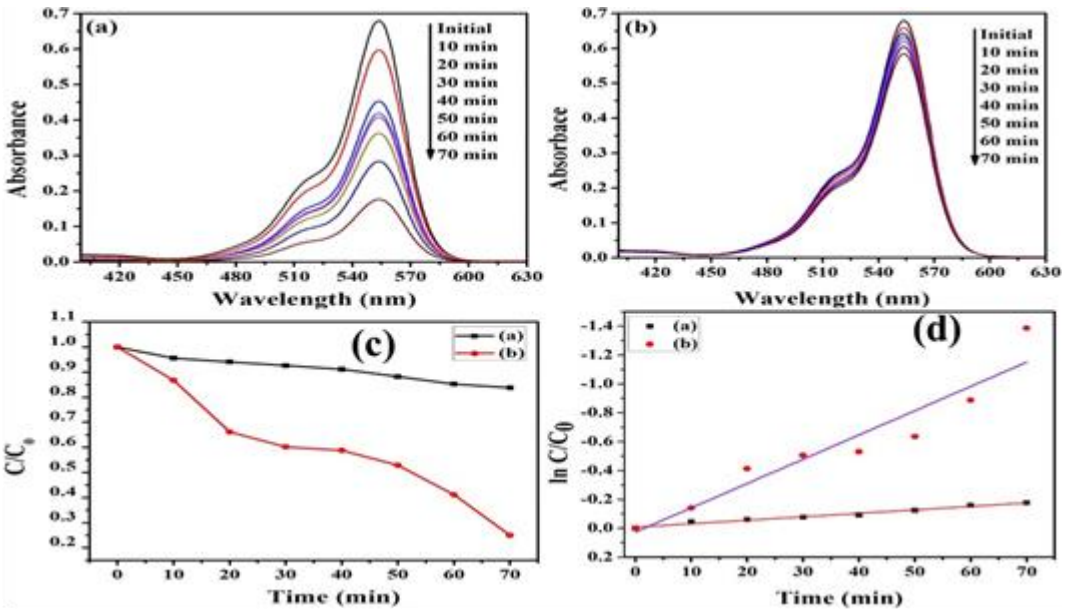

Figure 5.5: Photodegradation study of Rhb of (a) Fe_3O_4 (b) $CoFe_2O_4$ and (c) extent of degradation and (d) kinetics

5.6. Conclusion:

Pure Fe_3O_4 and cobalt ferrite ($CoFe_2O_4$) has been synthesize by chemical co-precipitation method using ammonia solution as a precipitating agent. The diffraction pattern obtained for pure Fe_3O_4 and cobalt ferrite system matched well with the JCPDS card number 861358, 770426. The effective crystallite size calculated by Scherer's method were found to be in the range, 33 nm. Photocatalytic activity of pure Fe_3O_4 is more effective as compared to CoF_2O_4 due to Photoluminance intensity of cobalt ferrite nanoparticles is increase.

5.7. References:

[1] Singhal G, Bhavesh R, Kasariya K, Sharma AR, Singh RP. Biosynthesis of silver nanoparticles using Ocimum sanctum (Tulsi) leaf extract and screening its antimicrobial activity. Journal of Nanoparticle Research. 2011;13:2981-8.

[2] Guo J, Wang R, Tjiu WW, Pan J, Liu T. Synthesis of Fe nanoparticles@ graphene composites for environmental applications. Journal of hazardous materials. 2012;225:63-73.

[3] Rothman A, Kalabukhov S, Sverdlov N, Dariel MP, Frage N. The Effect of Grain Size on the Mechanical and Optical Properties of Spark Plasma Sintering-Processed Magnesium Aluminate Spinel $MgAl_2O_4$. International Journal of Applied Ceramic Technology. 2014;11:146-53.

[4] Madhu B, Banu SR, Kavya M, Shruthi B, Vasanthkumar M, Sannamma T, et al. Dielectric Behavior and AC Conductivity Studies on Cobalt Nanoferrites Synthesized Using Combustion Method. Nanoscience, Technology and Societal Implications (NSTSI), 2011 International Conference on: IEEE; 2011. p. 1-4.

[5] Suzuki Y, Van Dover R, Gyorgy E, Phillips JM, Korenivski V, Werder D, et al. Structure and magnetic properties of epitaxial spinel ferrite thin films. Applied physics letters. 1996;68:714-6.

[6] Cheng FX, Jia JT, Xu ZG, Zhou B, Liao CS, Yan CH, et al. Microstructure, magnetic, and magneto-optical properties of chemical synthesized Co-RE (RE= Ho, Er, Tm, Yb, Lu) ferrite nanocrystalline films. Journal of applied physics. 1999;86:2727-32.

[7] Singh C, Goyal A, Singhal S. Nickel-doped cobalt ferrite nanoparticles: efficient catalysts for the reduction of nitroaromatic compounds and photo-oxidative degradation of toxic dyes. Nanoscale. 2014;6:7959-70.

[8] Singh C, Jauhar S, Kumar V, Singh J, Singhal S. Synthesis of zinc substituted cobalt ferrites via reverse micelle technique involving in situ template formation: a study on their structural, magnetic, optical and catalytic properties. Materials Chemistry and Physics. 2015;156:188-97.

[9] Qin C, Li Z, Chen G, Zhao Y, Lin T. Fabrication and visible-light photocatalytic behavior of perovskite praseodymium ferrite porous nanotubes. Journal of Power Sources. 2015;285:178-84.

Chapter 6
Synthesis and Characterization of Cadmium Doped Nickel Ferrite ($Ni_{0.6}Cd_{0.4}Fe_2O_4$) Nanoparticles and its Optical Properties

Chapter-6

Synthesis and characterization of Cadmium doped nickel Ferrite ($Ni_{0.6}Cd_{0.4}Fe_2O_4$) nanoparticles and its optical properties

Cd-Ni ferrite nanoparticles with a composition of $Ni_{0.6}Cd_{0.4}Fe_2O_4$ have been successfully prepared via simple co-precipitation technique using sodium hydroxide (NaOH) solution is used as a precipitating agent. The structural and optical properties of the samples were studied using Powder X-ray diffraction (PXRD), Scanning electron microscopy (SEM), Energy dispersive X-ray spectroscopy (EDX), Fourier transform Infrared Spectroscopy (FITR), UV-Visible spectroscopy (UV-Vis), and Fluorescence spectroscopy (FL) measurements. The PXRD analysis of all the samples shows the cubic phase without any impurity peaks. The average particle sizes were calculated by Scherrer's formula. The SEM image shows the agglomeration and flakes type nanoparticles with many void spaces due to exhaust of gases. EDX analysis is used for the elemental analysis of prepared samples (Cd, Ni, Fe, and O). FTIR spectra of the samples show the nature of the chemical bond between metal oxygen bonds (M-O). UV-Vis and PL spectra is used for the band gap calculation and its optical properties.

6.1. Introduction:

Ferrites are unbreakable, fragile, iron containing, gray or black in colour and they are polycrystalline i.e. made up of outsized number of crystals. They are formed by the chemical combination of iron oxide with one or extra other metals. These are ferrimagnetic material which encompasses iron or iron amalgams with body centered cubic crystal structure [1, 2]. Ferric oxide (iron oxide or rust) combined with any number of other metals as well as Mg, Ba, Mn, Ni, Cu or even iron itself. A ferrite is usually represented by the general formula MFe_2O_4 where M represents a few divalent metal that forms divalent bonds, such as elements Mg, Ba, Mn, Ni, Cu or even iron itself. Nickel ferrite for specimen is $NiFe_2O_4$, Manganese ferrite is $MnFe_2O_4$, and both are spinel ferrites. The most familiar ferrite known since biblical times is Magnetite (lode stone or ferrous ferrite $FeFe_2O_4$. Spinel Ferrite are performance a form of magnetism known as ferrimagnetism which is outstanding from the ferromagnetism of such materials as Fe, Co, and Ni [3-5].The structure of spinels can be 'normal' or 'inverse' is depending on the dissemination of cations on the interstitial sites. In situation the normal spinel, all the tetrahedral (A) sites are occupied by divalent cation, while the octahedral (B) sites are occupied by trivalent cation. Cadmium ($CdFe_2O_4$) and zinc ($ZnFe_2O_4$) ferrites are instances of normal spinels [6-9], where all the Cd^{2+} and Zn^{2+} ions are dispersed on the A sites and the Fe^{3+} ions occupy the B sites. In the situation inverse spinel structure the trivalent cation are dispersed similarly between A and B sites whilst all the divalent ions occupy B sites. Copper ($CuFe_2O_4$) and nickel ($NiFe_2O_4$) ferrites are instances of inverse spinels [10, 11]. In general, the dissemination of the different ions (cations) in the tetrahedral and octahedral sites of the spinel ferrite lattice essentially be influenced by the method of preparation and the processing situations. Innumerable preparation methods; for instance chemical co-precipitation, technique have been technologically advanced to produce nanosized ferrite nanoparticles. Nickel ferrite ($NiFe_2O_4$)

nanoparticles is unique lenient ferrite material owing to its low conductivity [12], lower eddy current fatalities and high electrochemical steadiness [12] with inverse spinel structure. The properties of nickel ferrite are, to a great extent, used in technological applications, as well as telecommunication, memory devices, electronic devices, antenna and transformer cores [14].

In the present work, $Ni_{0.6}Cd_{0.4}Fe_2O_4$ nanoparticles with a composition have been effectively synthesized via chemical co-precipitation technique using sodium hydroxide as precipitating agent. Advantage of this method is product formed is multi-component materials very effortlessly without any contaminations with desired stoichiometry. With this technique, particle size, chemical uniformity and degree of agglomeration can be without difficulty controlled. The prepared samples were characterized using Powder X-ray Diffraction (PXRD), Scanning Electron Microscopy (SEM), Energy dispersive X-ray spectroscopy (EDX), Fourier Transform Infrared Spectroscopy (FTIR), UV-Visible spectroscopy (UV-Vis) and Fluorescence spectra (FL).

6.2. Experimental section:

6.2.1. Materials:

For the synthesis of $Cd_{0.4}Ni_{0.6}Fe_2O_4$, the reagents were used as precursors are as follows: metal chlorides, cetyltrimethylammonium bromide (CTAB) as surfactant, sodium hydroxide and deionized water as solvent. Ferric chloride ($FeCl_3$), Nickel Chloride ($NiCl_2.6H_2O$) and Cadmium Chloride ($CdCl_2.2H_2O$) were used as product of Merck with purities exceeding 99% without further purification.

6.2.2. Synthesis procedure:

Nanocrystalline particle $Ni_{0.6}Cd_{0.4}Fe_2O_4$ were synthesized by co-precipitation method in this work. This method provides advantages, such as low synthesis temperature, small particle size and easy to proceed. All of the chemicals used are

analytical grade without further purification. For the synthesis of cadmium doped nickel ferrites nanoparticles, three solution containing 1 M solution of $FeCl_3$, 0.6 M solution of $NiCl_2.6H_2O$ and 0.4 M solution of $CdCl_2.H_2O$ were mixed and heated with continuous stirring for 30 min. pH of the mixed solution was maintained by aqueous solution of NaOH up to 11-12 range. Surfactant cetyltriammonuim bromide (CTAB), 0.5 g, was added to the mixed solution which was constantly stirred for 2 h so, obtained solution was aged at room temperature for 20 h. The precipitate was separated out and washed several times with distilled water in order to remove residual and impurities. The obtained product was dried in an oven at 100℃ for 3 h. The dried solid was crushed and crushed in a mortar to form powder. The obtained powder was calcined at 300℃ and other sample is not calcined.

6.3. Characterization technique:

The XRD patterns of as prepared pure $Ni_{0.6}Cd_{0.4}Fe_2O_4$ and calcinated $Ni_{0.6}Cd_{0.4}Fe_2O_4$ nanoparticles were recorded on Pananalytical's X'Pert Pro X-ray diffractometer in the 2θ range 20 to 80° with step size of 0.025°. Scanning electron microscope (SEM) images of the prepared nanomaterial were observed on SEM Jeol equipment. The SEM micrographs were achieved at an operating voltage of 3 kV. EDX (Quantax 200 with X-Flash e Bruker) clearly identified the elements present in the nanoparticles. FTIR spectra of as prepared pure $Ni_{0.6}Cd_{0.4}Fe_2O_4$ and calcinated $Ni_{0.6}Cd_{0.4}Fe_2O_4$ samples were characterized by the Perkin Elmer Spectrum RXI in the range 4000-400 cm^{-1}. Photoluminescence spectral studies of the materials have been carried out on spectrofluorometer (Perkin Elmer LS 55) at excitation wavelength 262 nm is measure optical properties including band gap also. UV-Visible spectra were recorded in absorption mode on Cary 100 spectrophotometer in the wavelength region 200-800 nm.

6.4. Result and discussion:

6.4.1. Structural analysis:

Figure6.1 (a, b) shows the XRD patterns of pure $Ni_{0.6}Cd_{0.4}Fe_2O_4$ and calcinated $Ni_{0.6}Cd_{0.4}Fe_2O_4$ samples, prepared by chemical co-precipitation methods. The structural analysis of the samples were made with the aid of X'pert software and the crystal structure of the samples was found to be inverse cubic spinel type. Using Scherer's equation, the average sizes of the crystals were estimated to be 9, 11 nm for pure $Ni_{0.6}Cd_{0.4}Fe_2O_4$ and calicinated $Ni_{0.6}Cd_{0.4}Fe_2O_4$ sample. In the given XRD patterns, the value of 2θ at 30.40º, 36.42º, 43.97º, 48.02º, 56.49º, 62.03º and 66.41º corresponds to planes (220), (311), (400), (420), (333), (440) and (442) of the cubic $Cd_{0.4}Ni_{o.6}Fe_2O_4$ as per JCPDS 790416. The value of lattice parameter (a) and the space group of this synthesized nanoparticles obtained from the XRD spectra are 8.394 Aº and F $\bar{4}$3m (216).

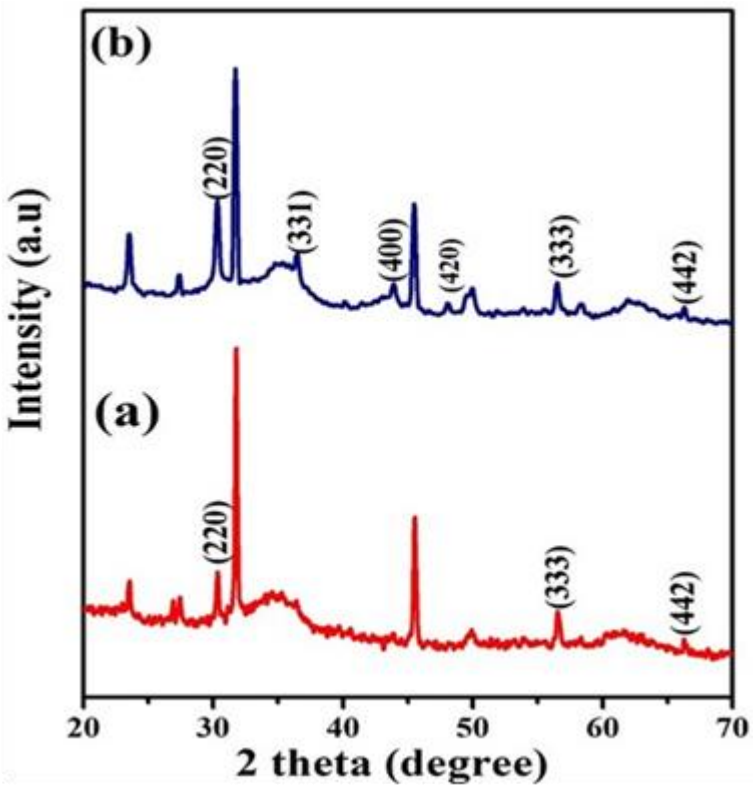

Figure 6.1: XRD spectra (a) pure $Ni_{0.6}Cd_{0.4}Fe_2O_4$ (b) Calcinated $Ni_{0.6}Cd_{0.4}Fe_2O_4$

6.4.2. Morphological and elemental analysis:

The morphology structure of the prepared ferrite nanoparticles is investigated by using SEM technique. Surface morphology of the prepared sample pure $Ni_{0.6}Cd_{0.4}Fe_2O_4$ and $Ni_{0.6}Cd_{0.4}Fe_2O_4$ are as revealed in Figure 6.2 (a, b). SEM image of pure $Ni_{0.6}Cd_{0.4}Fe_2O_4$ sample demonstrate the formation of porous, microstructure, spongy and similar to network like structure are shown in Figure 6.2 (a) and It can be observed that sample exhibit entirely interannular network with homogenous cavities and pores. In Figure 6.2 (b) shows the nearly spherical morphology. The pores structure is accredited to the release of considerable amount of gases during calcination process. Figure 6.2 (c, d) exhibit the EDX investigation of pure $Ni_{0.6}Cd_{0.4}Fe_2O_4$ and calcinated $Ni_{0.6}Cd_{0.4}Fe_2O_4$ nanoparticles carried out at room temperature for the elemental corroboration and purity of the sample. The EDX spectrum confirms the homogeneity and gradient of the elements Fe, O, Cd, Ni are present in the sample. The outcomes suggested that the precursors have completely reacted in the chemical reaction to form the single phase pure $Ni_{0.6}Cd_{0.4}Fe_2O_4$ and calicinated $Ni_{0.6}Cd_{0.4}Fe_2O_4$ nanoparticles as well as it approves that there is definitely not additional impurity existing in the samples. It is suggested that the comparative atomic mass ratio of the metal ferrites are acceptable matched along with the stoichiometry in preparation. The sample is gold coated for the improved visibility of the morphology shows in EDX spectra in form of peak.

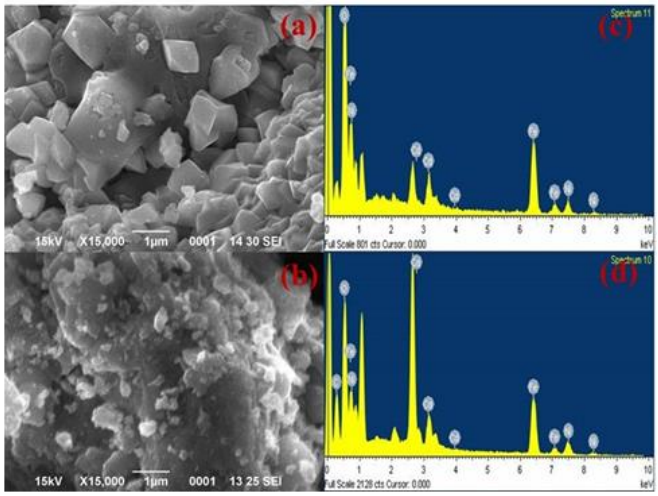

Figure 6.2: SEM image (a) pure $Ni_{0.6}Cd_{0.4}Fe_2O_4$ (b) Calcinated $Ni_{0.6}Cd_{0.4}Fe_2O_4$ (c, d) EDX spectra of pure $Ni_{0.6}Cd_{0.4}Fe_2O_4$ and Calcinated $Ni_{0.6}Cd_{0.4}Fe_2O_4$

6.4.3. Functional analysis:

FTIR spectrum of pure $Ni_{0.6}Cd_{0.4}Fe_2O_4$ and calcinated $Ni_{0.6}Cd_{0.4}Fe_2O_4$ at 400˚ C for 4 h is shown in Figure 6.3 (a, b). Spinel structure is confirmed by the most important absorption peak is detected in the range of 610-569 cm^{-1}. This peak is apportioned to the intrinsic stretching vibration of bonds between Cd^{2+} and oxygen ions. Another weakest peak detected in the range of 460-480 cm^{-1} is assigned to the stretching vibration of bonds between Fe^{3+} 4O and Ni^{2+}4O [13, 14]. A reduction in the wavenumber value of υ_1 indicates that Cd^{2+} preferred tetrahedral sites involve sp^3 hybrid orbital and forms covalent bonds. Also Cd^{2+} pushes the Fe^{3+} ion to tetrahedral site owing to the higher atomic weight in assessment to Nickel and oxygen and affects the bond length of Fe^{3+} 4O. The increase in cadmium content influences the metal oxygen bonds in the A-sites is due to the transition between inverse and mixed spinel structures. The absorption bands found at ~675 and ~1000-1300 cm^{-1} is assigned to the C-H group and C-O stretching bands correspondingly.

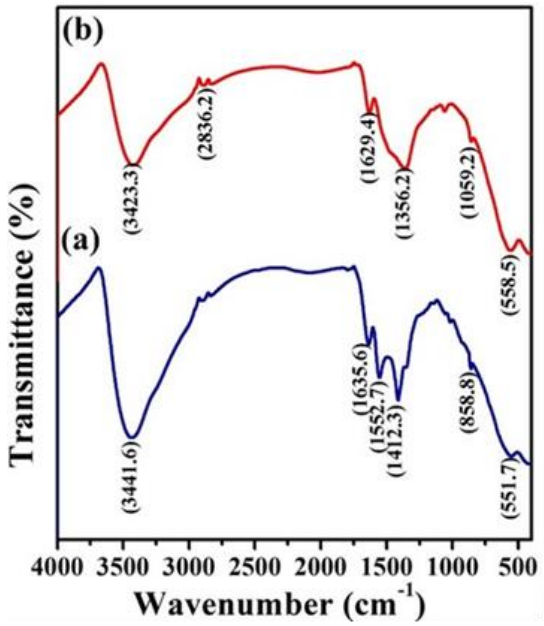

Figure 6.3: FTIR spectra (a) pure $Ni_{0.6}Cd_{0.4}Fe_2O_4$ (b) Calcinated $Ni_{0.6}Cd_{0.4}Fe_2O_4$

6.5. Optical analysis:

6.5.1. UV-Visible spectroscopy:

The optical properties were investigated by using UV-Vis spectrophotometer for pure $Ni_{0.6}Cd_{0.4}Fe_2O_4$ and calcinated $Ni_{0.6}Cd_{0.4}Fe_2O_4$ ferrite nanoparticles as presented in Figure 6.4 (a, b). In the condensed phase, Fe^{3+} exhibits three kinds of electronic transitions, first owing to ligand field transition, second owing to ligand metal charge transfer (LMCT from O^{2-} to Fe^{3+}) and third correspond to paired excitation of magnetically coupled Fe^{3+} ions occupying the adjacent sites in the crystals [15]. The band at 264 nm is accredited to Fe^{3+}←O charge transfer of isolated Fe ion in octahedral coordination [16]. The band at 373 nm is owing to charge transfer between oxygen and Fe^{2+} positioned in tetrahedral sites. Uninterrupted band gap energy of materials was calculated from the Tauc relation:

$$(\varepsilon h\nu)^2 = P\,(Eg - h\nu) \qquad (2)$$

Where ε is the molar extinction coefficient, h is plank constant, v is frequency of light, Eg is the band gap energy and P is the arbitrary constant. The linear part of the $(\varepsilon h\nu)^2$

verses hν graph (Figure 6.4. a, b) was used to calculate the band gap values. The intercept of tangent at the x axis gives Eg value. The Eg values for the pure $Ni_{0.6}Cd_{0.4}Fe_2O_4$ and calcinated $Ni_{0.6}Cd_{0.4}Fe_2O_4$ materials 3.1, 3.2 eV using above relation.

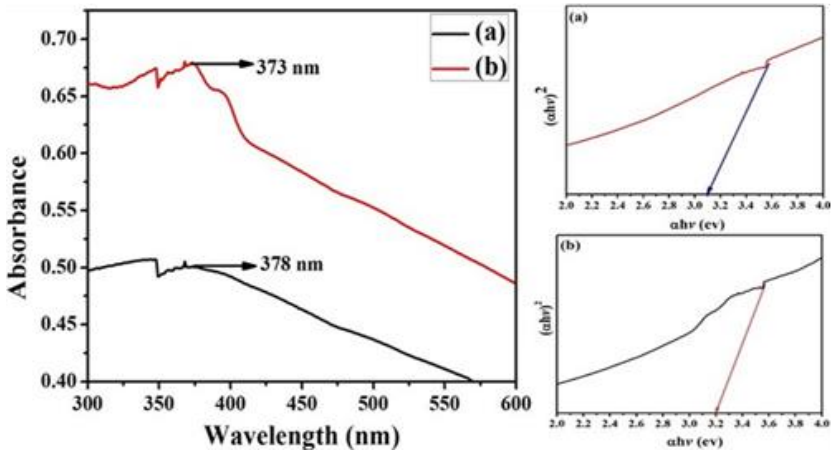

Figure 6.4: UV-Visible spectra (a) pure $Ni_{0.6}Cd_{0.4}Fe_2O_4$ (b) Calcinated $Ni_{0.6}Cd_{0.4}Fe_2O_4$ and (a, b) band gap of pure $Ni_{0.6}Cd_{0.4}Fe_2O_4$ and calcinated $Ni_{0.6}Cd_{0.4}Fe_2O_4$

6.5.2. Fluorescence spectrophotometer:

The photoluminescence spectra were recorded to investigate the recombination (or) effectiveness of photoproduced charge carrier, energetic situation of sub band gap and defects. Figure 6.5 (a, b) shows the pure $Ni_{0.6}Cd_{0.4}Fe_2O_4$ and calicinated $Ni_{0.6}Cd_{0.4}Fe_2O_4$ ferrite system excited at 300 nm [17]. The peaks in the UV range at 432 nm outcomes from the recombination of a photoexcited electron from the valence band to conduction band and in circumstance of $NiFe_2O_4$ nanomaterial peak confirmations at 408 nm shows in Figure 6.5 (b). The FL is accredited to lattice imperfections, and vacancies contained by the grain boundaries of pure ferrites system. The both samples appearance peak corresponding to violet emissions between 400- 450 nm. The violet emissions are owing to the radiating imperfections correlated to the interface traps existing at grain restrictions [18]. The decrease in the

luminescence concentration of calicinated $Cd_{0.6}Ni_{0.4}Fe_2O_4$ ferrites by increase the Cd^{2+} concentration, leads to intensification in the recombination rate of photogenerated electron-hole pairs. Thus, the FL can increases the photocatalytic property of calcinated $Ni_{0.6}Cd_{0.4}Fe_2O_4$ nanomaterial as compared to pure $Ni_{0.6}Cd_{0.4}Fe_2O_4$ material.

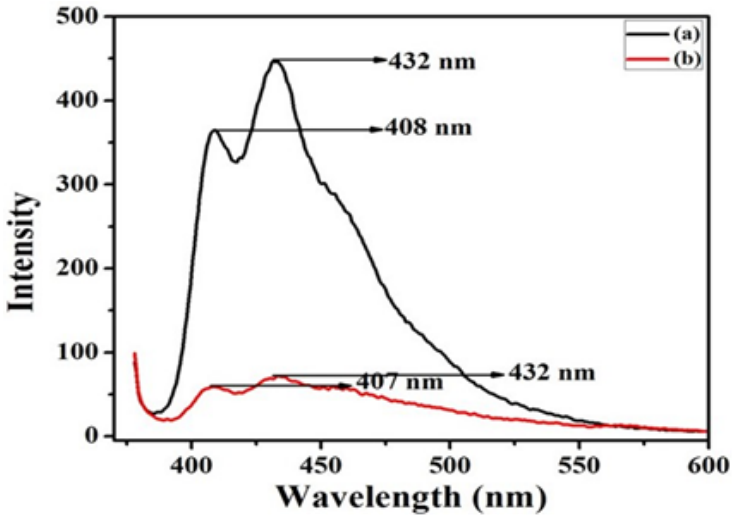

Figure 6.5: PL spectra (a) pure $Ni_{0.6}Cd_{0.4}Fe_2O_4$ (b) Calcinated $Ni_{0.6}Cd_{0.4}Fe_2O_4$

6.6. Conclusion:

In the present study I have synthesized cadmium doped nickel ferrite nanoparticles and calicinated for the effect of temperature on $Ni_{0.6}Cd_{0.4}Fe_2O_4$ by chemical co-precipitation method. From XRD pattern found cadmium doped nickel ferrite nanoparticles is cubic inverse spinel structure and match with JCPDS-790416 and SEM is used for the analysis of surface morphology and we found from SEM image is pure $Ni_{0.6}Cd_{0.4}Fe_2O_4$ is network like structure and the surface of calcinated sample is nearly spherical shape and agglomerated type due to calcination temperature. The band gap values for pure and calicinated $Ni_{0.6}Cd_{0.4}Fe_2O_4$ are calculated as 3.1 and 3.2 eV from UV-Visible absorption data.

6.7. References:

[1] Goldman A. Modern ferrite technology: Springer Science & Business Media; 2006.

[2] Sugimoto M. The past, present, and future of ferrites. Journal of the American Ceramic Society. 1999;82:269-80.

[3] Kumar KV, Reddy ACS, Ravinder D. High-frequency dielectric behaviour of erbium substituted Ni–Zn ferrites. Journal of Magnetism and Magnetic Materials. 2003;263:121-6.

[4] Deraz N, Alarifi A. Microstructure and magnetic studies of zinc ferrite nano-particles. Int J Electrochem Sci. 2012;7:6501-11.

[5] Mirghni AA, Siddig MA, Omer MI, Elbadawi AA, Ahmed AI. Synthesis of $Zn_{0.5}Co_xMg_{0.5-x}Fe_2O_4$Nano-Ferrites Using Co-Precipitation Method and Its Structural and Optical Properties. American Journal of Nano Research and Applications. 2015;3:27-32.

[6] Madhalea KV, Salunkheb MY, Bangalec SV. Structural, morphological and hydrophilic properties of nanocrystalline $NiFe_2O_4$ by combustion route. Archives of Applied Science Research. 2013;5:62-7.

[7] Wolska E, Wolski W, Piszora P, Pietrusik M, Šubrt J, Grygar T, et al. X-ray powder diffraction and Mössbauer studies on the formation of $Cd_{0.5}Ni_{0.5}Fe_2O_4/Zn_{0.5}Ni_{0.5}Fe_2O_4$ spinel solid solutions. International Journal of Inorganic Materials. 1999;1:187-92.

[8] Gibb TC. Principles of Mössbauer spectroscopy: Springer; 2013.

[9] Amer M, Hemeda O. 57 Fe Mössbauer and infrared studies of the system $Co_{1-x}Cd_x Fe_2O_4$. Hyperfine Interactions. 1995;96:99-109.

[10] Oak HN, Baek KS, Kim SJ. Mössbauer studies of superexchange interaction in tetragonal $CuFe_2O_4$. physica status solidi (b). 1998;208:249-55.

[11] Chinnasamy C, Narayanasamy A, Ponpandian N, Chattopadhyay K, Shinoda K, Jeyadevan B, et al. Mixed spinel structure in nanocrystalline $NiFe_2O_4$. Physical Review B. 2001;63:184108.

[12] Raghavender A, Kulkarni R, Jadhav K. Magnetic properties of nanocrystalline Al doped nickel ferrite synthesized by the sol-gel method. Chinese journal of physics. 2008;46:366-75.

[13] Chaudhari G. AC Impedance spectroscopy study on Nickel doped Cadmium Ferrites Nano particles prepared by sol-gel citrate method. measurements. 2014;3.

[14] Waldron R. Infrared spectra of ferrites. Physical review. 1955;99:1727.

[15] Ladgaonkar B, Kolekar C, Vaingankar A. Infrared absorption spectroscopic study of Nd^{3+} substituted Zn-Mg ferrites. Bulletin of Materials Science. 2002;25:351-4.

[16] Pandey G. Fe-EBT Chelate Complex: A Novel Mean for Growth of α-FeOOH and γ-Fe_2O_3 Nanostructures. Acta Metallurgica Sinica (English Letters). 2014;27:1127-33.

[17] Singh R, Narayan A, Prasad K, Yadav R, Pandey A, Singh A, et al. Thermal, structural, magnetic and photoluminescence studies on cobalt ferrite nanoparticles obtained by citrate precursor method. Journal of thermal analysis and calorimetry. 2012;110:573-80.

[18] Selvam NCS, Vijaya JJ, Kennedy LJ. Comparative studies on influence of morphology and La doping on structural, optical, and photocatalytic properties of zinc oxide nanostructures. Journal of colloid and interface science. 2013;407:215-24.

Chapter 7
Conclusion of Research Work and Scope of Future Research

Chapter-7

Conclusion

Conclusion of all chapters are discussed in the following:

Chapter	Remarks/Findings
Chapter-1	General introduction, literature review and objective of work
Chapter-2	Experimental work and Characterization techniques
Chapter-3	**α-Fe_2O_3-500:** XRD and SEM = rice grain like (45 nm long and 9 nm diameter) surface area (a_p) = 26.881 m^2g^{-1} pore volume (V_p) = 0.2652 cm^3g^{-1} band gap = 2.44 eV % photocatalytic degradation of dye methylene blue (Meb) = 92.8 % **α-Fe_2O_3-600:** XRD and SEM = spherical (50 nm diameter) nanocrystals surface area (a_p) =16.372 m^2g^{-1} pore volume (V_p) = 02105 cm^3g^{-1} band gap = 2.61 eV % photocatalytic degradation of dye methylene blue (Meb) = 85%
Chapter-4	Crystalline cubic inverse spinel structure Fe_3O_4/PVP nanoparticles with excellent adsorptive properties owing to great surface area and pore volume. PVP coated Fe_3O_4 NPs are effective adsorbent for elimination of dye Congo red adsorbent since it shown high surface area and the highest pore volume. Highest adsorption at pH = 6, Freundlich isotherm and pseudo second order kinetics fitting are appropriate.

Chapter-5	Photocatalytic activity of pure Fe_3O_4 is more effective as compared to CoF_2O_4 due to higher Photoluminance intensity of cobalt ferrite nanoparticles.
Chapter-6	$Ni_{0.6}Cd_{0.4}Fe_2O_4$ is synthesized by chemical co-precipitation method and effect of calcination temperature on optical properties has been discussed. The band gap values for pure and calcinated $Ni_{0.6}Cd_{0.4}Fe_2O_4$ are calculated as 3.1 and 3.2 eV from UV-Visible absorption data.

Scope and Further Research

- In the present work iron oxide nanoparticles and its composites have been optimized, however, the shape and size distribution of the materials may also modify the response characteristics. Hence, an effort will be made to explore the growth behavior of materials to optimize experimental conditions to achieve better shape and size distribution of iron oxide nanostructures.
- To expand the photocatalytic activity of metal iron oxide and its composite nanostructures through surface modification using various types of organic polymers and surfactants such as polyaniline, graphene oxide, reduced graphene oxide, cationic as well as anionic surfactants.
- To explore the role of shape and size of nanomaterials on photocatalytic degradation of organic dyes.

List of Publications

LIST OF PUBLICATIONS

1. **Sandhya Singh,** Gaurav Hitkari, Gajanan Pandey, Synthesis, Characterization of Fe_3O_4, $CoFe_2O_4$ Nanomaterials and its Application in Photodegradation of Rhodamin B dye, International Journal of Advanced Research in Science, Engineering and Technology (IJARSET) 4 (**2017**) 3966-3971.
2. **Sandhya Singh,** Gaurav Hitkari, Gajanan Pandey, Synthesis and characterization of Cadmium doped nickel Ferrite ($Ni_{0.6}Cd_{0.4}Fe_2O_4$) nanoparticles and its optical, International Journal of scientific and engineering research (IJSER) 8 (**2017**) 1630-1635.
3. **Sandhya Singh,** Gaurav Hitkari, Gajanan Pandey, "Effect of annealing temperature on structural, optical and photocatalytic properties of α-Fe_2O_3 nanostructures", communicated to Inorganic and nanometal chemistry **(Tayler and Francis)** (**2017** under review).
4. **Sandhya Singh,** Gaurav Hitkari, Gajanan Pandey "Synthesis and characterization of polyvinyl pyrrolidone (PVP) coated Fe_3O_4 nanoparticles by chemical co-precipitation method and removal of Congo red dye by adsorption process" communicated to International Nano Letters **(Springer)** (**2018** under review)**.**
5. Gaurav Hitkari, **Sandhya Singh,** Gajanan Pandey "Structural, optical and photocatalytic study of ZnO and ZnO-ZnS synthesized by chemical method" Nano-Structure and Nano Objects **(Elsevier)** 12 (**2017**) 1-9.
6. Gaurav Hitkari, **Sandhya Singh,** Gajanan Pandey "Synthesis, Characterization and Visible Light Degradation of Organic dye by Chemically Synthesized

ZnO/γ-Fe_2O_3 Nanocomposites" International Journal of Advanced Research in Science, Engineering and Technology (IJARSET) 4 (**2017**) 3960-3965.

7. Gaurav Hitkari, **Sandhya Singh,** Gajanan Pandey "Synthesis, characterization and photocatalytic application of copper-zinc oxide nanocomposites" communicated to Advanced Powder Technology **(Elsevier)** (**2017** under review)
8. Gaurav Hitkari, **Sandhya Singh,** Gajanan Pandey "Photoluminescence behavior and visible light photocatalytic activity of ZnO, ZnO/ZnS and ZnO/ZnS/α-Fe_2O_3 nanocomposites" Transactions of Nonferrous Metals Society of China **(Elsevier)** (**2017**) **Revised Manuscript Submitted decision pending.**

Book Chapters

1. Gaurav Hitkari, **Sandhya Singh,** Gajanan Pandey "Nanoparticles and their application in environmental wastewater management" in book "Emerging and Ecofriendly Approaches for Waste Management" Springer Singapore **(Springer)** (**2017**) **(**Accepted**).**
2. **Sandhya Singh,** Gaurav Hitkari, Gajanan Pandey **"**Synthesis, characterization and remediation application of iron oxide nanoparticles" in book "Ecofriendly Approaches for Environmental Management" to "Recent Advances in Environmental Management**"** CRC Press **(Taylor and Francis)** (**2017**) **(**Accepted**).**

CONFERENCES

1. National Conference on Recent Trends In Environmental Science, 4-5 February, 2014, Organized by Jwaji University Gwalior. **(Oral presentation)**
2. International Conferences on Updates in Cancer Prevention and Research, 14-16 February, 2017, Organized by BBAU Lucknow. **(Oral presentation).**
3. Recent Advances and Innovations In Chemical and Materials Sciences, 23-24 February, 2017, Organized by KKC college Lucknow. **(Oral presentation).**
4. National Conference on Advances in Basic & Applied Sciences, 7-8 April, 2017, Organized by Hameerpur University (H.P). **(Oral presentation).**
5. International Conference on Chemistry and Materials Prospects and Perspective, 14-16 December, 2012, Organized by BBAU Lucknow.
6. 2nd Lucknow Science Congress, 27-28 March, 2014, Organized by BBAU Lucknow.
7. International Symposium on Advances in Materials Characterization, organized by Babasaheb Bhimrao Ambedker University, Lucknow. **(14 July, 2014)**
8. International Conferences on chemistry and materiales prospects and perspectives Babasaheb Bhimrao Ambedkar University Lucknow. **(Attended) (14-16 Dec 2012).**

Workshops

1. National workshop on Innovation and Technology transfer to industries: Role of universities Babasaheb Bhimrao Ambedkar Universities Lucknow. **(Participated) (10-11 March 2014).**
2. "Bridging development divide for inclusive growth through Science Technology and Innovation" Babasaheb Bhimrao Ambedkar University Lucknow. **(Participated) (16-17 Jan 2015**).
3. Global Initiative for Academic Networks International Workshop on "Heterogeneous Catalysis and Applications" organized by Punjab University Chandigarh Punjab. **(Participated) (01-05 Aug 2016).**
4. National workshop on Research methodology and statistical analysis in Yogic Sciences organized by Sports Section Babasaheb Bhimrao Ambedkar University Lucknow. **(Participated) (22-28 Aug 2016).**